Modelling the external ballistics of tranquilliser darts

by

Aldert Johan Cilliers

Thesis presented in partial fulfilment of the requirements for the degree of Master of Engineering (Mechanical) in the Faculty of Engineering at Stellenbosch University

Supervisor: Dr. D.N.J. Els

March 2021

Declaration

By submitting this thesis electronically, I declare that the entirety of the work contained therein is my own, original work, that I am the sole author thereof (save to the extent explicitly otherwise stated), that reproduction and publication thereof by Stellenbosch University will not infringe any third party rights and that I have not previously in its entirety or in part submitted it for obtaining any qualification.

Date: 2021/01/15

Abstract

Modelling the external ballistics of tranquilliser darts

A.J. Cilliers
Department of Mechanical and Mechatronic Engineering,
University of Stellenbosch,
Private Bag X1, Matieland 7602, South Africa.

Thesis: MEng (Mech)

March 2021

To facilitate the design of tranquilliser darts, several ballistic models are investigated, derived, implemented and verified. Sensitivity analysis showed the required model fidelity and parameter accuracies are significantly less stringent for subsonic, flat trajectories. This agrees with doppler radar measurements suggesting drag stabilised darts have a near constant drag coefficient. This is further corroborated by computational fluid dynamics (CFD) analysis: aerodynamic coefficients are independent of velocity but sensitive to angle of attack. The tailpiece however ensures there is little to no pitching and/or yawing, eliminating non-linearities due to instability (the angle of attack). Consequently, a single CFD analysis at an average velocity can sufficiently estimate the aerodynamic forces and moments. For the same reasons, Point-mass and Modified point-mass approximations are qualitatively on par with Rigid-body approximations (in most cases).

Due to drag stabilisation by the tailpiece, the drag coefficients measured and simulated are high ($C_D >= 0.9$). Future designs' aerodynamic efficiency can be improved by rather using spin stabilisation. Point-mass and Modified point-mass approximations are however unable to account for instabilities. If considered, Rigid-body approximations are recommended to confirm initial stability.

Uittreksel

Modellering van die eksterne ballistiek van verdowingspyle

("Modelling the external ballistics of tranquilliser darts ")

A.J. Cilliers
Departement Meganiese en Megatroniese Ingenieurswese,
Universiteit van Stellenbosch,
Privaatsak X1, Matieland 7602, Suid Afrika.

Tesis: MIng (Meg)
Maart 2021

Om die ontwerp van verdowingspyle te vergemaklik, is verskeie ballistiese modelle ondersoek, geïmplementeer en geverifieer. Sensitiwiteitsanalise toon modelgetrouheid asook dat parameterakkuraatheid minder streng is vir kort en plat trajekte. Dit stem ooreen met doppler radar metings waar die verdowingspyl se sleur koëffisiënt konstant is. Berekenings vloeimeganika (BVM) toon dat die verskeie koëffisiënte onafhanklik is van snelheid maar sensitief vir invalshoek. Die stert verseker 'n klein invalshoek en bevorder sodoende die konstante geaardheid van die koëffisiënte. Gevolglik sal 'n eenmalige BVM simulasie, by 'n gemiddelde snelheid voldoende wees om die aerodinamise kragte en momente te bepaal. Vir soortgelyke redes is Puntmassa en Gemodifiseerde-puntmassa analises kwalitatief gelykstaande aan Rigiede-liggaam analises.

As gevolg van die stert, is die sleur koëffisiënt hoog ($C_D >= 0.9$). Aerodinamies kan verdowingspyle vebeter word deur eerder gebruik te maak van spin stabilisasie. Puntmassa en Gemodifiseerde-puntmassa neem aan die verdowingspyl is stabiel, wat nie noodwendig die geval is nie. Indien spin stabilisasie oorweeg word, stel ons Rigiede-liggaam simulasie voor as 'n grondslag om stabiliteit te bevestig.

Acknowledgements

I would like to express deepest gratitude to my supervisor Dr. Danie Els for his relentless support these past few years. His innate passion and curiosity for the field of engineering has been an inspiration throughout my studies and research.

Dedications

Hierdie tesis word opgedra aan my familie. Sonder hulle ondersteuning sou ek nie dié eindpunt bereik nie.

Contents

List of Figures

List of Tables

Nomenclature

Roman symbols

A	Characteristic area	[m^2]
$\mathbb{A}$	Sets of output parameters	[ ]
AL	Altitude	[m]
AZ	Azimuth	[deg]
a	Speed of sound	[m/s]
$\mathbb{B}$	Sets of input parameters	[ ]
DC	Drift correction	[rad]
d	Projectile diameter	[ ]
$\underline{\overline{\boldsymbol{E}}}$	Transformation matrix	[ ]
$\underline{\overline{\boldsymbol{E}_{313}}}$	Euler angle transformation matrix (z-x-z)	[ ]
$\underline{\overline{\boldsymbol{E}_{321}}}$	Euler angle transformation matrix (z-y-x)	[ ]
$\overline{\boldsymbol{e}_x}, \overline{\boldsymbol{e}_y}, \overline{\boldsymbol{e}_z}$	Body frame axes (unit vectors)	[ ]
$\overline{\boldsymbol{e}_X}, \overline{\boldsymbol{e}_Y}, \overline{\boldsymbol{e}_Z}$	World frame axes (unit vectors)	[ ]
$\mathbb{F}$	Sets of output functions	[ ]
F_D	Drag force	[N]
F_L	Lift force	[N]
F_{N_P}	Magnus force	[N]
$F_{N_{\dot{\alpha}+q}}$	Pitching force	[N]
$\overline{\boldsymbol{g}}$	Gravitational acceleration	[$\mathrm{m/s}^2$]
LA	Latitude	[deg]
M_α	Overturning moment	[N·m]
M_{L_P}	Roll dampening moment	[N·m]
M_{L_S}	Rolling moment	[N·m]
M_{N_P}	Magnus moment	[N·m]
$M_{\dot{\alpha}+q}$	Pitching moment	[N·m]
P	Pressure	[Pa]
P_s	Saturation pressure	[Pa]
q_0	Euler parameter scalar component	[ ]

$\overline{\boldsymbol{q}} = [q_1 \quad q_2 \quad q_3]$	Euler parameter vector component	[ ]
QE	Quadrant elevation	[rad]
$\underline{\overline{\boldsymbol{R}_x}}$	Elemental rotation around x axis	[ ]
$\underline{\overline{\boldsymbol{R}_y}}$	Elemental rotation around y axis	[ ]
$\underline{\overline{\boldsymbol{R}_z}}$	Elemental rotation around z axis	[ ]
Re	Reynolds number (diameter)	[ ]
Re_{crit}	Critical Reynolds number	[ ]
R_H	Relative humidity	[%]
r	Earth radius	[m]
S_d	Dynamic stability factor	[ ]
S_g	Gyroscopic stability factor	[ ]
s	Dimensionless arc length	[ ]
T	Temperature	[K]
T_w	Riffling twist rate	[Cal/turn]
$\overline{\boldsymbol{V}}$	Relative projectile velocity	[m/s]
$\overline{\boldsymbol{V}_\infty}$	Free stream velocity (wind)	[m/s]
V_m	Muzzle velocity	[m/s]
V_{WX}	Down range wind	[m/s]
V_{WY}	Cross range wind	[m/s]
$\overline{\boldsymbol{x}}$	Projectile location: Cartesian coordinates	[m]
$\dot{\overline{\boldsymbol{x}}}$	Translation velocity	[m/s]
$\ddot{\overline{\boldsymbol{x}}}$	Translation acceleration	[m/s^2]
$\overline{\dot{\boldsymbol{x}}_c}$	Earth curvature correction velocity	[m/s]
$\mathbf{Y}$	Projectile state vector	[deg]
$y+$	Dimensionless wall distance	[ ]

Greek symbols

α	Pitch	[rad]
α_0	Initial pitch (relative to barrel)	[rad]
α_t	Angle of attack	[rad]
β	Yaw	[rad]
β_0	Initial yaw (relative to barrel)	[rad]
β_R	Yaw of repose	[rad]
$\overline{\boldsymbol{\gamma}} = [\phi, \theta, \psi]$	Euler angles	[rad]
δ	Relative error	[ ]
δ_a	Humidity correction factor for speed of sound	[ ]

δ_ρ	Humidity correction factor for air density	[ ]
θ_{throw}	Lateral throw off angle	[rad]
θ_C	Lateral throw off, radial direction	[rad]
θ_{roll}	Initial roll angle	[rad]
$\overline{\mathbf{\Lambda}}$	Coriolis acceleration	$[\mathrm{m/s^2}]$
λ	Heat capacity ratio of air	[ ]
μ	Air viscosity	[Pa·s]
μ^*	Revised mean of elementary effects	[ ]
ρ	Air density	$[\mathrm{kg/m^3}]$
$\overline{\mathbf{\Omega}_E}$	Earth angular velocity	[rad/s]
$\overline{\boldsymbol{\omega}}$	Angular velocity	[rad/s]
$\dot{\overline{\boldsymbol{\omega}}}$	Angular acceleration	$[\mathrm{rad/s^2}]$
ξ	Pitch and yaw as single complex number	[rad]

Superscripts

E	Curved earth frame
b	Barrel frame
r'	Rotating body frame
r	Body frame
s	World frame

Abbreviations

BS	Bulirsch-Stöer
CFA	Computational fluid analysis
CFD	Computational fluid dynamics
ICAO	International Civil Aviation Organisation
RAD	Relative average deviation
RB	Rigid-body
RDDS	Remote drug delivery system
RK4	Runga-Kutta 4th order
RK54	Dorman-Prince embedded 5th order Runga-Kutta
MPM	Modified point-mass
PM	Point-mass

Chapter 1

Introduction

Remote Drug Delivery Systems (RDDS) allow long distance (> 15 m) administration of veterinary medication. The basic premise is as follows: a rifle launches a tranquilliser dart injecting its medication upon impact. RDDS made animal field studies and medical intervention routine procedure. Consequently advances in zoological/veterinary research are directly related to the refinement of RDDS (Bush, 1992).

1.1 Background

Rifles are either cartridge fired or gas based (PneuDart, 2020). Compressed gas rifles can vary their muzzle velocity by adjusting the gauge pressure. While useful to control impact velocity, aim (holdover) must also be adjusted accordingly. Figure 1.1 shows the compressed gas rifle manufactured by Pneu-Darts.

Figure 1.1: G2 X-Calibre gauged projector (Pneu-Dart, 2020)

Darts come in a wide array of designs and sizes (figure 1.2). They are routinely categorised based on injection method. The most common are air pressurised and percussion caps. Air pressurised darts are reusable, contrasting percussion caps that use an explosive charge and are thus single use (Rosenfield, 2017). No injection method is superior and choice depends on the operator's personal preference and cost.

Figure 1.2: Pneu-Dart Type C (Pneu-Dart, 2020)

The quality of the RDDS and skill of the operator can be measured using ethical distance.

1.1.1 Ethical distance

Reiterating the definition provided in Caudell *et al.* (2009) for more general applicability, ethical distance is the maximum range where impact is guaranteed to conform to preset constraints (in Caudell's case a humane kill). For RDDS, the criteria are successful injection and acceptable ballistic trauma. Estimating this range is difficult as each shot represents a unique event: type of dart, range, ambient conditions and animal all vary.

Injection

Upon impact, dart orientation and velocity must allow the needle to perforate the external epidermal layer. A perpendicular impact is preferred as intramuscular injection yields the fastest response. If the impact angle is sharp, perforation might be too shallow. In extreme cases the dart can ricochet, possibly inflicting greater injury (Rosenfield, 2017). Since trajectories are relatively flat, the impact angle is mostly dependent on the impact surface and dart stability.

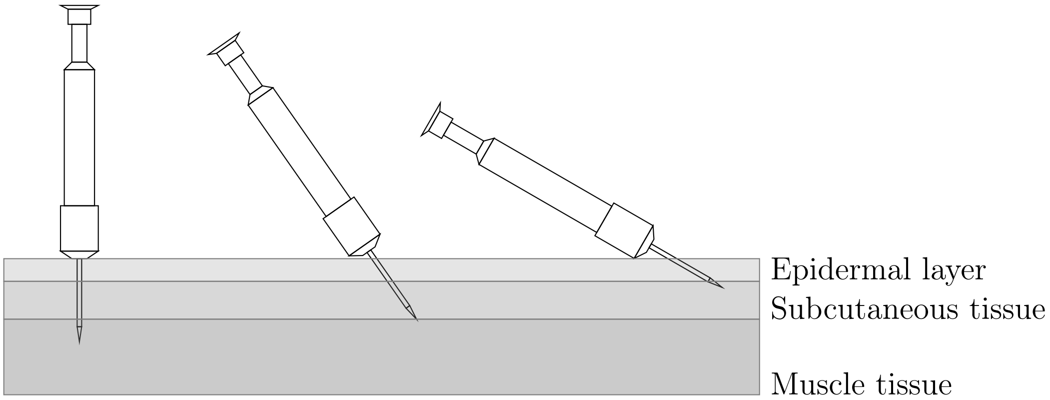

Figure 1.3: Injection angle

Ballistic trauma

RDDS are inherently intended to be non-lethal. Life threatening debilitation and/or death are however underestimated possibilities (Koene *et al.*, 2008). To regulate the impact energy, the target must be an appropriate distance from the RDDS operator. Too close and the physical trauma might be severe, too far and vulnerable areas such as eyes and joints become possible collateral damage (Hampton *et al.*, 2016). To facilitate this daunting task, manufacturers provide extensive tables with recommended pressures (muzzle velocities) and holdovers for various dosages and distances (Rosenfield, 2017).

1.2 Aeroballistics

Given sufficient information regarding the dart, it is possible to predict its flight behaviour. This entails quantifying the dart's interaction with the enveloping air: aerodynamic forces and moments.

1.2.1 Fluid: Ambient air

When the dart is in motion relative to the free stream, it forcefully displaces surrounding air. As per the Navier Stokes momentum equation, a change in fluid momentum implies the presence of forces (usually split into shear and pressure forces). As seen in equation 1.2, fluid density ρ and viscosity μ are needed to define fluid momentum (Schobeiri, 2010).

$$\overline{\boldsymbol{V}} = \dot{\overline{\boldsymbol{x}}} - \overline{\boldsymbol{V}}_\infty \neq 0 \tag{1.1}$$

$$\rho \frac{D\overline{\boldsymbol{V}}}{Dt} = -\nabla p + \rho \overline{\boldsymbol{g}} + \mu \nabla^2 \overline{\boldsymbol{V}} \tag{1.2}$$

To quantify these properties the ambient temperature, pressure and relative humidity at the projectile's location must be known (Gkritzapis *et al.*, 2007). For most practical applications, the free stream flow field is assumed to exclusively translate (V_∞). The relative velocity (V) is calculated using equation 1.1.

Flow regimes

Darts introduce disturbances that propagate throughout the free stream flow field at the speed of sound (a). When the propagation pattern is free of stochastic motion, the flow is laminar. When fully stochastic, the flow is turbulent. The regime is predicted using the Reynolds number, sufficiently high ($> Re_{crit}$) and the flow is fully turbulent. Close to Re_{crit}, the flow has an "intermittent characteristic": exhibits bursts of turbulence as the laminar motion becomes unstable (White, 2010).

$$Re = \frac{\rho V d}{\mu} \tag{1.3}$$

The characteristic length is the maximum external diameter (in this case, $d = 12.7\,\mathrm{mm}$). Most darts operate between $50\,\mathrm{m\,s^{-1}}$ and $90\,\mathrm{m\,s^{-1}}$. At mean sea level ambient conditions, darts have an average Re of 5×10^4. Darts are thus prototypical transitional or "low Reynolds number" problems (Anderson, 2009).

Transitional flow

At lower Reynolds numbers ($10^4 < Re < 10^5$) the boundary layer is laminar and thus prone to separate. When flow separation occurs, the already unstable flow becomes turbulent. The newly introduced shear stresses energise the flow, counteracting the pressure gradient and possibly reattaching the flow: known as a laminar separation bubble (Anderson, 2009). This makes transitional flow regimes difficult to accurately model using computational fluid analysis (CFA).

1.2.2 Projectile: Dart

The dart geometry dictates how the enveloping fluid is displaced. Darts are fairly blunt (excluding the needle) to distribute impact energy. This degrades aerodynamic performance by exacerbating drag and reducing flight stability. A stable projectile has a more predictable flight path as the angle of attack remains small: aerodynamic forces and moments are complex when instabilities are present.

1.3 Aerodynamic forces and moments

Aeroballisticians generally have the leisure of working with axis-symmetric projectiles. Taking advantage of this, the classical aeroballistic force and moment equations (tables 1.1 and 1.2) were developed (McCoy, 1999). Sections 1.3.1 through 1.3.7 elaborates on each individual force and moment.

For most practical applications, perfect axis-symmetry is a reasonable assumption. Ignoring the possibility of asymmetries would be remiss as they can effect on the trajectory. Section 1.5.5 discusses the possible consequences of asymmetries.

Table 1.1: Classic aerodynamic force equations

Force	**Equation**
Drag	$\overline{\boldsymbol{F}}_D = -\frac{C_D \rho A}{2} V \, \overline{\boldsymbol{V}}$
Lift	$\overline{\boldsymbol{F}}_L = \frac{C_L \rho A}{2} (\overline{\boldsymbol{V}} \times (\overline{\boldsymbol{e}_x} \times \overline{\boldsymbol{V}}))$
Pitching	$\overline{\boldsymbol{F}}_{N_{q+\dot{\alpha}}} = \frac{C_{N_{q+\dot{\alpha}}} \rho A}{2} \, d \, V \, \dot{\overline{\boldsymbol{e}_x}}$
Magnus	$\overline{\boldsymbol{F}}_{N_P} = \frac{C_{N_P} \rho A}{2} \, d \, (\overline{\boldsymbol{\omega}} \cdot \overline{\boldsymbol{e}_x})(\overline{\boldsymbol{V}} \times \overline{\boldsymbol{e}_x})$

Table 1.2: Classic aerodynamic moment equations

Moment	**Equation**
Overturning	$\overline{\boldsymbol{M}}_{\alpha} = \frac{C_{M_{\alpha}} \rho A}{2}\, d\, V (\overline{\boldsymbol{V}} \times \overline{\boldsymbol{e}_x})$
Pitching	$\overline{\boldsymbol{M}}_{M_{q+\dot{\alpha}}} = \frac{C_{M_{q+\dot{\alpha}}} \rho A}{2}\, d^2\, V (\overline{\boldsymbol{e}_x} \times \dot{\overline{\boldsymbol{e}_x}})$
Roll dampening	$\overline{\boldsymbol{M}}_{L_P} = \frac{C_{L_P} \rho A}{2}\, d^2\, V\, (\overline{\boldsymbol{\omega}} \cdot \overline{\boldsymbol{e}_x})\, \overline{\boldsymbol{e}_x}$
Rolling	$\overline{\boldsymbol{M}}_{L_S} = \frac{C_{L_S} \rho A}{2}\, d^2\, V^2\, \overline{\boldsymbol{e}_x}$
Magnus	$\overline{\boldsymbol{M}}_{M_P} = \frac{C_{M_P} \rho A}{2}\, d^2\, (\overline{\boldsymbol{\omega}} \cdot \overline{\boldsymbol{e}_x})(\overline{\boldsymbol{e}_x} \times (\overline{\boldsymbol{V}} \times \overline{\boldsymbol{e}_x}))$

Coefficients

The effects of geometry, inertia and flow regime are consolidated into the aeroballistic coefficients. The equations listed in tables 1.1 and 1.2 construe the fact that the coefficients are comprised of intricate non-linear relationships. Traditionally this relationship is expressed as a function of Mach number and angle of attack (α_t): equation 1.6 is commonly used to describe the non linear-influence of α_t at a set Mach number (Chaves *et al.* (2019), McCoy (1999)).

$$C_0 = f(\mathrm{Ma}) \tag{1.4}$$

$$C_2 = f(\mathrm{Ma}) \tag{1.5}$$

$$C = C_0 + C_2 \sin(\alpha_t)^2 + C_4 \sin(\alpha_t)^4 ... \tag{1.6}$$

Characteristics area

It can be any convenient value as long as it is clearly stated during the quantification of the aeroballistic coefficients. For axis-symmetric darts the accepted convention is to use the largest external diameter (d) to calculate the circular cross section.

$$A = \frac{\pi d^2}{4} \tag{1.7}$$

1.3.1 Drag

Drag is responsible for the dart's decrease in linear momentum. When small, a dart maintains its velocity and further distances are viable. Minimising drag is thus a primary concern when developing high performance projectiles.

$$\overline{\boldsymbol{F}}_D = -\frac{C_D \rho A V}{2} \overline{\boldsymbol{V}} \tag{1.8}$$

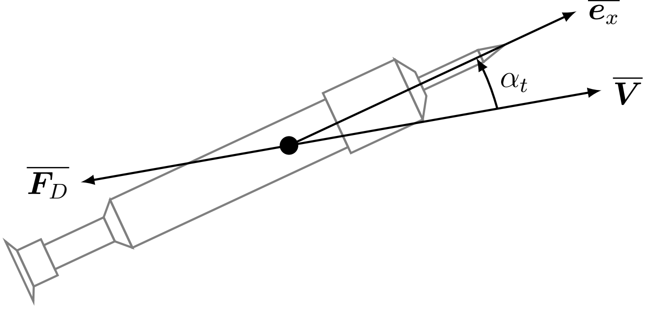

Figure 1.4: Drag

1.3.2 Lift

Asymmetric distribution of shear and pressure effects result in a force perpendicular to the relative free stream. This causes the dart to deflect laterally based on the dart's orientation. Lift is the largest contributor towards drift.

$$\overline{\boldsymbol{F}}_L = \frac{C_L \rho A}{2} (\overline{\boldsymbol{V}} \times (\overline{\boldsymbol{e}_x} \times \overline{\boldsymbol{V}})) \tag{1.9}$$

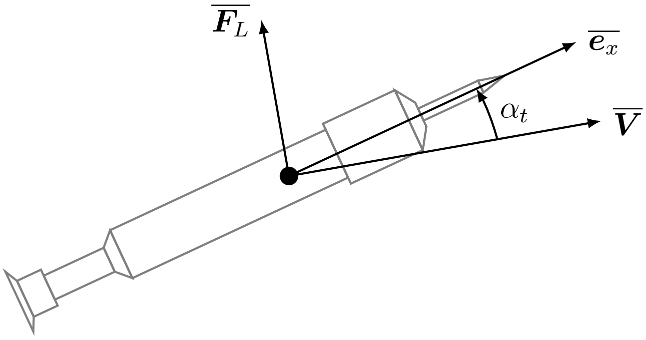

Figure 1.5: Lift

1.3.3 Overturning moment

As stated previously, surface shear and pressure effects are asymmetric. Additional to lift, the overturning moment is generated around the mass centre. When positive, the dart is considered statically unstable: will overturn without spin stabilisation (Tsien, 2012).

$$\overline{\boldsymbol{M}}_\alpha = \frac{C_{M_\alpha} \rho A \, d \, V}{2} (\overline{\boldsymbol{V}} \times \overline{\boldsymbol{e}_x}) \tag{1.10}$$

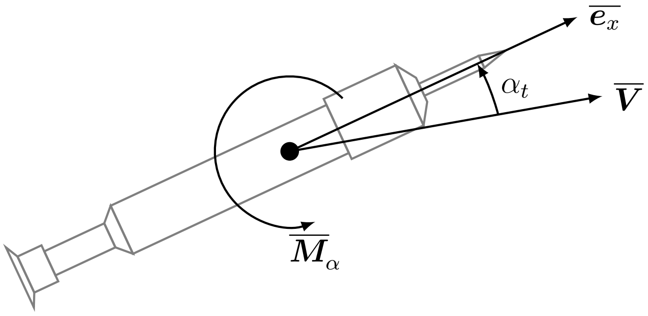

Figure 1.6: Overturning moment

To guarantee a negative value, darts are equipped with tailpieces (drag stabilisation). For high performance projectiles this is not viable as the additional drag is too severe. Spin stabilisation is more aerodynamically efficient but can be impractical if too high a spin rate is required (or when dart is dynamically unstable). Stability is discussed thoroughly in section 1.5.4.

1.3.4 Pitching force and moment

The dart “mixes” the surrounding air due to rapid changes in its symmetry axis (pitching and yawing). This motion is expressed by the derivative ($\dot{\overline{\boldsymbol{e}_x}}$) of the symmetry axis's unit vector. This is synonymous to a tangent line on the surface of a unit sphere (see figure 1.7). Air exercises a counteracting force and moment that dampen the motion. Both the force and moment are evaluated in the body frame using the Coriolis theorem: $\dot{\overline{\boldsymbol{e}_x}}$ becomes a function of the dart's pitching and yawing (ω_y, ω_z) (Hibbeler, 2010).

$$\overline{\boldsymbol{F}}_{N_{q+\dot{\alpha}}} = \frac{C_{N_{q+\dot{\alpha}}} \rho A \, d \, V}{2} \, \dot{\overline{\boldsymbol{e}_x}} \tag{1.11}$$

$$\overline{\boldsymbol{M}}_{M_{q+\dot{\alpha}}} = \frac{C_{M_{q+\dot{\alpha}}} \rho A \, d^2 \, V}{2} \left(\overline{\boldsymbol{e}_x} \times \dot{\overline{\boldsymbol{e}_x}} \right) \tag{1.12}$$

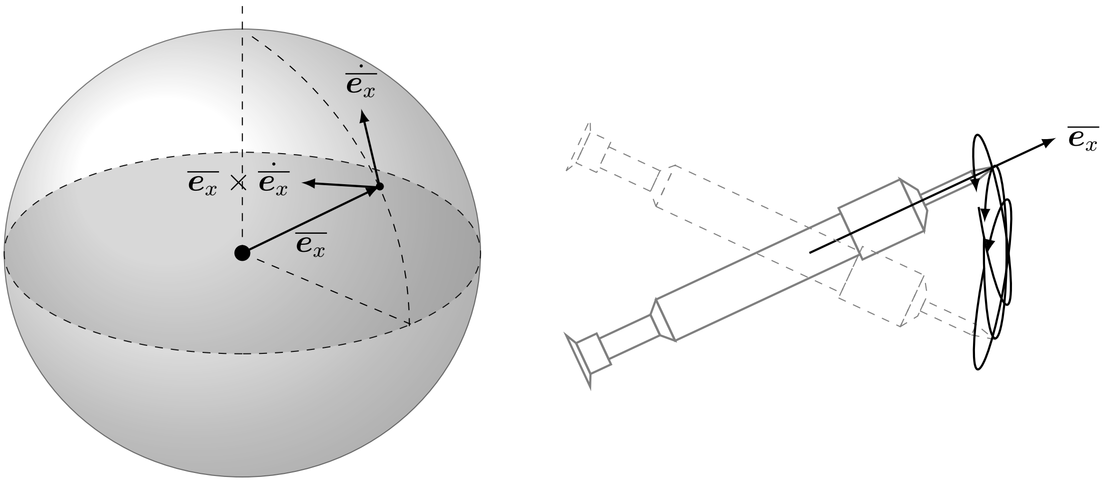

Figure 1.7: Pitching force and moment

1.3.5 Roll damping moment

This moment decreases the angular momentum around the symmetry axis. While not explicitly significant, spin stabilised darts can become unstable if the spin rate drops too low (gyroscopic stability).

$$\overline{\boldsymbol{M}}_{L_P} = \frac{C_{L_P} \rho A\, d^2\, V}{2} \left(\overline{\boldsymbol{\varpi}} \cdot \overline{\boldsymbol{e}_x}\right) \overline{\boldsymbol{e}_x} \tag{1.13}$$

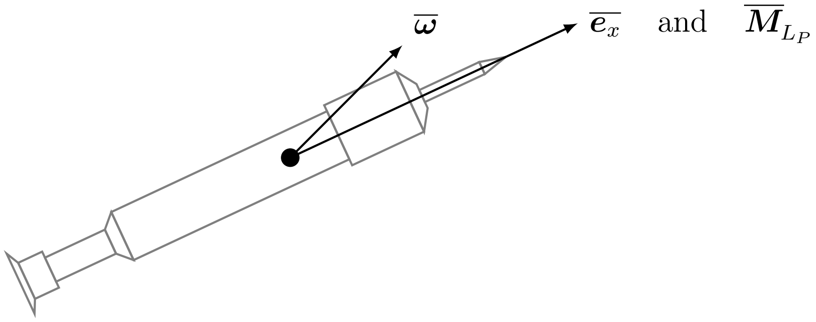

Figure 1.8: Roll damping moment

1.3.6 Rolling moment

If a dart needs to maintain axial spin, it can be equipped with fins. Fins induce a moment that increases axial momentum: accelerates spin.

$$\overline{\boldsymbol{M}}_{L_S} = \frac{C_{L_S} \rho A\, d^2\, V^2}{2} \overline{\boldsymbol{e}_x} \tag{1.14}$$

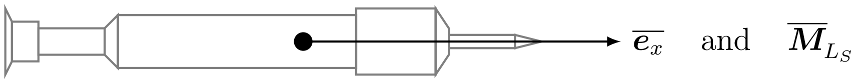

Figure 1.9: Rolling moment

1.3.7 Magnus force and moment

A rotating dart in a cross flow experiences perpendicular force and moment due to the Magnus effect. The axial spin deflects the cross flow laterally due to relative velocity differences on the dart's surface (Schobeiri, 2010).

$$\overline{\boldsymbol{F}}_{N_P} = \frac{C_{N_P} \rho A\, d}{2} (\overline{\boldsymbol{\omega}} \cdot \overline{\boldsymbol{e}_x})(\overline{\boldsymbol{V}} \times \overline{\boldsymbol{e}_x}) \tag{1.15}$$

$$\overline{\boldsymbol{M}}_{M_P} = \frac{C_{M_P} \rho A\, d^2}{2} (\overline{\boldsymbol{\omega}} \cdot \overline{\boldsymbol{e}_x})(\overline{\boldsymbol{e}_x} \times (\overline{\boldsymbol{V}} \times \overline{\boldsymbol{e}_x})) \tag{1.16}$$

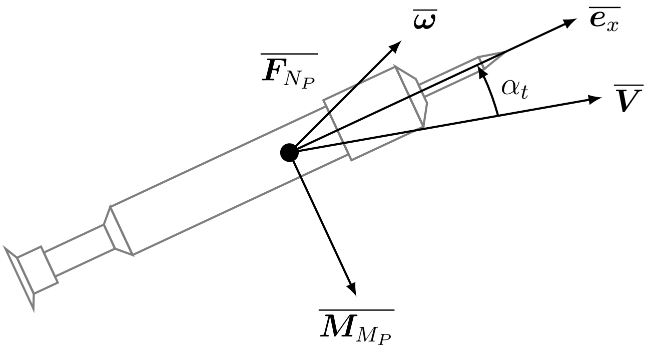

Figure 1.10: Magnus force and moment

1.4 Liquid payloads

A liquid payload exerts shear and pressure forces on the inner walls of the housing cavity, producing external moments on the dart. An axial moment is generated due to liquid spin up and a transverse moment from the sloshing effect: inertial waves propagate and collide with cavity walls. When these waves match the pitching and yawing motion of the housing, liquid resonance occurs and can cause catastrophic destabilisation. This is largely avoided by making sure there are no air cavities.

Several articles have been published that attempt to quantify these moments for axis-symmetric projectiles. Cooper and Costello (2011) used a well-developed spatial eigenvalue theory to generate liquid moment coefficients and incorporated them into a 6-DOF flight model. The analysis assumed that the projectile undergoes quasi-steady coning motion, which enables calculation of liquid moment coefficients as a function of *Re* and coning frequency. Rogers *et al.* (2013) improved on that concept by using a dual-spin projectile model to capture liquid spin-up after launch. Their validity is however questionable as no verification studies have been performed.

Due to its complexity, the effect of the liquid payload is assumed negligibly small and thus not taken into account for the remainder of this thesis.

1.5 Linearised projectile motion

Evident from the previous sections, a dart's equations of motion consist of highly non-linear differential equations. If the aerodynamic resistances and initial conditions are accurately known, an essentially exact solution is numerically available. Being simply a table of numbers, knowing how to improve a design is based on educated guesses. Alone, this approach can be very inefficient. Having access to a simplified closed form solution is recommended as each variable's contribution is stated explicitly: what must be changed to alter the dart's flight behaviour (stability criteria).

These analytical solutions have several other uses; confirm numerically solution is solved correctly; regression with experimental data to estimate coefficients. They are thoroughly documented in multiple publications (Chaves *et al.* (2019), McCoy (1999)).

1.5.1 Translational velocity

The full derivation for linearised velocity is given to show the application of dimensionless arc length (s). Only the final solutions for pitch, yaw and spin rate are presented.

$$s = \frac{1}{d} \int \dot{x} \tag{1.17}$$

For relatively short, windless ($V_\infty = 0$) distances the trajectory can be assumed straight and the drag coefficient (C_D) constant. Since the flight path is straight, gravity and lateral forces are negligible.

$$F = F_D = -\frac{C_D \rho A \, \dot{x}^2}{2} = m\ddot{x} \tag{1.18}$$

Linearising equation 1.18 in terms of s, it is solved using elementary 1st order differential equation solution methods. The solution (equation 1.19) suggests velocity decreases exponentially with distance traveled. Consequently small reductions in drag can exponentially improve maximum viable range.

$$s = \frac{1}{d}\int \dot{x}\,dt \qquad \frac{ds}{dt} = \frac{1}{d}\dot{x} \qquad dt = \frac{d}{\dot{x}}ds \qquad C_D^* = C_D\frac{\rho A\,d}{2m}$$

$$\begin{aligned}
\ddot{x} &= -C_D\frac{\rho A}{2m}\dot{x}^2 \\
\dot{x} &= -C_D\frac{\rho A}{2m}\int \dot{x}^2\,dt \\
\dot{x} &= -C_D\frac{\rho A\,d}{2m}\int \dot{x}\,ds \\
\dot{x} &= -C_D^*\int \dot{x}\,ds \\
\dot{x} &= \dot{x}_0\,e^{-C_D^*\,s}
\end{aligned} \tag{1.19}$$

The alternative solution as a function of time is:

$$\begin{aligned}
\ddot{x} &= -C_D\frac{\rho A}{2m}\dot{x}^2 \\
\dot{x}^{-2}\frac{d\dot{x}}{dt} &= -C_D\frac{\rho A}{2m} \\
\frac{1}{\dot{x}} - \frac{1}{\dot{x}_0} &= \left(C_D\frac{\rho A}{2m}\right)\times t \\
\frac{1}{\dot{x}} &= \left(C_D\frac{\rho A}{2m}\right)\times t + \frac{1}{\dot{x}_0}
\end{aligned} \tag{1.20}$$

1.5.2 Axial spin

The analytical solution for axial spin is derived in a similar fashion to equation 1.19. The result (equation 1.23) show that spin rate decays exponentially with distance traveled.

$$k_x^{-2} = \frac{md^2}{I_\mathrm{x}} \tag{1.21}$$

$$K_p = -\left[k_x^{-2}C_{L_P}^* + C_D^*\right] \tag{1.22}$$

$$\left(\frac{\omega_x d}{\dot{x}}\right) = \left(\frac{\omega_x d}{\dot{x}}\right)\Bigg|_0 e^{-K_p s} \tag{1.23}$$

1.5.3 Yaw and Pitch

Both pitch and yaw are collectively defined in terms of a single complex variable (ξ). Where β represents yaw and α pitch.

$$\xi = \alpha + \beta i \tag{1.24}$$

Through lengthly algebra the following equation is obtained. See either Chaves *et al.* (2019) or McCoy (1999) for its full derivation.

$$\xi = K_{F_0} e^{\lambda_F + i(\phi'_F s + \phi_F)} + K_{S_0} e^{\lambda_S + i(\phi'_S s + \phi_S)} + i\beta_R \tag{1.25}$$

Equation 1.25 indicates the symmetry axis traces an epicyclic pattern: two arms (K_F,K_S) each rotating at a unique frequency (ϕ'_F, ϕ'_S). Figure 1.11 is a visual representation of these components.

If there is no spin K_F and K_S are fixed in space. Lift then acts in a constant direction and produces a lateral deflection that increases quadratically with downrange distance. It is thus recommended to apply spin even if a dart is statically stable: lateral deflection primarily becomes a consequence of yaw of repose (β_R).

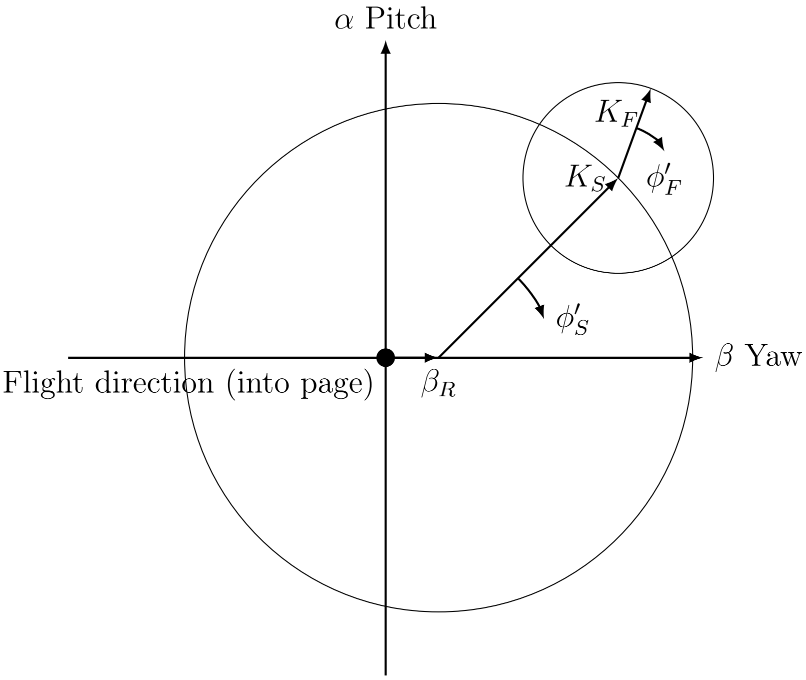

Figure 1.11: Linearised pitch and yaw

The performance of a dart is largely synonymous to its stability. When stable, aerodynamic resistance is less intricate resulting in a more predictable trajectory. Knowing how to achieve stability is thus of interest when developing a new dart. From equation 1.25, the classical flight stability criteria are derived. When presented in literature, authors are often presumptuous and assume the projectiles being investigated are statically unstable. The criteria are different based on static stability. Current tranquilliser dart's design are predominantly statically stable. If a more efficient design were investigated (spin stabilisation, tailpiece omitted) the dart will likely be statically unstable.

1.5.4 Stability

The exponents in equation 1.25 can cause the analytical pitch and yaw to grow without bound (instability). This forms the basis for the gyroscopic and dynamic stability criteria.

Gyroscopic stability

If the frequency exponents (ϕ'_F, ϕ'_S) in equation 1.25 contain imaginary variables, ξ will grow without bound. The gyroscopic stability criteria ensure the frequency exponents are real. It is customary to present the criteria in terms the gyroscopic stability factor S_g. The factor and criteria as found in Murphy (1954):

$$S_g = \frac{I_x^2 {\omega_x}^2}{2\rho d\, I_y A C_{M_\alpha} \dot{x}^2} \tag{1.26}$$

$$\text{Gyroscopic stability criteria} \begin{cases} S_g > 1, & \text{for } C_{M_\alpha} > 0 \\ S_g < 1, & \text{for } C_{M_\alpha} < 0 \end{cases} \tag{1.27}$$

It is worth noting that a statically stable dart is always gyroscopically stable regardless of spin: S_g is always negative $(C_{M_\alpha} < 0, S_g < 0)$. Being gyroscopically stable does not guarantee stability, simply that ϕ'_F and ϕ'_S will not cause destabilisation. If the damping coefficients λ_S or λ_F are positive, ξ will still grow without bounds regardless of gyroscopic stability.

Dynamic stabiliy

To ensure damping coefficients are negative, the dynamic stability criteria must be met. Criteria in terms of dynamic stability factor (S_d) as found in Murphy (1954):

$$S_d(2 - S_d) > \frac{1}{S_g} \tag{1.28}$$

$$S_d = \frac{2\left(C_L + k_x^{-2} C_{M_P}\right)}{C_L - C_D - k_y^{-2}\left(C_{M_q} + C_{M_a}\right)} \tag{1.29}$$

Figure 1.12 is a visual representation of both stability criteria (equations 1.27 and 1.28). It highlights that a statically unstable dart can only be stabilised if the dynamic stability factor is within $0 < S_d < 2$. The closer S_d is to 1, the easier the dart is to stabilise. When the dynamic stability factor is $S_d < 0$ or $S_d > 2$, too much spin will cause a statically stable dart to destabilise. Without information regarding a dart's dynamic stability factor, overzealously applying spin might thus be detrimental. When designing a new dart, the dynamic and gyroscopic stability criteria are guides on how to improve flight performance.

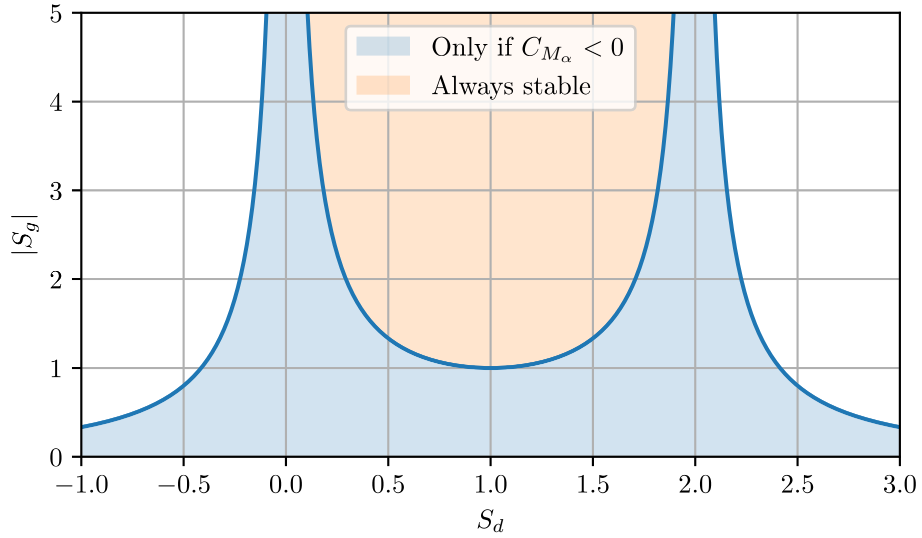

Figure 1.12: Stability regions

1.5.5 Limitations of stability criteria

The dynamic and gyroscopic stability criteria are derived for a perfectly rigid axis-symmetric projectile with a short and straight trajectory. They become less reliable when projectiles are asymmetric, over-stabilised, have liquid payloads or subjected to high ordinance trajectories.

Asymmetries

Spin stabilisation is a delicate phenomena that must be used with care. Consider a rigid body whose principal moments of inertia are $I_1 < I_2 < I_3$. It is mathematically shown it can be spin stabilised around one of its extrema principle axes (I_1 or I_3) (Wie, 2008). Spin around any intermediate axis is always unstable.

The dart is assumed axis-symmetric for the stability criteria ($I_2 = I_3$). The symmetry axis is then automatically an extrema principle axis (I_1). However darts are never perfectly axis-symmetric. In flight the spin axis will migrate to the true extrema principle inertia axis. When the true axes are parallel to the symmetry axes, the dart is statically unbalanced. When tilted, it is dynamically unbalanced. These states are not mutually exclusive and tend to occur together. Figures 1.13 and 1.14 show the implications of both instances during flight.

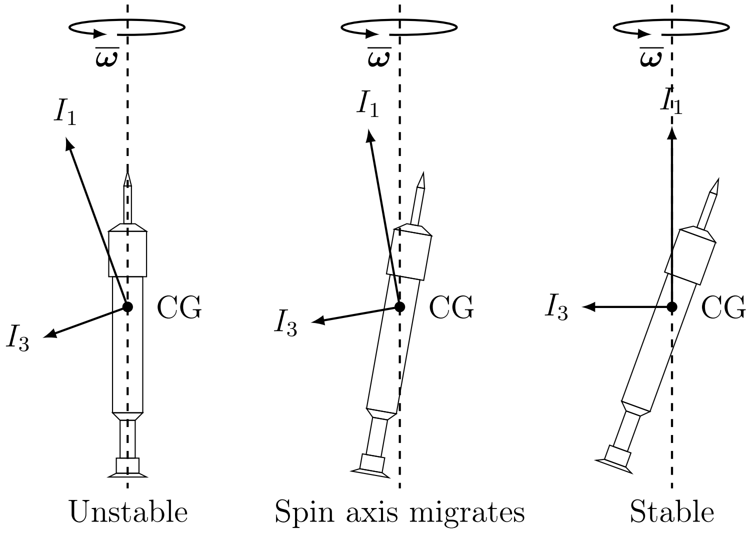

Figure 1.13: Dynamically unbalanced dart

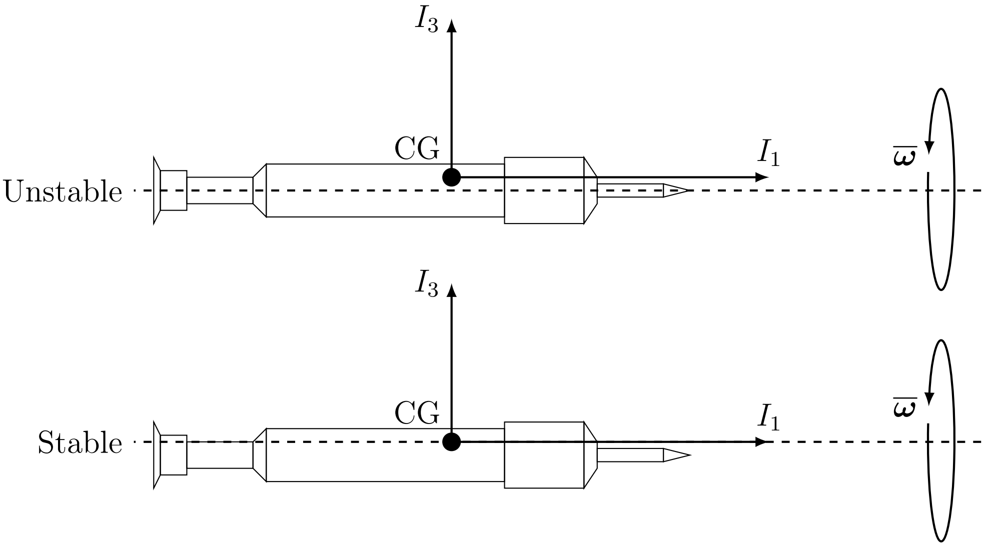

Figure 1.14: Statically unbalanced dart

Over stabilisation

There is a common misconception that a high spin rate is always beneficial. Excessive spin gyroscopically fixes the angular momentum vector, preventing the dart' s nose from following the flight arc. Since dart's trajectories are fairly straight, over stabilisation is less relevant in comparison to high ordinance projectiles.

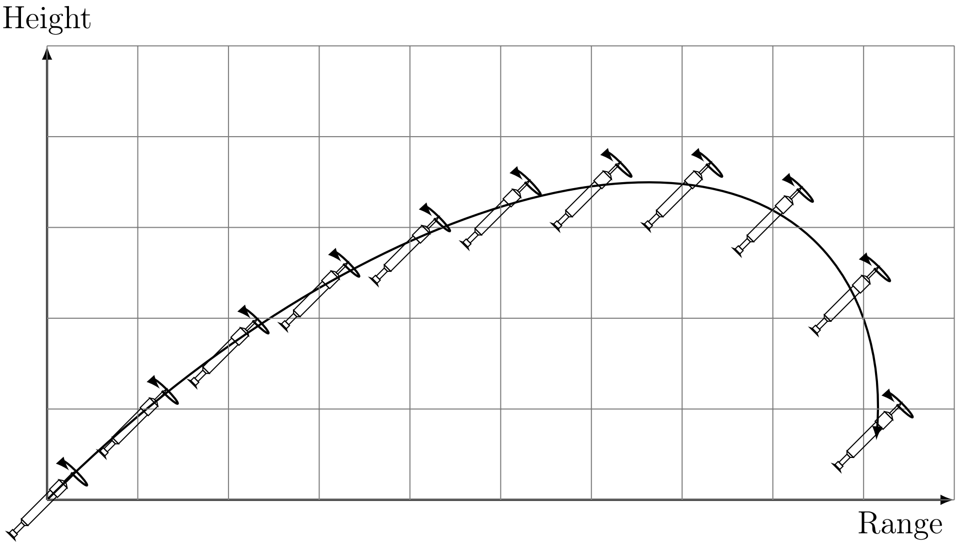

Figure 1.15: Over stabilisation

Liquid payloads

Despite being outside the scope of this thesis, its implications should be acknowledged. The stability criteria assume a dart is sufficiently presented by a rigid body. Liquid payloads inherently violate this assumption. The dart might be stable at the beginning of its trajectory but become unstable due to liquid resonance or gyroscopic/dynamic instability. Liquid resonance occurs when the sloshing of the liquid payload, matches the pitching and yawing of the housings. This can be avoided by confirmation that there are little to no air cavities.

Chapter 2

Projectile model

Several viable dart approximations exist with varying fidelity and data requirements. They are routinely split into three categories; Point-mass (PM); Modified point-mass (MPM) and Rigid body (RB) (Baranowski *et al.* (2016), Khalil *et al.* (2015), McCoy (1999)).

Sections 2.1-2.3 give the derivation of their equations of motion. The specifics of the numerical algorithm such as initial conditions, integration techniques, dense output and their implementation are discussed in chapter 3.

$$\boldsymbol{Y} = \begin{bmatrix} u_1 & u_2 & u_3 & ... \end{bmatrix}^T \tag{2.1}$$

$$\dot{\boldsymbol{Y}} = \begin{bmatrix} \dot{u}_1 & \dot{u}_2 & \dot{u}_3 & ... \end{bmatrix}^T \tag{2.2}$$

These are generalised equations and thus not exclusive to darts. Given the availability, all validations are done with the high speed, spin stabilised Sierra international bullet, as defined in appendix C, at mean sea level atmospheric conditions, with the following initial conditions; $V_m = 792.48\,\mathrm{m\,s^{-1}}$; $\omega_z = 25\,\mathrm{rad\,s^{-1}}$; $T_w = 12$ cal/turn.

Figure 2.1: Sierra international bullet

2.1 Point-mass

When approximating a dart as a PM, it is assumed to have no characteristic orientation or rotational inertia: equation of motion is derived using only conservation of linear momentum (Elsaadany and Wen-Jun, 2014) .

2.1.1 Equation of motion

Euler's 1^{st} law of motion states linear momentum remains constant unless compelled to change by external forces (Hibbeler, 2010).

$$\overline{\boldsymbol{F}} = \dot{\overline{\boldsymbol{L}}} \tag{2.3}$$

Substituting the linear momentum definition ($\overline{\boldsymbol{L}} = m\dot{\overline{\boldsymbol{x}}}$) the result is Newton's 2^{nd} law of motion.

$$\overline{\boldsymbol{F}} = m\ddot{\overline{\boldsymbol{x}}} \tag{2.4}$$

2.1.2 Aeroballistic forces

Without orientation or angular velocity, only drag, gravity, Coriolis effect and the earth's curvature effects can be applied. This exemplifies the advantage and disadvantage of using PM: easy to quantify but other potentially significant phenomena are neglected (modelling error).

2.1.3 State vector representation

When implemented numerically, the equations of motion are consolidated into state vectors. This promotes modularity and simplifies numerical integration and interpolation.

State vector:

$$\mathbf{Y}_{PM} = \begin{bmatrix} \overline{\boldsymbol{x}}^E \\ \dot{\overline{\boldsymbol{x}}}^s \end{bmatrix} \tag{2.5}$$

$$\dot{\mathbf{Y}}_{PM} = \begin{bmatrix} \dot{\overline{\boldsymbol{x}}}^E \\ \ddot{\overline{\boldsymbol{x}}}^s \end{bmatrix} = \begin{bmatrix} \dot{\overline{\boldsymbol{x}}}^s \\ m^{-1}\overline{\boldsymbol{F}}^s \end{bmatrix} + \begin{bmatrix} \dot{\overline{\boldsymbol{x}}_c}^s \\ \mathbf{0} \end{bmatrix} \tag{2.6}$$

PM forces:

$$\overline{\boldsymbol{F}}^s = \overline{\boldsymbol{F}_D}^s + m\,\overline{\boldsymbol{g}}^s + m\overline{\boldsymbol{\Lambda}}^s \tag{2.7}$$

2.1.4 Verification

In section 1.5, a projectile's velocity is expressed analytically (equation 1.19). This solution is colloquially referred to as a 1-DOF approximation: straight trajectory. Replicating this scenario in the numerical model, the drag coefficient is made constant and all other forces and influences are ignored ($g = 0, \Lambda = 0, x_c = 0$) . The identical results (figure 2.2), indicate that the PM approximation is implemented correctly.

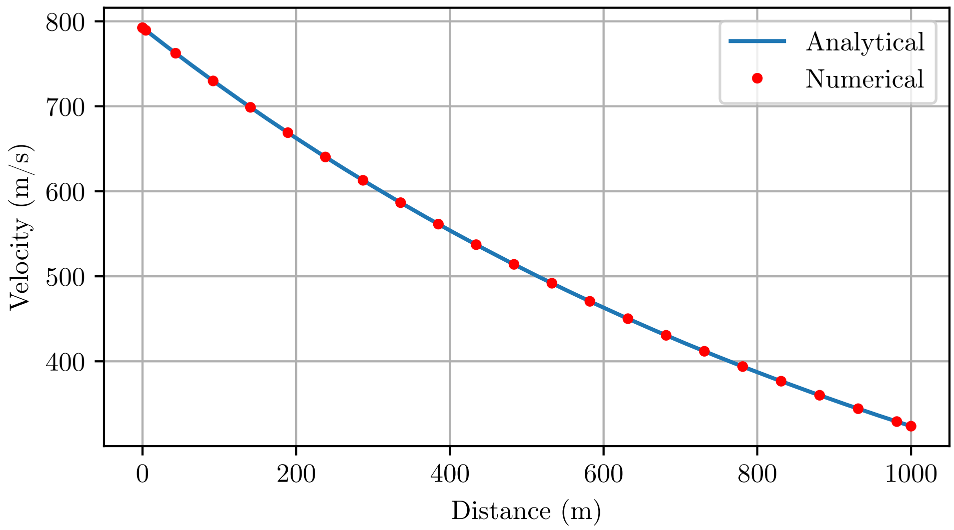

Figure 2.2: Point-mass: Analytical vs Numerical

2.2 Rigid-body

This sophisticated model expands on the PM approximation by also considering angular momentum. Quantifying angular momentum is far more laborious than its linear counterpart ($\overline{\boldsymbol{H}} = \underline{\boldsymbol{I}} \cdot \overline{\boldsymbol{\omega}}$).

2.2.1 Equation of motion

Euler's 2^{nd} law of motion indicates angular momentum remains constant unless compelled to change by an external moment (Hibbeler, 2010).

$$\overline{\boldsymbol{M}} = \dot{\overline{\boldsymbol{H}}} \tag{2.8}$$

$$\dot{\overline{\boldsymbol{H}}} = \overline{\boldsymbol{M}} = \dot{\underline{\boldsymbol{I}}} \cdot \overline{\boldsymbol{\omega}} + \underline{\boldsymbol{I}} \cdot \dot{\overline{\boldsymbol{\omega}}} \tag{2.9}$$

An inertia tensor defined in a stationary frame ($\underline{\boldsymbol{I}}^r$) changes as the body rotates ($\dot{\underline{\boldsymbol{I}}}^r \neq 0$). The Coriolis theorem circumvents the need to calculate this derivative.

Coriolis theorem states the time derivative of a vector observed from a fixed inertial frame ($\dot{\overline{\boldsymbol{x}}}^r$), is equal to the rate of change of the same vector as observed from a rotating frame ($\dot{\overline{\boldsymbol{x}}}^{r\prime}$) and adding the change resulting from the frame's angular velocity as observed from the inertial frame $\overline{\boldsymbol{\Omega}}^r$ (Hibbeler, 2010).

Applying the Coriolis theorem to the angular momentum derivative:

$$\dot{\overline{\boldsymbol{H}}}^r = \dot{\overline{\boldsymbol{H}}}^{r\prime} + \overline{\boldsymbol{\Omega}}^r \times \overline{\boldsymbol{H}}^r \tag{2.10}$$

Substituting the angular momentum definition ($\overline{\boldsymbol{H}} = \underline{\boldsymbol{I}} \cdot \overline{\boldsymbol{\omega}}$):

$$\overline{\boldsymbol{M}}^r = (\dot{\underline{\boldsymbol{I}}} \cdot \overline{\boldsymbol{\omega}} + \underline{\boldsymbol{I}} \cdot \dot{\overline{\boldsymbol{\omega}}})\Big|^{r\prime} + (\overline{\boldsymbol{\Omega}} \times \underline{\boldsymbol{I}} \cdot \overline{\boldsymbol{\omega}})\Big|^{r} \tag{2.11}$$

The rotating frame's angular velocity ($\overline{\boldsymbol{\Omega}}^r$), can be meticulously chosen to keep the inertia tensor constant.

$$\dot{\underline{\boldsymbol{I}}}^{r\prime} = 0 \tag{2.12}$$

$$\overline{\boldsymbol{M}}^r = (\underline{\boldsymbol{I}} \cdot \dot{\overline{\boldsymbol{\omega}}})\Big|^{r\prime} + (\overline{\boldsymbol{\Omega}} \times \underline{\boldsymbol{I}} \cdot \overline{\boldsymbol{\omega}})\Big|^{r} \tag{2.13}$$

Having the fixed inertial and rotating frame coincide, the equation reduces to the vector form of Euler's classic rigid body equation of motion.

$$\overline{\boldsymbol{M}}^r = (\underline{\boldsymbol{I}} \cdot \dot{\overline{\boldsymbol{\omega}}} + \overline{\boldsymbol{\Omega}} \times \underline{\boldsymbol{I}} \cdot \overline{\boldsymbol{\omega}})\Big|^{r} \tag{2.14}$$

When truly modelling a rigid body, the rotating frame follows the body exactly ($\overline{\boldsymbol{\Omega}} = \overline{\boldsymbol{\omega}}$). This substitution is however not performed as darts have symmetrical properties that can be exploited for numerical efficiency. This is explored later in this section.

Frames of reference

The dart's orientation cannot be directly solved from equation 2.14 as it is expressed in the body frame and information is only available in the world frame. Both concerns are addressed using an appropriate transformation matrix $\overline{\underline{\boldsymbol{E}}}$. Per definition, a transformation matrix consists of orthonormal vectors. These unit vector are principle axes of the intended frame relative to the current frame.

$$\overline{\underline{\boldsymbol{E}}}_r^s = \left[\overline{\boldsymbol{e}_x}^s \quad \overline{\boldsymbol{e}_y}^s \quad \overline{\boldsymbol{e}_z}^s\right] \tag{2.15}$$

$$\overline{\underline{\boldsymbol{E}}}_s^r = \left[\overline{\boldsymbol{e}_X}^r \quad \overline{\boldsymbol{e}_Y}^r \quad \overline{\boldsymbol{e}_Z}^r\right] \tag{2.16}$$

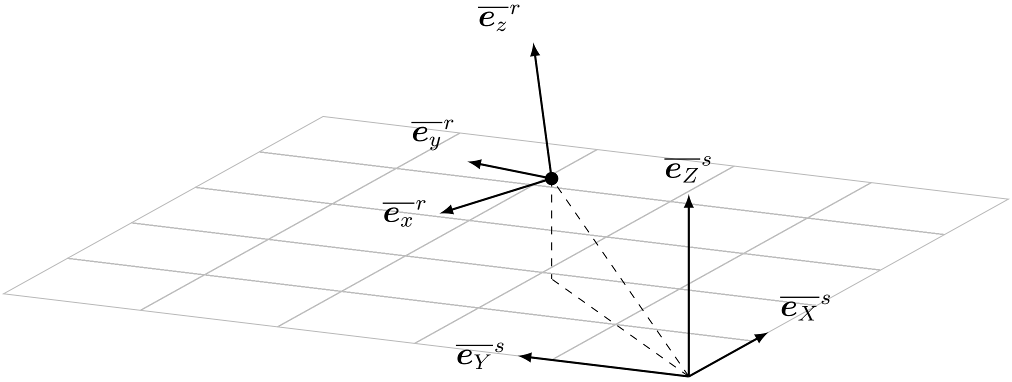

Figure 2.3: Frames of reference

The inverse of a transformation matrix is the backwards transformation matrix. Being orthonormal, the inverse matrix is simply its transpose.

$$\overline{\underline{\boldsymbol{E}}}_s^r \cdot \overline{\boldsymbol{x}}^s = \overline{\boldsymbol{x}}^r \tag{2.17}$$

$$\begin{aligned} \left[\overline{\underline{\boldsymbol{E}}}\right]^{-1} &= \left[\overline{\underline{\boldsymbol{E}}}\right]^T \\ \overline{\underline{\boldsymbol{E}}}_s^r &= \left[\overline{\underline{\boldsymbol{E}}}_r^s\right]^T \end{aligned} \tag{2.18}$$

In order to integrate the body's angular velocity, many parametrisation methods have been devised to define the attitude of the fixed body frame $\overline{\underline{\boldsymbol{E}}}_s^r$ relative to the world frame $\overline{\underline{\boldsymbol{E}}}_r^s$. The most noteworthy options being Euler symmetric parameters and Euler angles (Henderson, 1977).

Euler angles are intuitive and simple to apply but not numerically robust. The Euler symmetric parameters are numerically robust but conceptually abstract. Having access to both is advisable for validation and versatility.

Euler angles

Composed of three sequential rotations, the Euler angles describe the orientation of the body frame with respect to the world frame. Generally denoted as ϕ, θ, ψ.

$$\boldsymbol{\gamma} = \begin{bmatrix} \phi & \theta & \psi \end{bmatrix}^T \tag{2.19}$$

Each angle corresponds to a 3-dimensional rotation around a principle axis. The Euler angles are not unique and depend on the sequence of the elemental rotations around the x, y and z axes. Each rotation is mathematical computed using a corresponding elemental transformation matrix (Henderson, 1977).

Rotation around x axis:

$$\underline{\overline{\boldsymbol{R}_x}}(x) = \begin{bmatrix} 1 & 0 & 0 \\ 0 & \cos(x) & -\sin(x) \\ 0 & \sin(x) & \cos(x) \end{bmatrix} \tag{2.20}$$

Rotation around y axis:

$$\underline{\overline{\boldsymbol{R}_y}}(x) = \begin{bmatrix} \cos(x) & 0 & \sin(x) \\ 0 & 1 & 0 \\ -\sin(x) & 0 & \cos(x) \end{bmatrix} \tag{2.21}$$

Rotation around z axis:

$$\underline{\overline{\boldsymbol{R}_z}}(x) = \begin{bmatrix} \cos(x) & -\sin(x) & 0 \\ \sin(x) & \cos(x) & 0 \\ 0 & 0 & 1 \end{bmatrix} \tag{2.22}$$

The transformation matrix $\underline{\overline{\boldsymbol{E}_{313}}}$, is comprised of three rotations. The subscript 3-1-3 intuitively implies elemental rotations around the z, x and z axes. Abbreviating cos as c and sin as s the cumulative transformation matrix is:

$$\begin{aligned}
\underline{\overline{\boldsymbol{E}_{313}}}^{s}_{r}(\phi,\theta,\psi) &= \underline{\overline{\boldsymbol{R}_{z}}}(\phi)\cdot\underline{\overline{\boldsymbol{R}_{x}}}(\theta)\cdot\underline{\overline{\boldsymbol{R}_{z}}}(\psi) \\
&= \begin{bmatrix} c(\phi)c(\psi)-s(\phi)c(\theta)s(\psi) & -c(\phi)s(\psi)-s(\phi)c(\theta)c(\psi) & s(\phi)s(\theta) \\ s(\phi)c(\psi)+c(\phi)c(\theta)s(\psi) & -s(\phi)s(\psi)+c(\phi)c(\theta)c(\psi) & -c(\phi)s(\theta) \\ s(\theta)s(\psi) & s(\theta)c(\psi) & c(\theta) \end{bmatrix}
\end{aligned} \tag{2.23}$$

Since the "fixed " body frame orientation changes with time, the Euler angles must change accordingly (Greenwood, 2003). The corresponding derivative:

$$\dot{\gamma} = \begin{bmatrix} \dot{\phi} \\ \dot{\theta} \\ \dot{\psi} \end{bmatrix} = \underline{\overline{\boldsymbol{B}_{313}}}^{r}\cdot\overline{\boldsymbol{\Omega}}^{r} \tag{2.24}$$

$$\underline{\overline{\boldsymbol{B}_{313}}}^{r} = \frac{1}{\sin(\theta)}\begin{bmatrix} \sin(\psi) & \cos(\psi) & 0 \\ \sin(\theta)\cos(\psi) & -\sin(\theta)\sin(\psi) & 0 \\ -\cos(\theta)\sin(\psi) & -\cos(\theta)\cos(\psi) & \sin(\theta) \end{bmatrix} \tag{2.25}$$

Equation 2.24 must be used with care as it is susceptible to numerical instability: as θ approaches 0, equation $\underline{\overline{\boldsymbol{B}_{313}}}^{r}$ encroaches on a numerical singularity (tends towards infinity). This can be circumvented by switching to a different Euler angle parameterisation.

Euler symmetric parameters: Unit quaternions

The Euler symmetric parameters are a 4-dimensional extension of complex numbers consisting of a scaler (q_0) and vector ($\overline{\boldsymbol{q}}$) component. They are a convenient alternative to Euler angles since they are devoid of singularities.

$$(q_0, \overline{\boldsymbol{q}}) = q_0 + q_1\,\overline{\boldsymbol{i}} + q_2\,\overline{\boldsymbol{j}} + q_3\,\overline{\boldsymbol{k}} \tag{2.26}$$

$$\overline{\boldsymbol{q}} = q_1\overline{\boldsymbol{i}} + q_2\overline{\boldsymbol{j}} + q_3\overline{\boldsymbol{k}} \tag{2.27}$$

Three dimensional vectors are simply pure quaternions: zero scalar value (0,$\overline{\boldsymbol{q}}$). This pure quaternion is rotated using a triple Hamilton product.

$$\overline{\boldsymbol{V}}^{s} = (q_0, \overline{\boldsymbol{q}}) \diamond (\overline{\boldsymbol{V}}^{r}) \diamond (q_0, \overline{\boldsymbol{q}})^{-1} \tag{2.28}$$

The Hamilton product as defined in Crassidis and Markley (2003):

$$(a_0, \overline{\boldsymbol{a}}) \diamond (b_0, \overline{\boldsymbol{b}}) = \big(a_0 b_0 - \overline{\boldsymbol{a}} \cdot \overline{\boldsymbol{b}}, a_0\overline{\boldsymbol{b}} + b_0\overline{\boldsymbol{a}} + \overline{\boldsymbol{a}} \times \overline{\boldsymbol{b}}\big) \tag{2.29}$$

Inverse of a unit quaternion as defined in Crassidis and Markley (2003):

$$(q_0, \overline{\boldsymbol{q}})^{-1} = (q_0, -\overline{\boldsymbol{q}}) \tag{2.30}$$

Rewriting the arithmetic of equation 2.28 in terms of a rotation matrix $\underline{\overline{\boldsymbol{E}}}_r^s$.

$$\underline{\overline{\boldsymbol{E}}}_r^s = \begin{bmatrix} 2q_0^2 + 2q_1^2 - 1 & 2\,(q_1q_2 - q_3q_0) & 2\,(q_1q_3 + q_2q_0) \\ 2\,(q_1q_2 + q_3q_0) & 2q_0^2 + 2q_2^2 - 1 & 2\,(q_2q_3 - q_1q_0) \\ 2\,(q_1q_3 - q_2q_0) & 2\,(q_2q_3 + q_1q_0) & 2q_0^2 + 2q_3^2 - 1 \end{bmatrix} \tag{2.31}$$

Similar to the change in Euler angles, the change in quaternion values are a function of the body frame's angular velocity.

$$(\dot{q}_0, \dot{\overline{\boldsymbol{q}}}) = \frac{1}{2}(q_0, \overline{\boldsymbol{q}}) \diamond (0, \overline{\boldsymbol{\Omega}}^{r}) \tag{2.32}$$

Unit quaternions deviate from representing rotations when they lose their unit length. Being inevitable during numerical integration, regular normalisation is required. A computationally efficient approach is outlined in Greenwood (2003):

$$\begin{aligned} \epsilon &= q_0^2 + q_1^2 + q_2^2 + q_3^2 - 1 \neq 0 && (2.33) \\ f_q &= -\frac{\epsilon}{2}\,(q_0, \overline{\boldsymbol{q}}) && (2.34) \\ \text{Normalised quaternion} &= f_q + (q_0, \overline{\boldsymbol{q}}) && (2.35) \end{aligned}$$

2.2.2 Rigid-body aeroballistic forces and moments

The standardised aerodynamic forces and moments provided in tables 1.1 and 1.2 can be redefined to take advantage of the body frame ($\underline{\overline{\boldsymbol{E}}}_s^r$). The projectile geometrical symmetry axis $\overline{\boldsymbol{e}_x}^r$, is aligned with the x axis. Its derivative $\overline{\dot{\boldsymbol{e}}_x}^r$ is then only a function of transverse rotation (the Coriolis theorem).
The resulting body frame equations are listed in tables 2.1 and 2.2 . The complete absence of Ω_x indicates that both $\overline{\boldsymbol{F}}^r$ and $\overline{\boldsymbol{M}}^r$ are independent of the body frame's axial rotation. Consequently, for axis-symmetric darts, Ω_x can be disregarded without introducing modelling error. While rarely perfectly axis-symmetric, the assumption has substantial numerical benefits.

Table 2.1: Body frame expanded aerodynamic force equations

Force	**Equation**
Drag	$\overline{\boldsymbol{F}_D}^r = -\frac{C_D \rho A}{2} V \, \overline{\boldsymbol{V}}^r$
Lift	$\overline{\boldsymbol{F}_L}^r = \frac{C_L \rho A}{2} \left(\begin{bmatrix} V^2 & 0 & 0 \end{bmatrix}^T - V_x \overline{\boldsymbol{V}} \right) \Big\|^r$
Magnus	$\overline{\boldsymbol{F}_{N_P}}^r = \frac{C_{N_P} \rho A}{2} \, d \left(\omega_x \begin{bmatrix} 0 & V_z & -V_y \end{bmatrix}^T \right) \Big\|^r$
Pitch damping	$\overline{\boldsymbol{F}_{N_{q+\dot{\alpha}}}}^r = \frac{C_{N_{q+\dot{\alpha}}} \rho A}{2} \, d V \left(\begin{bmatrix} 0 & \Omega_z & -\Omega_y \end{bmatrix}^T \right) \Big\|^r$

Table 2.2: Body frame expanded aerodynamic moment equations

Moment	**Equation**
Overturning	$\overline{\boldsymbol{M}_{\alpha}}^{r} = \frac{C_{M_{\alpha}}\rho A}{2}\, d\, V \left(\begin{bmatrix} 0 & V_z & -V_y \end{bmatrix}^T \right) \Big\rvert^{r}$
Pitching	$\overline{\boldsymbol{M}_{M_{q+\dot{\alpha}}}}^{r} = \frac{C_{M_{q+\dot{\alpha}}}\rho A}{2}\, d^2\, V \left(\begin{bmatrix} 0 & \Omega_y & \Omega_z \end{bmatrix}^T \right) \Big\rvert^{r}$
Roll damping	$\overline{\boldsymbol{M}_{L_P}}^{r} = \frac{C_{L_P}\rho A}{2}\, d^2\, V \left(\begin{bmatrix} \omega_x & 0 & 0 \end{bmatrix}^T \right) \Big\rvert^{r}$
Rolling	$\overline{\boldsymbol{M}_{L_S}}^{r} = \frac{C_{L_S}\rho A}{2}\, d^2\, V \left(\begin{bmatrix} 1 & 0 & 0 \end{bmatrix}^T \right)$
Magnus	$\overline{\boldsymbol{M}_{M_P}}^{r} = \frac{C_{M_P}\rho A}{2}\, d^2 \left(\omega_x \begin{bmatrix} 0 & V_y & V_z \end{bmatrix}^T \right) \Big\rvert^{r}$

Axis-symmetric dart

If a dart is perfectly axis-symmetric, the inertia tensor is preserved in the body frame ($\dot{\overline{\underline{\boldsymbol{I}}}}^{r} = 0$) regardless of the frame's orientation about the symmetry axis: Ω_x can be included or disregarded interchangeably. The former is however computationally more efficient. For spin stabilised projectiles, ω_x is easily 3 orders of magnitude larger than ω_y or ω_z. Thus when $\Omega_x = 0$, equations 2.24 and 2.32 are significantly less stiff: needs fewer integration steps. When this simplification is enforced, it is known as a 5-DOF approximation.

$$\overline{\boldsymbol{\Omega}}^{r} = \begin{cases} \overline{\boldsymbol{\omega}}^{r} & \text{Asymmetric (6-DOF)} \\ \\ \begin{bmatrix} 0 & \omega_y & \omega_z \end{bmatrix}^T & \text{Axis-symmetric (5-DOF)} \end{cases} \tag{2.36}$$

It is interesting to note that for a perfectly spherical projectile, the inertia tensor is preserved regardless of $\overline{\boldsymbol{\Omega}}$: the rotating body frame's orientation can be stationary without introducing modelling error .

$$\overline{\boldsymbol{\Omega}}^{r} = \begin{bmatrix} 0 & 0 & 0 \end{bmatrix}^T \tag{2.37}$$

For the high velocity spin stabilised Sierra projectile, a 5-DOF simulation is on average 8 times faster. This decrease in computation time is invaluable for parametric analysis where several trajectories are evaluated. If not spin stabilised, the 5-DOF approximation does not yield the same computational benefit since ω_x (and thus Ω_x) is already 0. The 6-DOF approximation can thus be used without exacerbating computation time or error.

5-DOF approximation

If significant asymmetries are present, the inertia tensor is only preserved in the body body frame when $\overline{\boldsymbol{\Omega}}^r$ matches the body's angular velocity, $\overline{\boldsymbol{\omega}}^r$ (6-DOF).

$$\overline{\boldsymbol{\Omega}}^r = \begin{bmatrix} \omega_x & \omega_y & \omega_z \end{bmatrix}^T \tag{2.38}$$

To illustrate the modelling error, a slightly asymmetric, Sierra International bullet is simulated using both 5 and 6-DOF approximations. Figure 2.4 shows how the tricyclic wobble is replaced with an epicyclic motion when using the 5-DOF approach. In this case the asymmetries have minor effects on the trajectory and the 5-DOF model delivers qualitatively adequate results.

Initial conditions; $V_m = 792.48\,\mathrm{m\,s^{-1}}$; $\omega_z = 25\,\mathrm{rad\,s^{-1}}$; $T_w = 12$ cal/turn.

Inertia tensor for asymmetric Sierra International bullet:

$$\underline{\boldsymbol{I}}^r = \begin{bmatrix} 7.228e^{-1} & -3e^{-3} & -5e^{-4} \\ -3e^{-3} & 5.379 & -1e^{-3} \\ -5e^{-4} & -1e^{-3} & 5.379 \end{bmatrix} \times e^{-7}\ \mathrm{kg\,m^2} \tag{2.39}$$

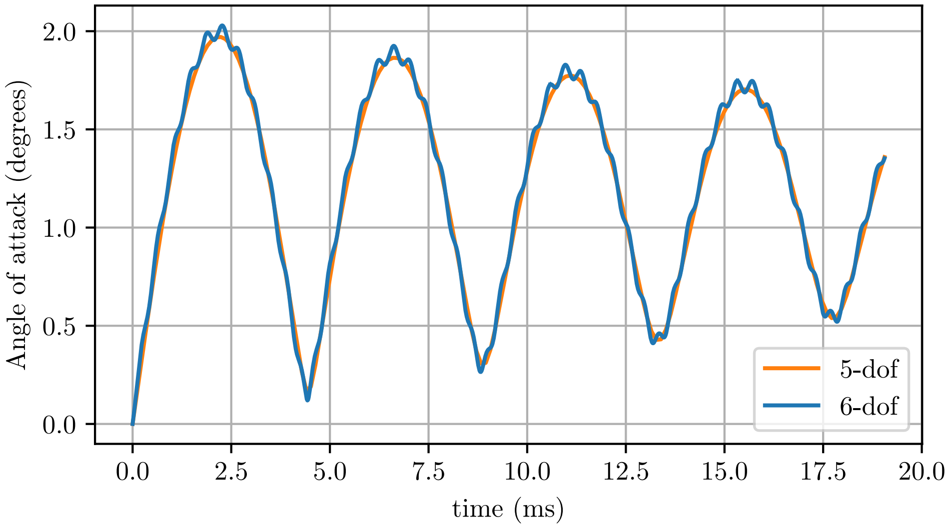

Figure 2.4: Modelling error of 5-DOF model

2.2.3 State vector representation

Consolidating the equations presented for the RB approximation, the following state vectors are concatenated. They can be numerically integrated to yield the dart's position, velocity, angular velocity and orientation.

State vector:

$$\boldsymbol{Y}_{RB} = \begin{bmatrix} \overline{\boldsymbol{x}}^{E} \\ \dot{\overline{\boldsymbol{x}}}^{s} \\ \gamma \text{ or } (q_0, \overline{\boldsymbol{q}}) \\ \overline{\boldsymbol{\omega}}^{r} \end{bmatrix} \tag{2.40}$$

$$\dot{\boldsymbol{Y}}_{RB} = \begin{bmatrix} \dot{\overline{\boldsymbol{x}}}^{E} \\ \ddot{\overline{\boldsymbol{x}}}^{s} \\ \dot{\gamma} \text{ or } (\dot{q}_0, \dot{\overline{\boldsymbol{q}}}) \\ \dot{\overline{\boldsymbol{\omega}}}^{r} \end{bmatrix} = \begin{bmatrix} \dot{\overline{\boldsymbol{x}}}^{s} \\ \\ m^{-1}\overline{\boldsymbol{F}}^{s} \\ \overline{\underline{\boldsymbol{B}_{313}}}^{r} \cdot \overline{\boldsymbol{\Omega}}^{r} \text{ or } \frac{1}{2}(q_0, \overline{\boldsymbol{q}}) \diamond (0, \overline{\boldsymbol{\Omega}}^{r}) \\ \underline{\overline{\boldsymbol{I}}}^{-1} \left(\overline{\boldsymbol{M}} - \overline{\boldsymbol{\Omega}} \times \underline{\overline{\boldsymbol{I}}}\overline{\boldsymbol{\omega}}\right) \Big|^{r} \end{bmatrix} + \begin{bmatrix} \overline{\dot{\boldsymbol{x}}_c}^{s} \\ \boldsymbol{0} \end{bmatrix} \tag{2.41}$$

The body frame's rotation is adjusted based on the darts geometry.

$$\overline{\boldsymbol{\Omega}}^{r} = \begin{cases} \overline{\boldsymbol{\omega}}^{r} & \text{Asymmetric (6-DOF)} \\ \begin{bmatrix} 0 & \omega_y & \omega_z \end{bmatrix}^{T} & \text{Axis-symmetric (5-DOF)} \\ \begin{bmatrix} 0 & 0 & 0 \end{bmatrix}^{T} & \text{Sphere} \end{cases} \tag{2.42}$$

RB force and moments:

$$\overline{\boldsymbol{F}}^{s} = \underline{\overline{\boldsymbol{E}}}_{r}^{s} \left(\overline{\boldsymbol{F}_D}^{r} + \overline{\boldsymbol{F}_L}^{r} + \overline{\boldsymbol{F}_{N_{q+\dot{\alpha}}}}^{r} + \overline{\boldsymbol{F}_{N_P}}^{r}\right) + m\overline{\boldsymbol{g}}^{s} + m\overline{\boldsymbol{\Lambda}}^{s} \tag{2.43}$$

$$\overline{\boldsymbol{M}}^{r} = \overline{\boldsymbol{M}_{\alpha}}^{r} + \overline{\boldsymbol{M}_{M_{q+\dot{\alpha}}}}^{r} + \overline{\boldsymbol{M}_{M_P}}^{r} + \overline{\boldsymbol{M}_{L_P}}^{r} + \overline{\boldsymbol{M}_{L_S}}^{r} \tag{2.44}$$

Verification

To confirm the model is correctly implemented and mathematically sound, its numerically predicted yaw and pitch are compared to the analytical approximation (equation 1.25). The same simplifications are imposed on the numerical model; trajectory is straight; velocity is constant; spin is constant; aeroballistic coefficients are constant; only select forces and moments are relevant ($F_L, M_\alpha, M_{\dot{\alpha}}, M_{N_P}$). The analytical and numerical solution yield nearly identical results (see figure 2.5).

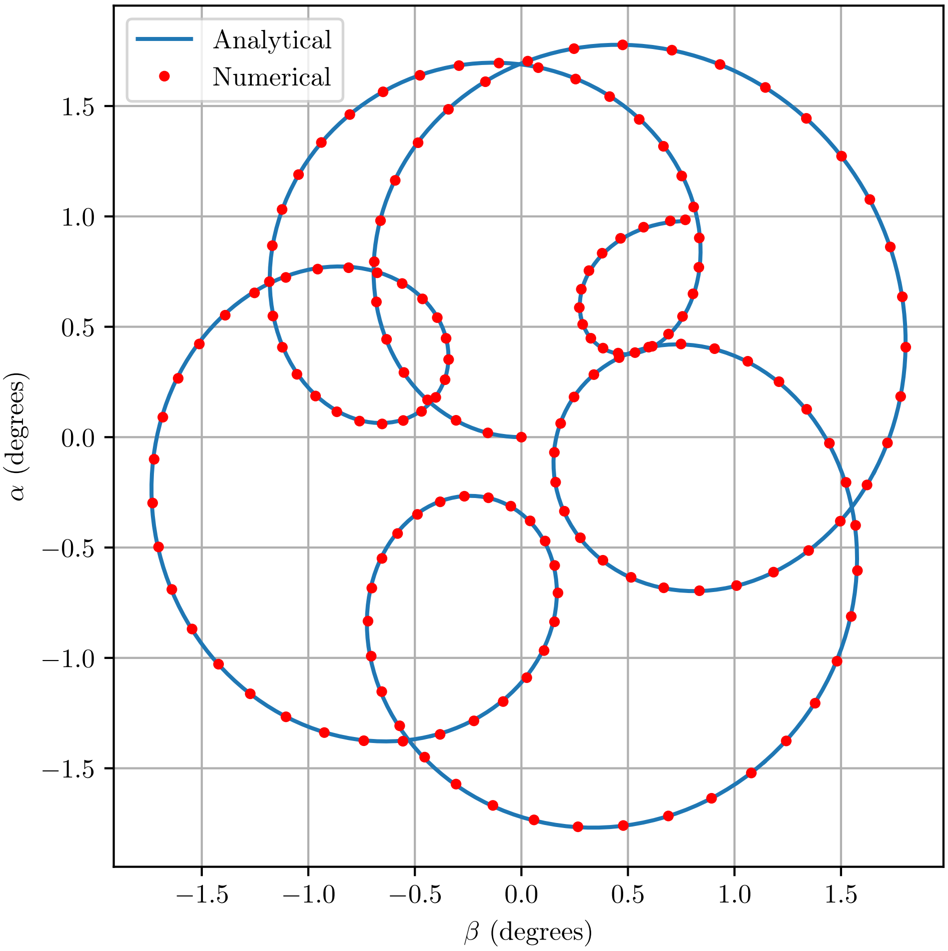

Figure 2.5: Rigid body: Analytical vs Numerical

2.3 Modified point-mass

After the initial transient pitching and yawing dampen out, the nearly imperceptible yaw of repose becomes visible. The dart's orientation lags behind the flight curve causing the spin axis to tilt towards the overturning moment vector (Bradly, 1990).

If the transient phase is considered infinitesimally small, the dart's orientation is sufficiently defined by the yaw of repose. The MPM method takes advantage of this, resulting in a computationally efficient projectile model that can approximate lateral forces such as lift and Magnus effect.

2.3.1 Yaw of repose

Substantial research is readily available on how to approximate the yaw of repose. The original expression published in Lieske and Reiter (1966) has undergone several iterations in the past few decades.

Original expression from Lieske and Reiter (1966).

$$\overline{\boldsymbol{\beta}}_R^s = \frac{-2I_x\omega_x C_L \left(\overline{\boldsymbol{V}}^s \times \ddot{\overline{\boldsymbol{x}}}^s\right) - 2md^2\omega_x C_{M_P} \left(\overline{\boldsymbol{V}}^s \times (\ddot{\overline{\boldsymbol{x}}}^s - \overline{\boldsymbol{g}}^s)\right)}{\rho A d V^2 \left(V^2 C_L C_{M_\alpha} + {\omega_x}^2 d^2 C_{N_P} C_{M_P}\right)} \tag{2.45}$$

A more efficient method was later devised by Bradly (1990):

$$\overline{\boldsymbol{\beta}}_R^s = \frac{2I_x\omega_x(\overline{\boldsymbol{g}}^s \times \overline{\boldsymbol{V}}^s)}{\rho A d V^4 C_{M_a}} \tag{2.46}$$

2.3.2 Equation of motion

MPM assumes the influence of pitching and yawing is minute. Consequently, in addition to translation, only axial spin needs to be quantified. MPM models are thus often referred to as 4-DOF models.

$$\begin{aligned} \dot{H}_x &= I_x\,\dot{\omega}_x = M \\ \dot{\omega}_x &= I_x^{-1} M \end{aligned} \tag{2.47}$$

2.3.3 Aeroballistic forces and moments

The classic aeroballistic forces and moments have unique expressions based on the yaw of repose. Despite not being listed in this table, the overturning moment is used to calculate the yaw of repose.

Table 2.3: Aerodynamic force and moment equations for MPM

Force	**Equation**
Drag	$\overline{\boldsymbol{F}_D}^s = -\dfrac{C_D \rho A}{2} V \, \overline{\boldsymbol{V}}^s$
Lift	$\overline{\boldsymbol{F}_L}^s = \dfrac{C_L \rho A}{2} V^2 \overline{\boldsymbol{\beta}}_R^s$
Magnus	$\overline{\boldsymbol{F}_{N_P}}^s = \dfrac{C_{N_P} \rho A}{2} d \, \omega_x (\overline{\boldsymbol{V}}^s \times \overline{\boldsymbol{\beta}}_R^s)$

Moment	**Equation**
Roll damping	$M_{L_P} = \dfrac{C_{L_P} \rho A}{2} \, d^2 \, V \, \omega_x$
Rolling	$M_{L_S} = \dfrac{C_{L_S} \rho A}{2} \, d^2 V$

2.3.4 State vector representation

Consolidating all the relevant equations, the state vectors for MPM are:

$$\mathbf{Y}_{MPM} = \begin{bmatrix} \overline{\boldsymbol{x}}^E \\ \dot{\overline{\boldsymbol{x}}}^s \\ \omega_x \end{bmatrix} \tag{2.48}$$

$$\dot{\mathbf{Y}}_{MPM} = \begin{bmatrix} \dot{\overline{\boldsymbol{x}}}^E \\ \ddot{\overline{\boldsymbol{x}}}^s \\ \dot{\omega}_x \end{bmatrix} = \begin{bmatrix} \dot{\overline{\boldsymbol{x}}}^s \\ m^{-1}\overline{\boldsymbol{F}}^s \\ I_x^{-1}M \end{bmatrix} + \begin{bmatrix} \dot{\overline{\boldsymbol{x}}_c}^s \\ \mathbf{0} \end{bmatrix} \tag{2.49}$$

MPM forces and moments:

$$\overline{\boldsymbol{F}}^s = \overline{\boldsymbol{F}_D}^s + \overline{\boldsymbol{F}_L}^s + \overline{\boldsymbol{F}_{N_P}}^s + m\overline{\boldsymbol{g}}^s + m\overline{\boldsymbol{\Lambda}}^s \tag{2.50}$$

$$M = M_{L_P} + M_{L_S} \tag{2.51}$$

Verification

As part of the linearised pitch and yaw solution presented in section 1.5, the yaw of repose is expressed analytically (equation 1.25). By imposing the same restrictions of the analytical solution on the numerical model, their solutions become comparable; aerodynamic coefficients constant; only $F_D, \overline{\boldsymbol{g}}, F_L, M_{L_P}$ are relevant. The numerical and analytical solutions give identical results (figure 2.6). This indicates MPM is correctly implemented and mathematically sound.

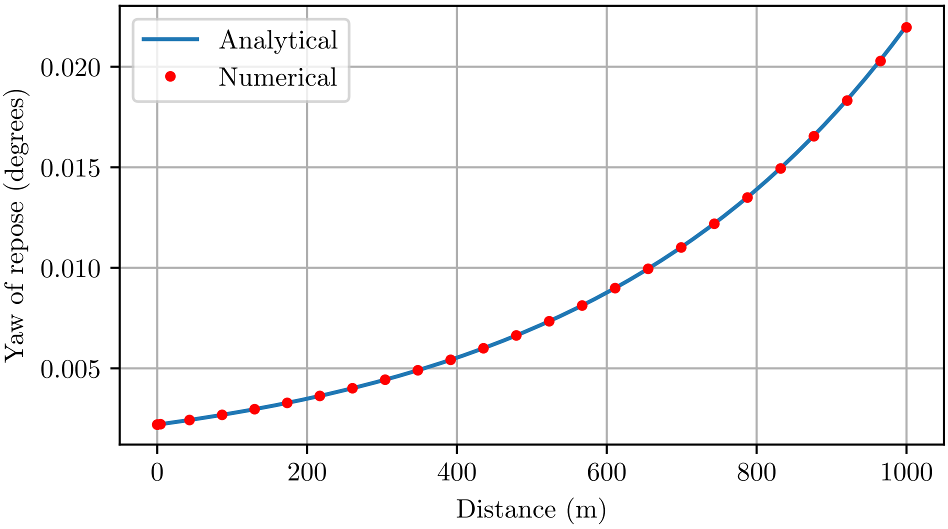

Figure 2.6: Modified point-mass: Analytical vs Numerical

Chapter 3

Trajectory simulation

A trajectory is simply a sequence state vectors, every point expressed by equation 3.1. With the appropriate initial conditions, numerical integration and termination criteria, entire trajectories are readily available. This chapter discusses the routines used to accomplish these aspects.

$$\boldsymbol{Y}\bigg|_{t} = \boldsymbol{Y}\bigg|_{t=0} + \int_{0}^{t} \dot{\boldsymbol{Y}} \tag{3.1}$$

3.1 World frame

Before any initial conditions can be quantified, the world frame origin and orientation must be concluded. The only prerequisite is an axis perpendicular to the Earth's surface: needed to define the gravity vector. For practicality the origin coincides with the rifle muzzle and $\overline{\boldsymbol{e}_X}$ points downrange towards the target.

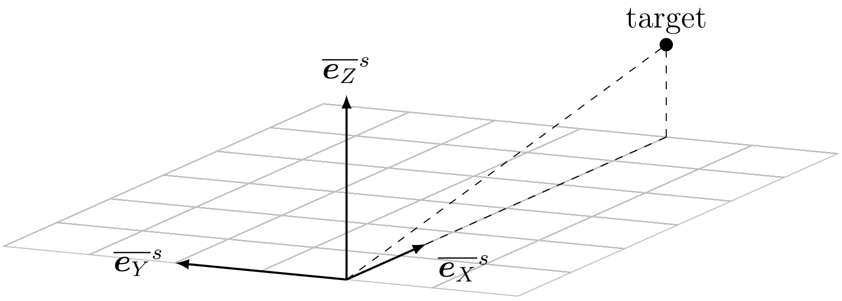

Figure 3.1: World frame orientation

3.2 Initial conditions

The predominant factors that define the dart's initial state are quadrant elevation, drift correction, twist rate and muzzle velocity (QE, DC, T_w, V_m). They define the launch state as intended by the operator (barrel orientation). From this barrel frame, additional considerations such as initial yaw, pitch and lateral throw-off can be seamlessly incorporated.

Barrel frame

The barrel's symmetry axis $(\overline{\boldsymbol{e}_{x_b}})$ is defined by quadrant elevation (QE) and drift correction (DC). Applying them to a 3-2-1 Euler anlge transformation the barrel frame $(\underline{\overline{\boldsymbol{E}}}_b^s)$ is defined. Despite having no rotation around the x axis, the component is retained to provide versatility.

$$\underline{\overline{\boldsymbol{E}}}_b^s = \underline{\overline{\boldsymbol{E}_{321}}}_b^s = f(DC, -QE, 0) = \begin{bmatrix} \overline{\boldsymbol{e}_{x_b}}^s & \overline{\boldsymbol{e}_{y_b}}^s & \overline{\boldsymbol{e}_{z_b}}^s \end{bmatrix} \tag{3.2}$$

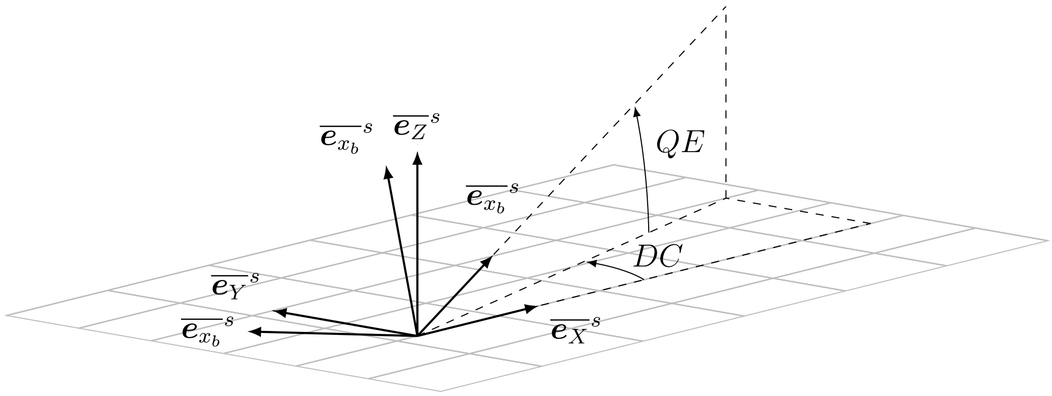

Figure 3.2: Barrel frame

$$\underline{\overline{\boldsymbol{E}_{321}}}_b^s = \begin{bmatrix} c(\theta_2)c(\theta_1) & -c(\theta_2)s(\theta_1) & s(\theta_2) \\ c(\theta_3)s(\theta_1) + c(\theta_1)s(\theta_3)s(\theta_2) & c(\theta_3)c(\theta_1) - s(\theta_3)s(\theta_2)s(\theta_1) & -c(\theta_2)s(\theta_3) \\ s(\theta_3)s(\theta_1) - c(\theta_3)c(\theta_1)s(\theta_2) & c(\theta_1)s(\theta_3) + c(\theta_3)s(\theta_2)s(\theta_1) & c(\theta_3)c(\theta_2) \end{bmatrix} \tag{3.3}$$

3.2.1 Position: $\overline{\boldsymbol{x}}$

Since the muzzle is the world frame origin, the initial condition is simply $\overline{\boldsymbol{0}}$.

$$\overline{\boldsymbol{x}}_0 = \overline{\boldsymbol{0}} \tag{3.4}$$

3.2.2 Velocity: $\dot{\boldsymbol{x}}^s$

For most applications the velocity vector is assumed collinear with the barrel. Deviation is possible due to static unbalance and manufacturing error. As the dart spins inside a rifled barrel, the axis of rotation is constrained to the geometrical symmetry axis. The gravity centre traces a helical pattern as the dart moves forward. When the dart exits the barrel, it literally flies off on a tangent. This phenomenon is known as lateral throw-off (Chaves *et al.*, 2019).

The resulting velocity vector is extracted from an adjusted barrel frame (3-2-1 Euler transformation). There is no standardised way to define these changes, it is however convenient to use a throw and roll angle $(\theta_{throw}, \theta_C)$.

$$\arctan \frac{V_t}{V_x} = \theta_{throw} \tag{3.5}$$

$$\dot{\boldsymbol{x}}^s = V_m \, \underline{\overline{\boldsymbol{E}_{321}}}(DC + \theta_{throw}, -QE, \theta_C) \cdot [1, 0, 0]^T \tag{3.6}$$

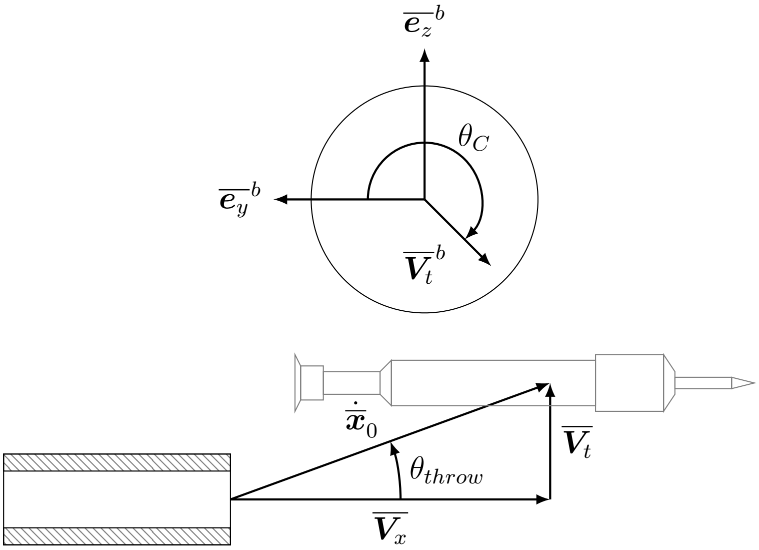

Figure 3.3: Lateral throw off

3.2.3 Orientation: γ and $(q, \overline{\boldsymbol{q}})$

Ideally the dart's orientation matches the barrel ($\underline{\overline{\boldsymbol{E}}}_b^s = \underline{\overline{\boldsymbol{E}}}_r^s$). It can be necessary to specify an initial yaw, pitch or roll angle ($\beta_0, \alpha_0, \theta_{roll}$). Similar to the velocity vector, the dart's orientation (body frame) is determined from an adjusted barrel frame (3-2-1 Euler transformation). The result (equation 3.7) is used to define the initial Euler angles or parameters.

$$\underline{\overline{\boldsymbol{E}}}_r^s\Big|_0 = \left[\underline{\overline{\boldsymbol{E}_{321}}}(DC + \beta_0, -(QE + \alpha_0), \theta_{roll})\right]^T \tag{3.7}$$

Initial 3-1-3 Euler angles

$$\begin{aligned} \tan(\phi_0) &= \frac{E_{13}}{-E_{23}} && (3.8) \\ \cos(\theta_0) &= E_{33} && (3.9) \\ \tan(\psi_0) &= \frac{E_{31}}{E_{32}} && (3.10) \end{aligned}$$

Initial Euler parameters

$$\begin{aligned} |2q_0| &= \sqrt{1 + E_{11} + E_{22} + E_{33}} && (3.11) \\ |2q_1| &= \sqrt{1 + E_{11} - E_{22} - E_{33}} && (3.12) \\ |2q_2| &= \sqrt{1 - E_{11} + E_{22} - E_{33}} && (3.13) \\ |2q_3| &= \sqrt{1 - E_{11} - E_{22} + E_{33}} && (3.14) \end{aligned}$$

For numerical accuracy, it is best to recalculate the Euler parameter based on the largest (absolute value) parameter found from $\underline{\overline{\boldsymbol{E}}}_r^s$ (Greenwood, 2003).

$$\begin{bmatrix} q_0 \\ q_1 \\ q_2 \\ q_3 \end{bmatrix} = \begin{bmatrix} \frac{|2q_0|}{2} \\ \frac{E_{32}-E_{23}}{2|2q_0|} \\ \frac{E_{13}-E_{31}}{2|2q_0|} \\ \frac{E_{21}-E_{12}}{2|2q_0|} \end{bmatrix} \text{ or } \begin{bmatrix} \frac{E_{32}-E_{23}}{2|2q_1|} \\ \frac{|2q_1|}{2} \\ \frac{E_{12}+E_{21}}{2|2q_1|} \\ \frac{E_{13}+E_{31}}{2|2q_1|} \end{bmatrix} \text{ or } \begin{bmatrix} \frac{E_{13}-E_{31}}{2|2q_2|} \\ \frac{E_{12}+E_{21}}{2|2q_2|} \\ \frac{|2q_2|}{2} \\ \frac{E_{23}+E_{32}}{2|2q_2|} \end{bmatrix} \text{ or } \begin{bmatrix} \frac{E_{21}-E_{12}}{2|2q_3|} \\ \frac{E_{13}+E_{31}}{2|2q_3|} \\ \frac{E_{23}+E_{32}}{2|2q_3|} \\ \frac{|2q_3|}{2} \end{bmatrix} \tag{3.15}$$

3.2.4 Angular velocity: $\overline{\boldsymbol{\omega}}^r$

Angular velocity is dictated by rifling twist rate, T_w (equation 3.16). Transverse rotation (ω_y, ω_z) is possible due to blow by, dynamic unbalance or a poor quality muzzle. Neither ω_y or ω_z are explicitly known and are usually estimated to achieve the maximum pitch/yaw measured experimentally. By definition they are pre-defined in the body frame.

$$\omega_x = \dot{x}_0 \frac{2\pi}{T_w\, d} \tag{3.16}$$

3.3 Integration

Initial conditions are propagated forward in time through numerical integration. Two major types are explored, namely Runge-Kutta methods and Richardson extrapolation. Runge-Kutta methods combine information from several Euler-style steps to complete a higher order Taylor series expansion. They tend to outperform most methods when accuracy requirements are not ultra stringent ($< 10^{-8}$) (Press and Teukolsky (1992),Sandvik (2018)).

3.3.1 Classic 4^{th} order Runge-Kutta

The classic 4th order Runge-Kutta (RK4) is still used in many modern ballistic models: such as those seen in Elsaadany and Wen-Jun (2014), Gkritzapis and Kaimakamis (2008) and Hainz and Costello (2005). This section explores why RK4 has retained its prevalence despite not being the most efficient or accurate approach. The algorithm is implemented as outlined in Press *et al.* (2007).

Performance evaluation

To gauge the performance of RK4, the Sierra international bullet's (as defined in appendix C) first 100 m of flight is simulated with the following initial conditions; $V_m = 792.48\,\mathrm{m\,s^{-1}}$; $\omega_z = 25\,\mathrm{rad\,s^{-1}}$; $T_w = 12$ cal/turn. Both runtime and result are compared to a high tolerance ($tol = 1e^{-15}$) Bulirsch Stöer extrapolation (BS).

$$\text{Relative error} = f(h) = \max\left(\frac{|\mathbf{Y}_{RK4}(h) - \mathbf{Y}_{BS}|}{|\mathbf{Y}_{BS}|}\right) \tag{3.17}$$

$$\text{Normalised wall-clock time} = f(h) = \frac{t_{RK4}(h)}{t_{BS}(tol = 1e^{-15})} \tag{3.18}$$

There is clear convergence with increase runtime (figure 3.4). Thus, while perfectly adequate results can be obtained with RK4, without a convergence study the reliability of the results are unknown. Errors can be large when underestimating the needed step size but being overly conservative disproportionally exacerbates computational costs.

For the same amount of wall-clock time as BS ($tol = 1e^{-15}$), RK4 achieved a relative error of $1e^{-5}$ (figure 3.4). For most aeroballistic problems, uncertainty overshadows numerical integration error (shown in section 4.2). Consequently if accuracy is the primary concern, refining the model inputs supersede the integration algorithm: hence why it is often acceptable to use RK4. If computational efficiency is of interest (such as parametric studies), it is worth having access to more efficient algorithms. To fill this need, Embedded Runge-Kutta 5(4) (RK54) and BS are useful alternatives depending on the needed accuracy.

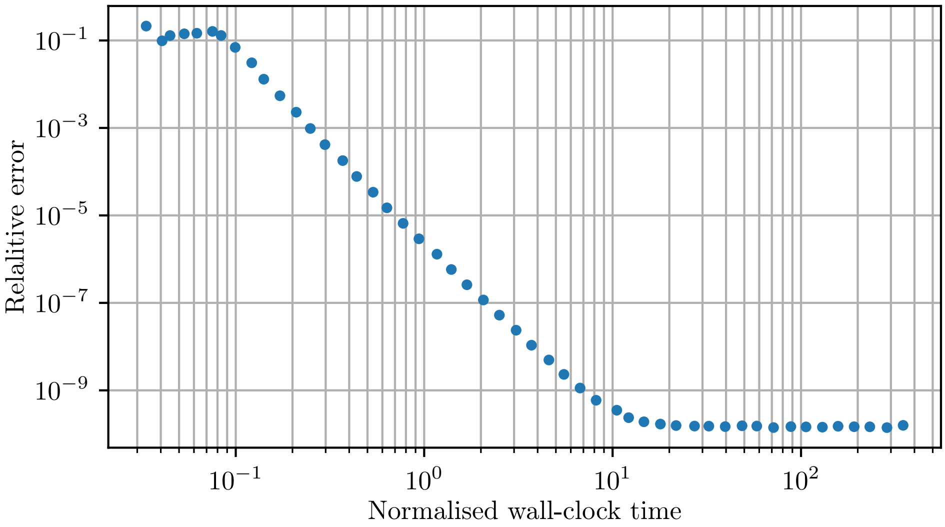

Figure 3.4: Normalised wall-clock time of classic Runge-Kutta

3.3.2 Embedded Runge-Kutta 5(4)

In order to address some of the computational and accuracy restrictions of RK4, adaptive step size control is usually implemented. Small meticulous steps crawl around "corners" while a great strides speed through smooth regions. Adaptive step size control requires the algorithm to gauge its performance: comparing the results of a higher and lower order Runge-Kutta. The preposition "embedded" refers to the lower order Runge-Kutta being extracted from the higher order Runge-Kutta.

This variant (Dormand-prince) increases its computational efficiency by applying “first same as last” (FSAL): the final function evaluation is also the first evaluation of the following step. Since it would have been evaluated in any case, it costs nothing. The algorithm is implemented as outlined in Press *et al.* (2007).

Adaptive step size can however be counterintuitive due to equation stiffness: steps need to be small to prevent numerical instabilities. The result is a disproportionate increase in function evaluations, computation time and numerical error.

Performance evaluation

RK54 outperforms BS when step tolerances larger than 10^{-10} are acceptable. The same case study used in RK4, is evaluated using incrementally smaller tolerances with both BS and RK54. Figure 3.5 shows that for higher accuracies BS was 4 times faster.

$$\text{Wall-clock time ratio} = f(tol) = \frac{t_{RK54}(tol)}{t_{BS}(tol)} \tag{3.19}$$

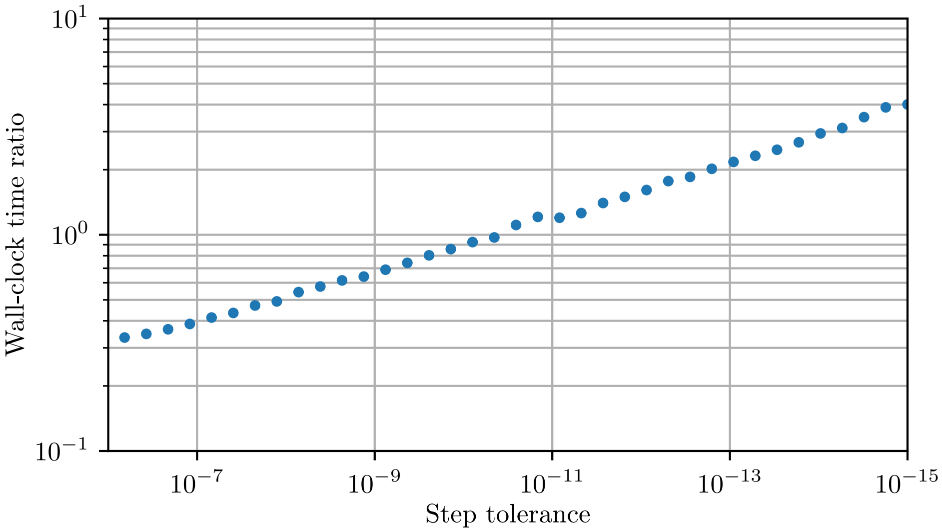

Figure 3.5: Embedded Runge-Kutta 5(4) runtime wall-clock time

3.3.3 Bulirsch-Stöer extrapolation

These methods use the idea of extrapolating the value that would be obtained if the step size was smaller than it actually is. In particular, extrapolation to a zero step size. Initial estimates are made using the modified midpoint method. The hypothetical zero step size state vector is then extrapolated using the Aitkens-Neville algorithm. The integrator is implemented as advised by Press *et al.* (2007).

Performance evaluation

BS excels when accuracy constraints are stringent. This can become necessary when working with particularly complex 6-DOF trajectories. To illustrate the complications, the previous Sierra international bullet case study is investigated using both 5-DOF and 6-DOF approximations. Being an axisymmetric projectile, both should yield identical results: differences are the result of numerical error.

$$\text{Relative error} = f(tol) = \max\left(\frac{|\boldsymbol{Y}(tol) - \boldsymbol{Y}_{5DOF}(tol = 1e^{-15})|}{|\boldsymbol{Y}_{5DOF}(tol = 1e^{-15})|}\right) \tag{3.20}$$

Figure 3.6 shows the relative error is 2 orders of magnitude larger when using the 6-DOF model. The error can be attributed to equation stiffness. This suggests that a 6-DOF simulation should be avoided unless the situation specifically requires it: such as investigating the influence of asymmetries.

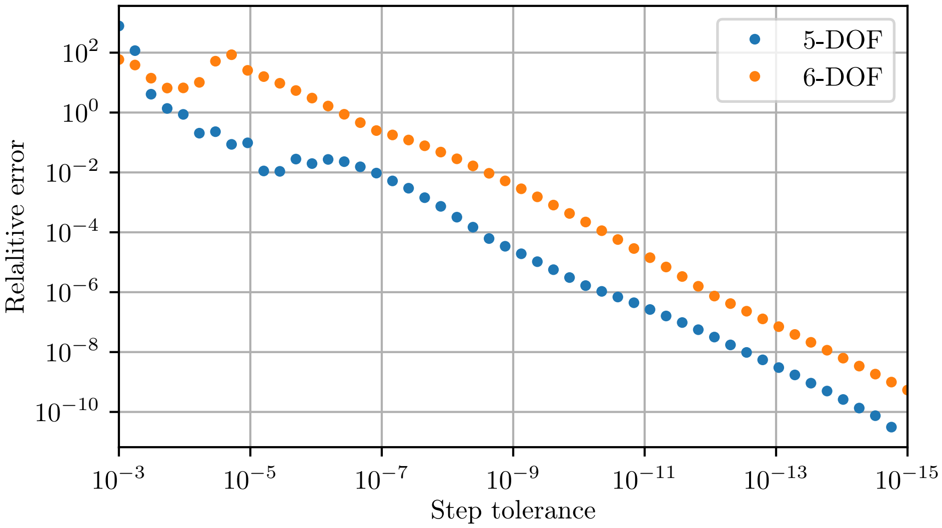

Figure 3.6: Comparison of 5-DOF and 6-DOF relative error

3.4 Termination criteria

When simulating a trajectory it is usually not explicitly known how far to integrate. The algorithm marches along till the state vector ($\boldsymbol{Y}$) conforms to some predetermined constraint: the moment of impact. Termination criteria as an inequality:

$$||x_{target}|| < ||x_i|| \tag{3.21}$$

The state vector that conforms to the constraint might actually have significant “overshoot”, especially when adaptive step size is employed. For most uses, this is acceptable, however if the dart's state at the exact moment of impact is needed (if investigating impact angle), some form of interpolation is necessitated.

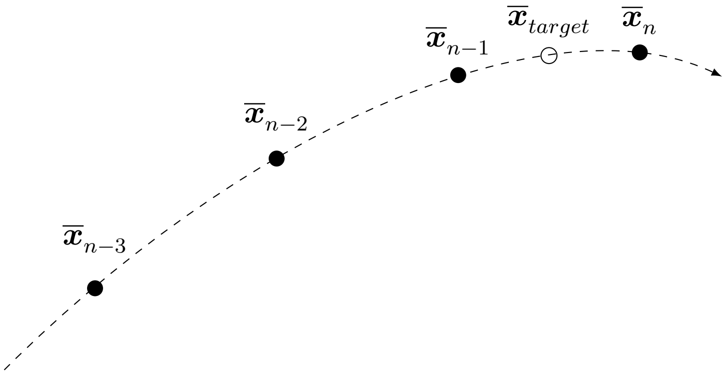

Figure 3.7: Termination criteria overshoot

To preserve the integration algorithm's order of accuracy, Press *et al.* (2007) recommends rewriting the last integration step as function of which the optimal step size is the root. Any root-finding algorithm such as Bisection, Newton or Secant can then be used to solve the optimal step size.

3.5 Dense output

While the points provided by the integration algorithm is usually sufficient, it is often desirable to be able to define any arbitrary point along the trajectory. This is especially necessary for BS where steps are extremely large due to the high orders invoked. While the root finding approach discussed previously is feasible for arbitrary points along the trajectory, it is computationally expensive and therefore should be reserved for the point of impact.

Press *et al.* (2007) suggests using cubic Hermite interpolation as it matches a function in both observed value and derivative $(\boldsymbol{Y}, \dot{\boldsymbol{Y}})$. Any method will suffice given enough points but Hermite interpolation excels even when steps are sparse. Figure 3.8 shows the dense output obtained with BS. Interpolation algorithms do not natively preserve the unity of Euler parameters, for better accuracies the interpolated values must be normalised.

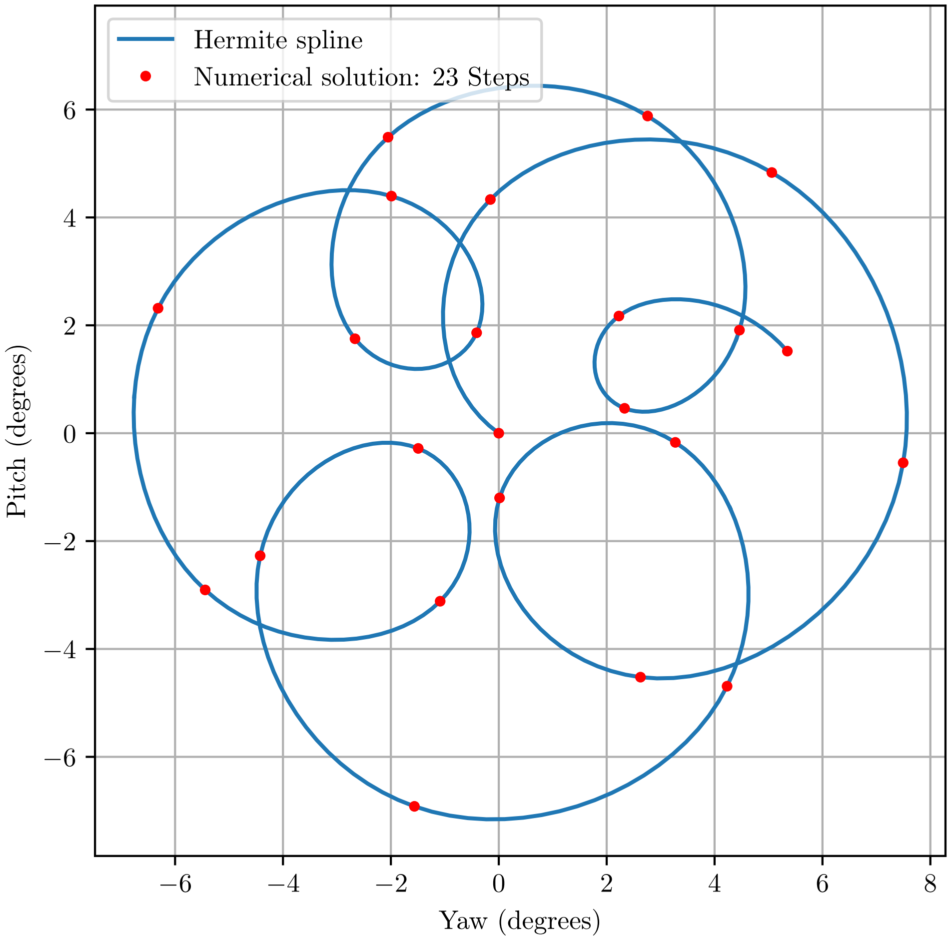

Figure 3.8: Pitch and yaw Hermite interpolation

3.6 Program sample calculation

The program is implemented as a python package (named BallisticsAJC) for versatility and ease of use. The algorithm performing the simulation (named Trajectory) is given a struct (Settings) detailing needed values and numerical routines. Trajectory is implemented with modularity in mind: most entries in struct represent files containing the necessary information. This allows alternative parameters, models, forces and moments to be seamlessly explored without performing major code revisions. Table 3.1 shows a sample "Settings" struct. The python script that initiates the simulation:

```
from BallisticsAJC import Trajectory

Trajectory(**Settings)
```

Table 3.1: Struct supplied to algorithm ("Settings")

Projectile model	`RB`
Atmosphere model	`ICAO`
Earth model	`Flat`
V_b (m/s), DC (deg), QE (deg)	`[200.   0.   45.]`
Adv initial conditions	`Twist_rate_18`
Geodetic location	`West`
Ambient conditions	`Mean`
Projectile	`M1`
Transformation method	`Quat`
Stepping algorithm	`BS`
First step size (sec)	`0.01`
Relative tolerance	`1e-12`
Absolute tolerance	`1e-10`
Target distance (m)	`1000`
Force & moment equations	`Classic`
Forces	`All`
Moments	`All`
Dense output	`False`
Save name	`testing`
Figures	`All`
Figure format	`pgf`

If the struct contains a “Savename”, the algorithm will write and save several text files documenting the settings, computation time, state vectors and state vector derivatives. This allows independent repeating of simulations or data processing. The simplified procedure performed by “Trajectory” is outlined in the block diagram, figure 3.9. For convenience BallisticsAJC is equipped with an “Illustrate” routine. It natively produces several common figures, such as height vs range, drift vs range, pitch vs yaw and angle of attack vs time, (if the model allows it). See appendix D for relevent information and sample outputs.

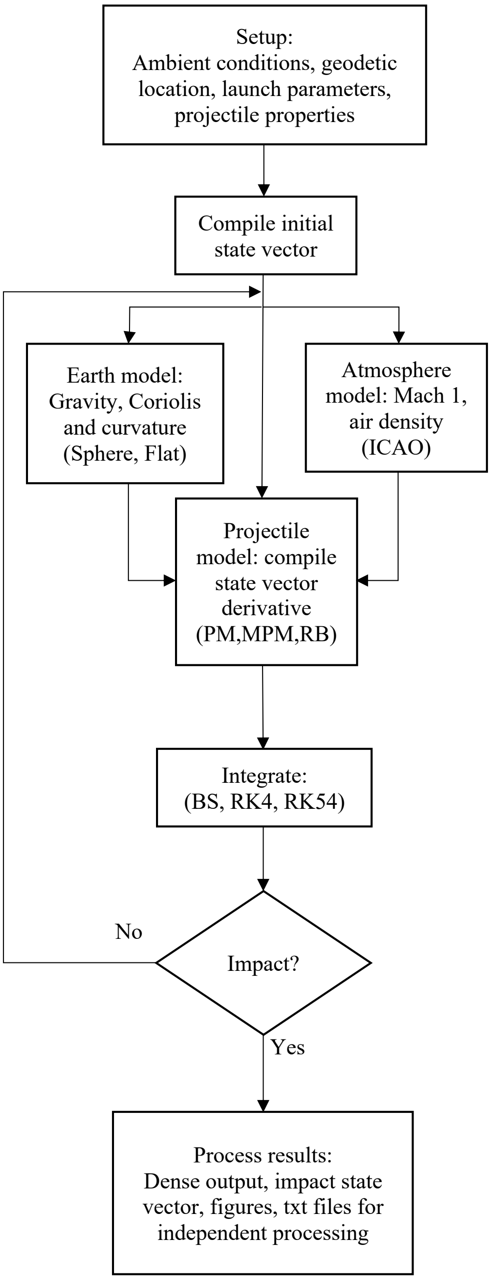

Figure 3.9: Trajectory algorithm: block diagram

Chapter 4

Evaluation

The ideal numerical model is computationally inexpensive and provides sufficiently accurate results from a minimal data set. The optimal solution for a situation is however not easily realised. Results can be compromised by: model, parameter and initial state errors (Fresconi *et al.*, 2011).

Model error

Model error is the compromise for simplifying or disregarding factors that define physical reality such as liquid payloads, asymmetries, forces or degrees of freedom.

Parameter error

The cumulative effects of erroneous values compromise the model output. Hence "high fidelity" models such as RB do not necessary entail superior precision or accuracy to MPM or PM.

Initial state error

Uncertainty in the initial state vector propagates throughout the solution: under or over estimation of muzzle velocity can cause the projectile to fall short or fly over the true impact point.

Due to the pervasive and stochastic nature of modelling error and uncertainty, numerical models can not be proven "true" . They can only be extensively corroborated. This can be facilitated by uncertainty analysis, sensitivity analysis, benchmarking and experimental results (Saltelli *et al.*, 2008).

4.1 Benchmarking

While the models presented are intended for tranquilliser darts, they are valid for any projectile. Benchmarking can thus be done against high ordinance artillery trajectories for which there are several documented simulations. The atmosphere and earth models used to incorporate the Coriolis effect, earth's curvature, variation in pressure and temperature are outlined in appendices A and B.

McCoy (1999) presents the analysis for the M1 artillery projectile and a standard mortar. Replicating these cases and comparing the results is an indication of the model's validity. Additionally to McCoy, a comparative study is done with commercial ballistics software PRODAS V3. This software has been validated with experimental results and used internationally. The aeroballistic properties of the projectiles are given in appendix C.

4.1.1 Mortar

A total of six trajectories are investigated to include a wide array of situations. The inputs and expected results as listed in McCoy (1999) are presented in table 4.1.

Figure 4.1: Mortar (120 mm)

Table 4.1: Mortar test cases

Run Number	V_m (m/s)	QE (deg)	ω_{y0} (rad/sec)	Range R (m)	Apogee H (m)
1	102	45	0.913	1010	260
2	102	65	0.913	770	420
3	102	85	0.913	165	510
4	318	45	1.795	7315	2100
5	318	65	1.795	5570	3380
6	318	85	1.795	1275	4070

Results

The models yield similar results: RB's errors are consistently less that 1% (see table 4.2). For a steep QE, PM and MPM have notable range errors. This can be attributed to pronounced pitching and yawing. Near the apogee the mortar's pitch reach values up to 40° (see figure 4.2). Only RB takes into account the corresponding increase in aerodynamic resistance.

$$\text{Relative error} = \delta_X = \frac{|X - X_{McCoy}|}{|X_{McCoy}|} \tag{4.1}$$

Table 4.2: Mortar trajectory relative error

Run	**RB**		**MPM**		**PM**	
Number	$\delta_R\%$	$\delta_H\%$	$\delta_R\%$	$\delta_H\%$	$\delta_R\%$	$\delta_H\%$
1	0.3	0.2	0.4	0.34	0.4	0.34
2	0.19	1.13	0.62	0.95	0.62	0.95
3	0.08	0.17	6.88	0.37	6.88	0.37
4	0.1	0.27	0.12	0.15	0.12	0.15
5	0.15	0.15	0.31	0.12	0.31	0.12
6	0.01	0.11	1.78	0.16	1.78	0.16

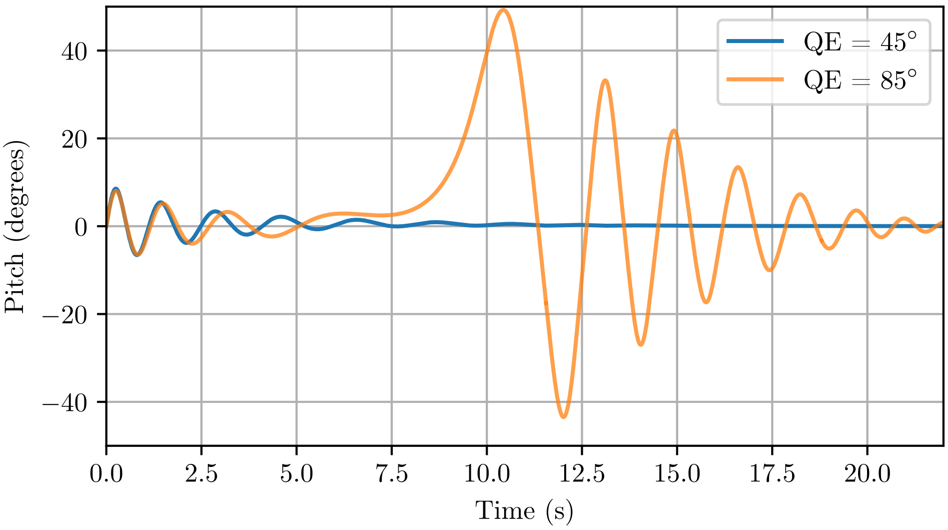

Figure 4.2: Mortar pitching ($V_m = 105$ m/s)

4.1.2 M1 artillery projectile

A total of 8 simulations are performed with the inputs and expected results as found in McCoy (1999) listed in table 4.3.

Figure 4.3: M1 artillery projectile

Table 4.3: M1 artillery projectile test cases

Run Number	Twist (Cal/turn)	V_m (m/s)	QE (deg)	ω_{y0} (rad/s)	Range R (m)	Apogee H (m)	Drift D (m)
1	18	205	45	1.44	3775	992	91
2	18	205	70	1.47	2360	1746	181
3	18	493	45	3.61	11494	3508	292
4	18	493	70	3.64	7408	6040	725
5	25	205	45	0.76	3770	992	66
6	25	205	70	0.79	2370	1746	137
7	25	493	45	1.97	11476	3508	213
8	25	493	70	1.98	7448	6040	522

Results

The RB model shows minor deviation with largest relative errors incurred from drift (close to 4%, see table 4.4). This is misleading as drift's order of magnitude is several times smaller than range and apogee. Similar to the mortar, MPM and PM have noteworthy range errors if QE is steep. The cause is slightly different from the mortar. Near the apogee the overturning moment and spin cause the yaw (specifically the yaw of repose) to engorge: reaching almost 25° (see figure 4.4).

Past the apogee an angle of attack around 7.5° is sustained for the remaining flight. This increases the overall complexity and magnitude of the aerodynamic forces and moments.

$$\text{Relative error} = \delta_X = \frac{|X - X_{McCoy}|}{|X_{McCoy}|} \tag{4.2}$$

.

Table 4.4: M1 artillery projectile relative error

Run Number	RB			MPM			PM		
	δ_R %	δ_H %	δ_D %	δ_R %	δ_H %	δ_D %	δ_R %	δ_H %	δ_D %
1	0.22	1.06	3.68	0.48	1.15	3.92	0.42	1.07	N/A
2	0.67	0.4	0.29	2.54	0.36	9.69	2.7	0.3	N/A
3	0.61	0.75	3.52	0.75	0.64	4.32	0.63	0.78	N/A
4	0.89	0.22	0.79	2.46	0.17	3.39	2.72	0.06	N/A
5	0.39	1.02	3.41	0.59	1.11	3.59	0.56	1.07	N/A
6	0.13	0.29	3.88	2.18	0.33	5.2	2.27	0.3	N/A
7	0.76	0.81	2.34	0.86	0.71	2.95	0.8	0.78	N/A
8	0.08	0.1	2.78	2.04	0.12	3.2	2.18	0.06	N/A

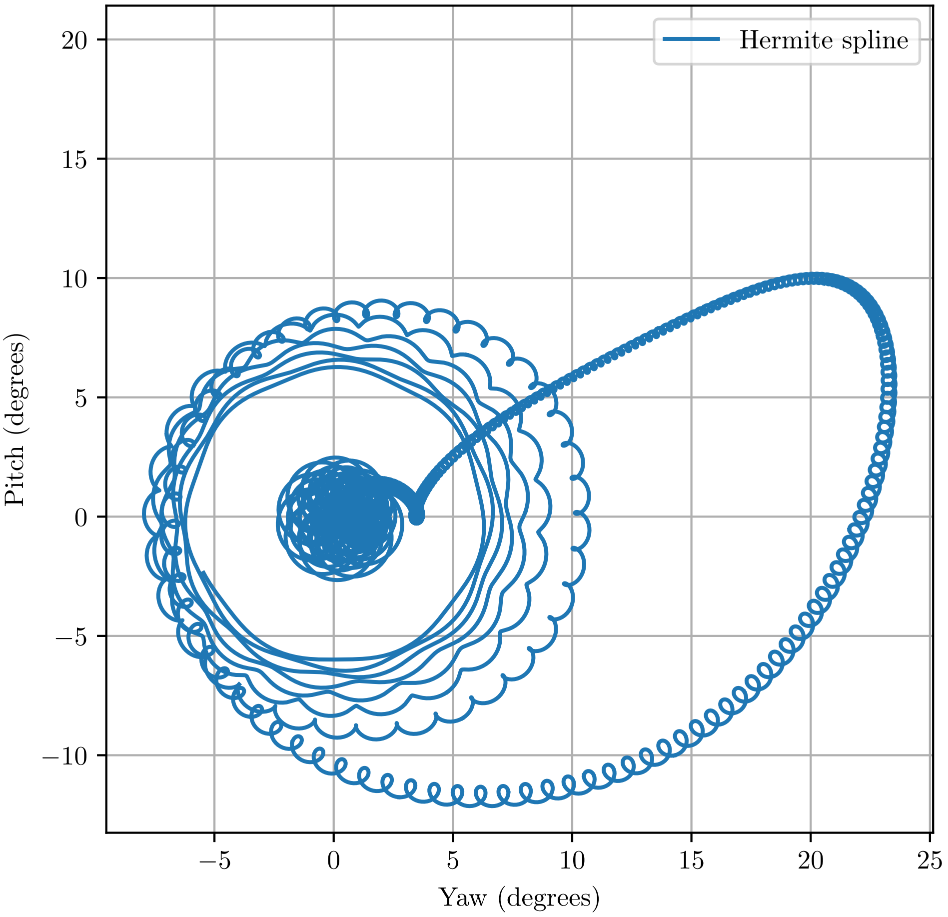

Figure 4.4: M1 projectile: Pitch and yaw (Subsonic, $QE = 70°$)

4.1.3 M107 artillery projectile

The inputs as found in Altufayl (2019) are listed in table 4.5 (constant twist rate, $T_w = 20$ cal/turn).

Figure 4.5: M107 artillery projectile

Table 4.5: M107 artillery projectile cases

Run Number	V_m (m/s)	QE (deg)	Range R (m)	Apogee H (m)	Drift D (m)	Vel V (m/s)
1	580	20	10837	1293	134.3	297.8
2	580	45	14851	4654	517.7	320.3
3	580	60	13056	6863	827.5	331.3
4	950	20	19099	2680	326.6	315.6
5	950	45	25642	9297	1186	335.9
6	950	60	24106	13914	1822	349.3

Results

MPM is qualitatively on par with RB: both yield highly accurate results with largest relative errors relating to drift, $\delta_D = 6.08\%$ (see tables 4.6-4.8). Similar to the M1 artillery projectile, this is misleading as the magnitude of range is several orders larger than drift.

Table 4.6: M107 artillery projectile RB relative errors

Run	**RB**			
Number	δ_R %	δ_H %	δ_D %	δ_V %
1	0.47	0.5	4.86	0.78
2	0.44	0.57	0.98	0.69
3	0.65	0.56	1.08	0.69
4	0.12	0.32	3.49	0.91
5	0.18	0.22	3.32	0.32
6	0.89	0.25	1.49	2.27

Table 4.7: M107 artillery projectile MPM relative error

Run		**MPM**		
Number	δ_R %	δ_H %	δ_D %	δ_V %
1	0.39	0.37	5.73	0.75
2	0.43	0.45	0.38	0.68
3	0.93	0.42	1.78	0.69
4	0.02	0.18	2.47	0.9
5	0.13	0.05	1.4	0.31
6	1.49	0.02	6.08	2.22

Table 4.8: M107 artillery projectile PM relative error

Run		**PM**		
Number	δ_R %	δ_H %	δ_D %	δ_V %
1	0.14	0.14	N/A	0.69
2	0.23	0.17	N/A	0.68
3	0.96	0.12	N/A	0.69
4	0.21	0.02	N/A	0.87
5	0.12	0.21	N/A	0.32
6	1.53	0.29	N/A	2.22

4.2 Uncertainty and sensitivity analysis

The previous sections confirmed that given correct inputs, the models yield accurate results. This does not imply they are “fit for purpose”. Input values are never truly correct: models must retain their validity even when presented with uncertainty (Saltelli *et al.*, 2008).

Uncertainty and sensitivity analysis are nearly always performed in tandem; latter quantifies all possible outputs based on global parameter variation; the former apportions the overall output variance to each input parameter. Both are paramount when developing models capable of surviving scientific inquiry as they answer the following questions:

- How robust is the model?
- What is the relative importance of each variable?

Comparing MPM and RB, several observations regarding sensitivity can be made before applying complex numerical analysis. In subsection 4.1.1 and 4.1.2 it is shown if a projectile maintains a small angle of attack, MPM yields results on par with RB. This implies the properties disregarded during MPM's derivation such as pitching and yawing are indeed minute. This is corroborated by the sensitivity analysis.

This also exemplifies an inherent danger of sensitivity analysis. The relevance of each input parameter depends on the situation considered. To give insight into the overall performance, various cases must be investigated: sensitivity analysis results will differ for each. For example the M1 artillery projectile is used for subsonic, supersonic, low and high ordinance trajectories. To illustrate the implications, 4 separate analyses are performed to encompass the wide array of flight behaviours. The defining characteristics of these cases are listed in table 4.9.

Table 4.9: M1 artillery projectile, sensitivity analysis cases

Run Number	Twist (Cal/turn)	V_m (m/s)	QE (deg)
1	18	205	45
2	18	205	70
3	18	493	45
4	18	493	70

4.2.1 Time dependent sensitivity analysis

Regardless of method, sensitivity/uncertainty analysis entails; generating a set of input parameters ($\mathbb{B}$); evaluating the model for each entry to define a corresponding set of scalar values ($\mathbb{A}$); estimating sensitivity (in this case μ^*) using both sets.

$$\mathbb{B} = \{\, \boldsymbol{b_0}, \boldsymbol{b_1}, \boldsymbol{b_2},\ \ldots\ , \boldsymbol{b_n} \,\} \tag{4.3}$$

$$a_n = f\big(\, \boldsymbol{b_n} \,\big) \tag{4.4}$$

$$\mathbb{A} = \{\, a_0, a_1, a_2,\ \ldots\ , a_n \,\} \tag{4.5}$$

$$\mu^* = f\big(\mathbb{A}, \mathbb{B}\big) \tag{4.6}$$

The sensitivity analysis performed differs from those encountered in literature as the sensitivity is monitored with time. A time dependent representation of sensitivity yields a robust guide for visualising the propagation of errors, prioritising parameters and model selection. To accomplish this task, the set of output parameters $\mathbb{A}$, must be expressible as a function of time.

Taking advantage of the dense output algorithm, a set of time dependent functions are generated ($\mathbb{F}$): each entry a unique projectile trajectory. Evaluating these functions, a complete set of projectile state vectors are known for any point in time.

$$\boldsymbol{Y}_n(t) = f\big(\boldsymbol{b_n}\big) \tag{4.7}$$

$$\mathbb{F} = \{\, \boldsymbol{Y}_0(t), \boldsymbol{Y}_1(t), \boldsymbol{Y}_2(t), \, \dots \, , \boldsymbol{Y}_n(t) \,\} \tag{4.8}$$

For the sensitivity measurement's magnitude to be comparable throughout, the property being investigated must be normalised at each instant considered. Normalisation by the norm of the mean vector worked sufficiently well. This is done separately for position, velocity and angular velocity.

$$\overline{\boldsymbol{e}_x}\Big|_i = \frac{\overline{\boldsymbol{x}}_i}{||\,\mathrm{mean}(\overline{\boldsymbol{x}})||} \tag{4.9}$$

$$\overline{\boldsymbol{e}_{\dot{x}}}\Big|_i = \frac{\dot{\overline{\boldsymbol{x}}}_i}{||\,\mathrm{mean}(\dot{\overline{\boldsymbol{x}}})||} \tag{4.10}$$

$$\overline{\boldsymbol{e}_\omega}\Big|_i = \frac{\overline{\boldsymbol{\omega}}_i}{||\,\mathrm{mean}(\overline{\boldsymbol{\omega}})||} \tag{4.11}$$

Atmosphere, Earth and Projectile models are all highly non-linear and cumulatively have upwards of 30 possible inputs ($\boldsymbol{b_n}$). The number of inputs and inherent computational cost of RB makes traditional sensitivity analyses such as Monte Carlo and One At a Time impractical as they require an exorbitant number of function evaluations. Based on the guidelines provided in Saltelli *et al.* (2008), Elementary Effects is appropriate.

Saltelli *et al.* (2008) outlines how to calculate $\mathbb{B}$ and the sensitivity measure mu^* from $\mathbb{A}$. While additional sensitivity measures can be quantified using Elementary effects, μ^* is usually sufficient indication of the overall sensitivity.

4.2.2 Results

For the subsonic and flat trajectory ($QE = 45°, V_m = 205\,\mathrm{m\,s^{-1}}$), position, velocity and angular velocity varied 3% from the mean (see figure 4.6). At supersonic velocities and/or high QE's the deviation reaches up to 10%. While not relevant for darts, it highlights the importance of investigating several operating conditions. The full results are in appendix E. If a similar analysis is performed on darts, intricate scenarios such as moving vehicles or helicopters should also be considered: ethical range will be significantly shorter.

$$\text{Relative average deviation (RAD)} = \max\left(\left|\frac{x_i - \text{mean}(x)}{\text{mean}(x)}\right|\right) \times 100$$

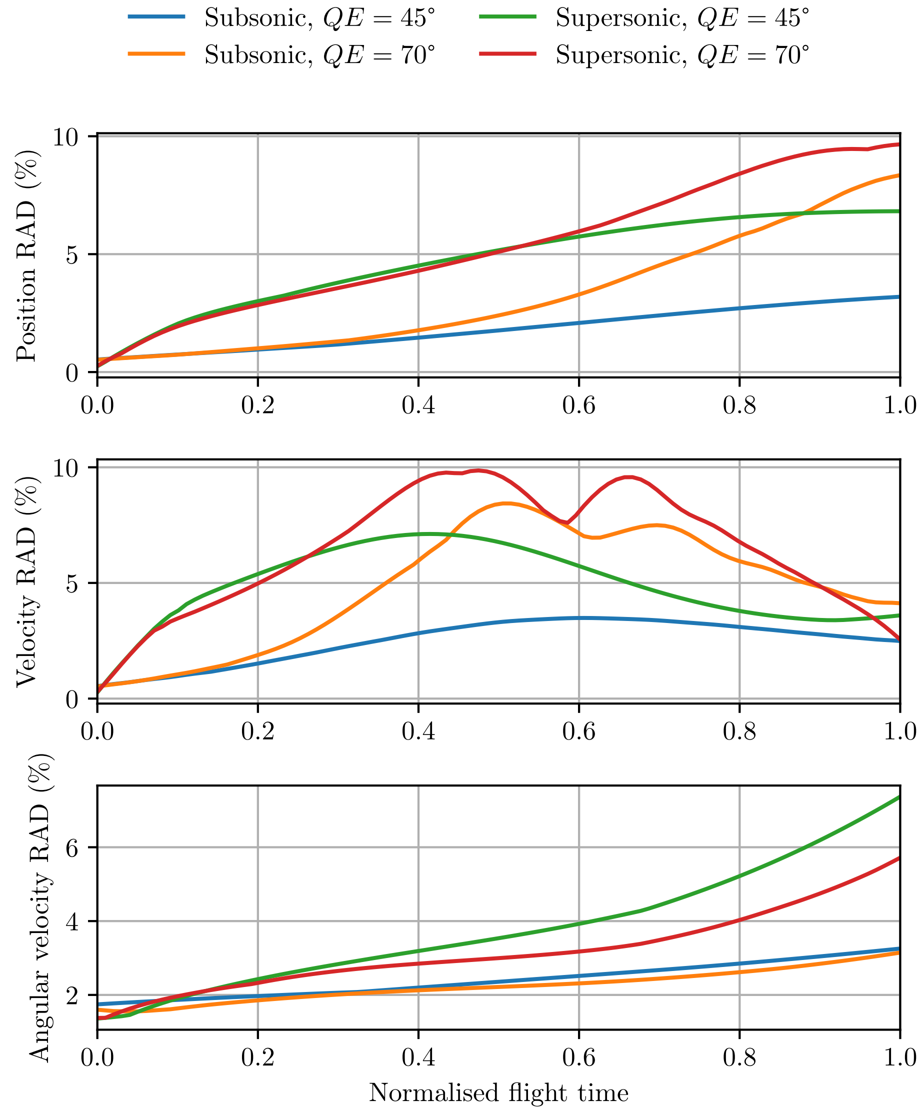

Figure 4.6: Relative average deviation

Sensitivity to launch parameters

The barrel orientation (QE and DC) and muzzle velocity (V_m) are the most influential parameters in all scenarios considered (see figure 4.7). This suggest optimising/accurately knowing the launch parameters might be more relevant than the projectile. This extends to tranquilliser darts, especially when used with compressed air rifles where muzzle velocity can be adjusted. It is worth noting the contribution of "lateral jump" : initial yawing and pitching (ω_y, ω_z) cause the projectile to deflect from the intended trajectory.

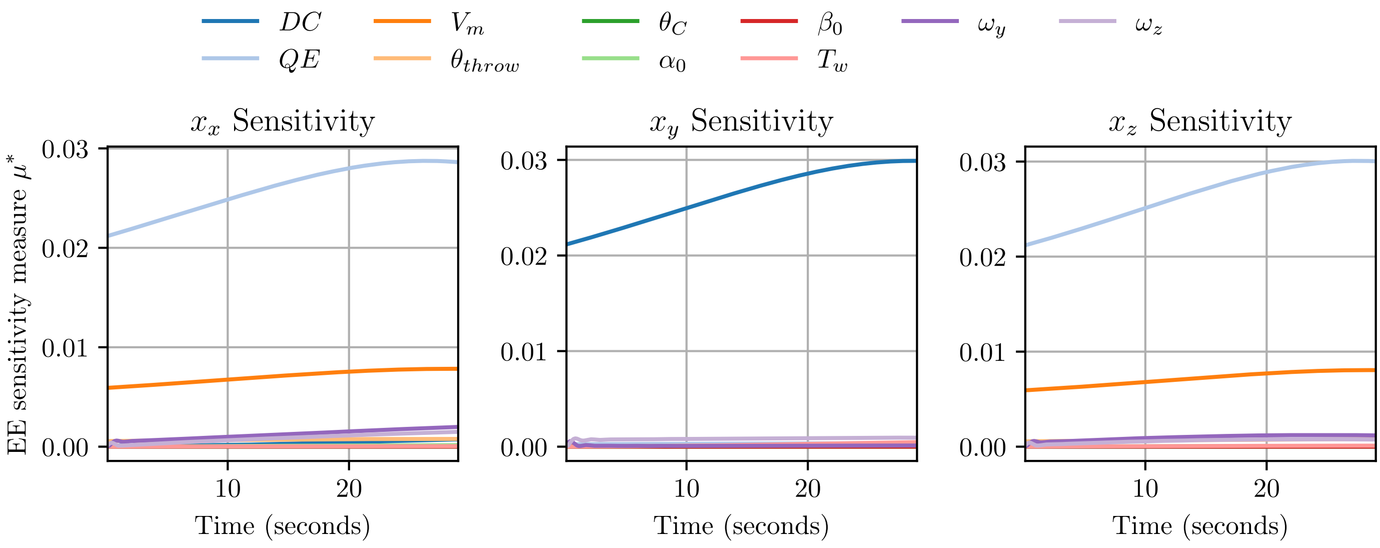

Figure 4.7: Position sensitivity to initial conditions (Subsonic, $QE = 45°$)

The sensitivity of the initial state, while always relevant, eventually stops increasing. In contrast sensitivity to parameters such as aerodynamic coefficients or ambient conditions keep on increasing throughout the timespan investigated (see figures 4.8 and 4.9). Given enough time and/or small enough uncertainty in the initial conditions, the parameter errors will eventually overtake the initial state errors: optimising the dart can become more crucial than the rifle.

Ambient conditions

Precisely measuring temperature and pressure is far less laborious than accurately defining the aerodynamic coefficients. Their sensitivity measures are however of similar magnitude (see figures 4.8 and 4.9). Eliminating uncertainty regarding T_0 and P_0 is thus an effective means of improving precision.

The contribution of wind (V_{WY},V_{WX}) must not be underestimated. It exacerbates lateral jump by increasing the initial angle of attack. In figure 4.8, there is an initial spike in cross-range wind's (V_{WY}) sensitivity as the projectile swerves trying to stabilise (lateral jump).

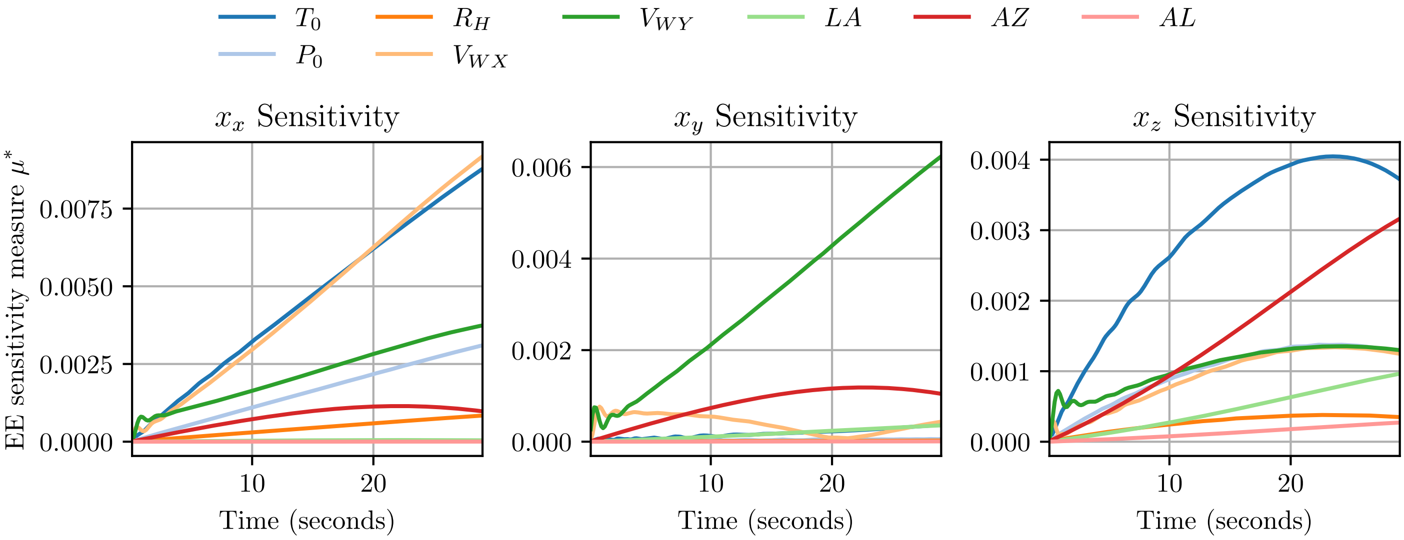

Figure 4.8: Position sensitivity to ambient conditions (Subsonic, $QE = 45°$)

At supersonic velocities all parameter sensitivities increase. See appendix E for the supersonic trajectory's results as they are not relatable to tranquilliser darts. Relative to temperature, the effect of wind is less pronounced because of the supersonic velocities encountered.

Predicting the onset of shock waves is crucial for supersonic trajectories. Consequently, even slight changes in air density and Mach number (temperature variation) have significant influences on the trajectory.

Aerodynamic coefficients

For a stable projectile with a consistently small angle of attack, the contribution of C_{D_0}, C_{L_0} and C_{M_α} eclipses all other coefficients. For such cases, like the trajectory presented in figure 4.9, (Subsonic, $QE = 45°$) MPM should yield accurate results.

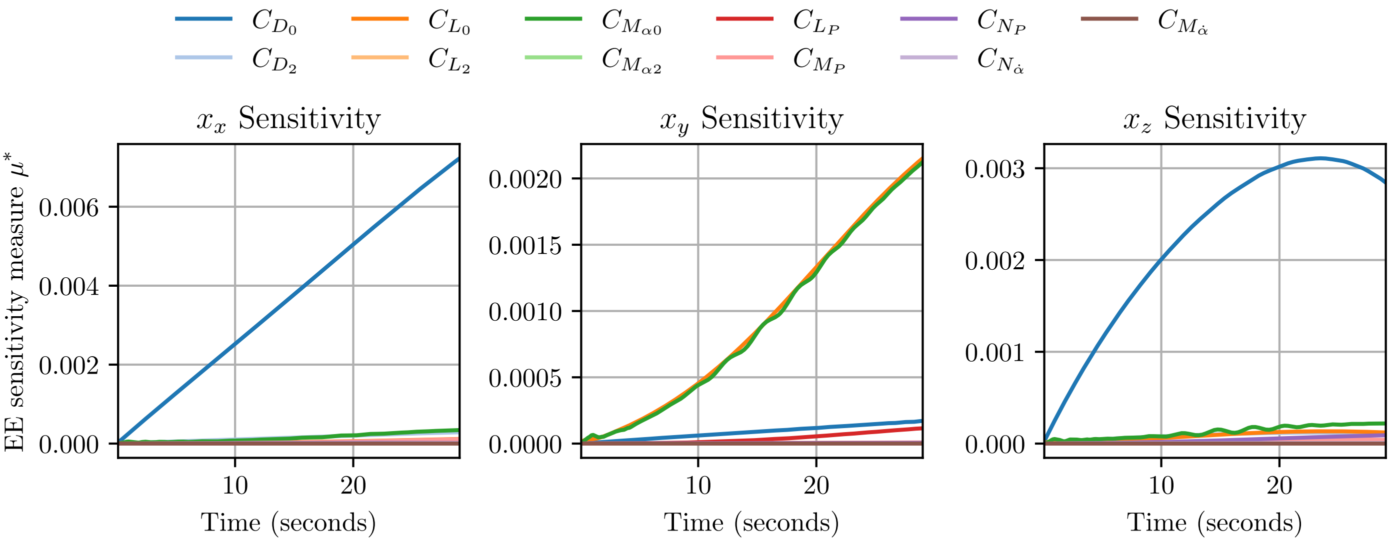

Figure 4.9: Position sensitivity to aerodynamic coefficients (Subsonic, $QE = 45°$)

As seen in figure 4.4, for the subsonic, super elevated ($QE = 70°$) trajectory, the yaw of repose reaches 23°. This large angle of attack increases the magnitude and overall complexity of the aerodynamic coefficients. The sensitivity analysis for that trajectory (figure 4.10) reflects this: several additional coefficients become relevant past the apogee. If impact were to occur exclusively before the apogee ($t < 20$ s), MPM would still be a viable approximation.

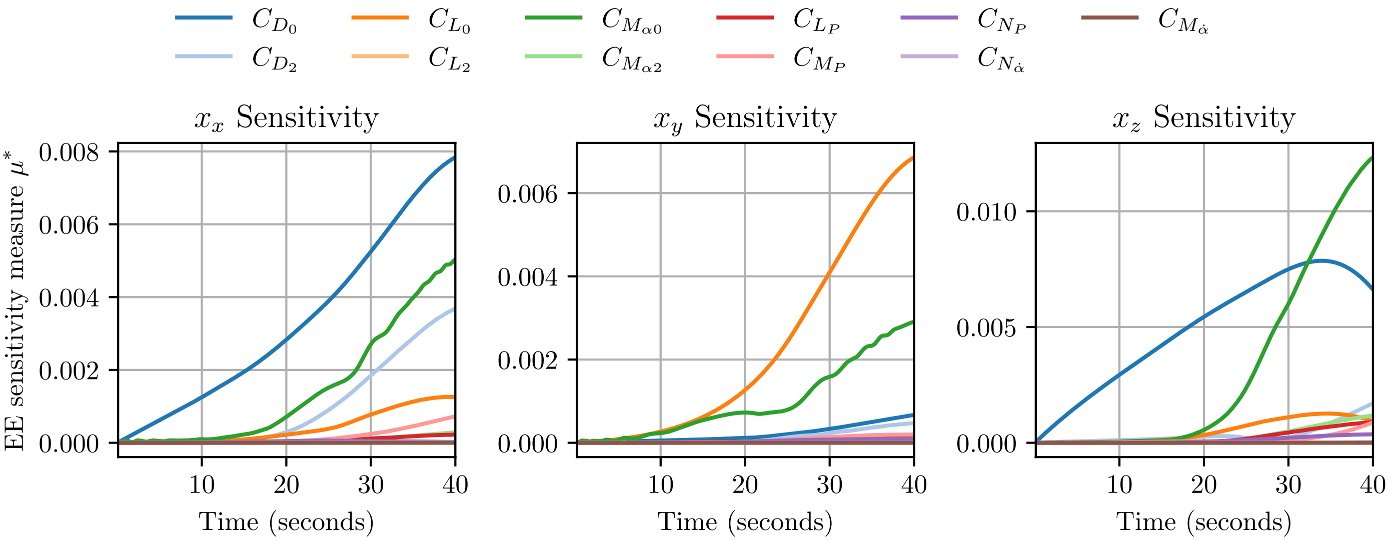

Figure 4.10: Position sensitivity to aerodynamic coefficients (Subsonic, $QE = 70°$)

Sensitivity analysis show that a stable and straight trajectory can be modelled using simple approximations such as PM or MPM. Since this will generally be the case for tranquilliser darts, RB approximations will likely not be qualitatively superior in most cases. In extreme conditions such as wind, moving vehicles or helicopters, a RB analysis is likely unavoidable. A large initial angle of attack, pitching and yawing will be present causing lateral jump and exacerbating aerodynamic resistance.

Chapter 5

Dart aerodynamic properties

To investigate tranquilliser dart aerodynamic behaviour, doppler radar tests and computational fluid analyses (CFA) are performed. Radar measurements provide a rudimentary guide and benchmark for the CFA. From both, an aeroballistic dart profile is assembled and applied to the projectile models to evaluate a hypothetical "design". The level of correspondence indicates how viable the models are for their intended purpose: modelling tranquilliser dart trajectories.

Only a smooth bore was available during testing and spin is thus not considered.

5.1 Doppler radar measurements

A doppler radar measures the dart's velocity along its trajectory. By monitoring the rate of decay, select aerodynamic traits can be inferred; complexity of drag coefficient (linearity); average drag coefficient. Five shots are recorded for the three darts shown in figure 5.1, namely 0.5 cc, 1 cc and 1.5 cc darts.

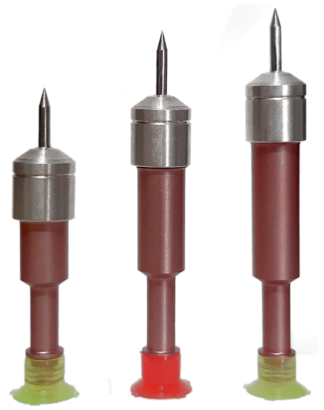

Figure 5.1: Professional wildlife equipment darts

Figures 5.2 - 5.4 shows that $(\dot{x})^{-1}$ varies linearly with time. The consistent gradients, suggest the intricacies (non-linearities) incurred from instability or flow regime are absent. Consequently, C_D can be assumed constant for each individual dart without significant error. Fitting the analytical solution (equation 1.20, restated for convenience) to the measurements, an average C_D is calculated.

$$\frac{1}{\dot{x}} = \left(C_D \frac{\rho A}{2m}\right) \times t + \frac{1}{\dot{x}_0}$$

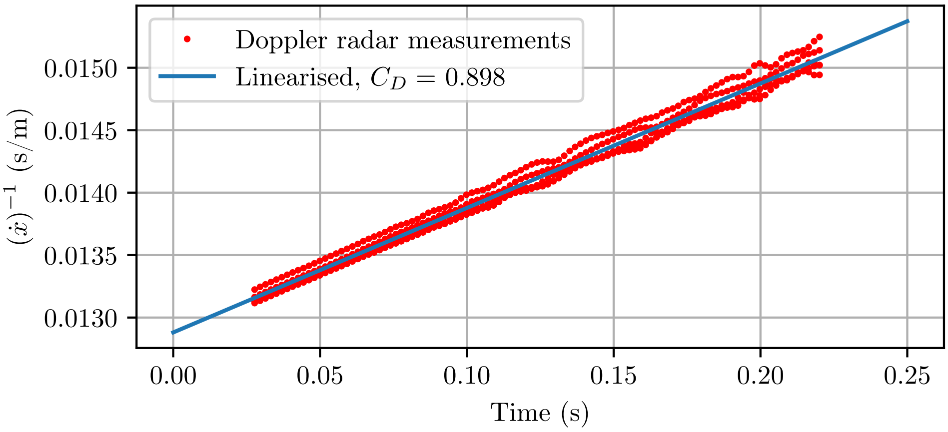

Figure 5.2: Curve fitted to doppler radar measurements: 0.5 cc dart

Due to the tailpieces, these darts all have high drag coefficients ($C_D > 0.9$). The additional surface area of the 1 cc and 1.5 cc darts increase their drag due to surface shear. The individual darts do not exhibit any unique behaviour, CFA is thus only performed on the 0.5 cc dart.

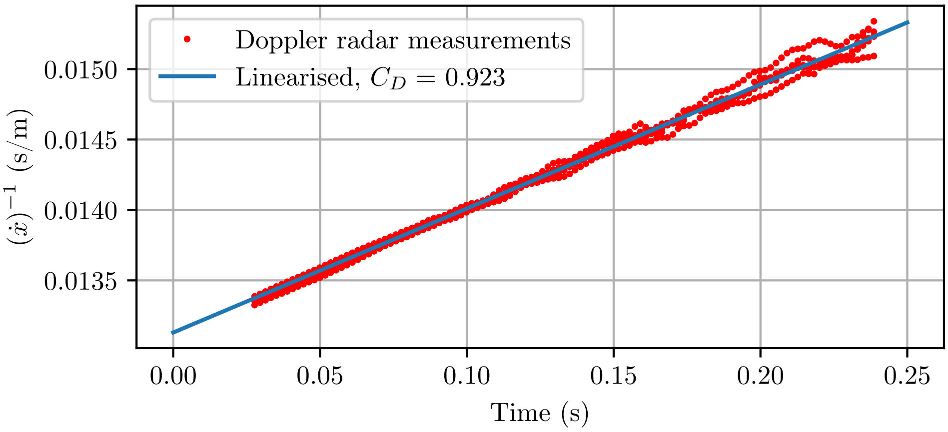

Figure 5.3: Curve fitted to doppler radar measurements: 1 cc dart

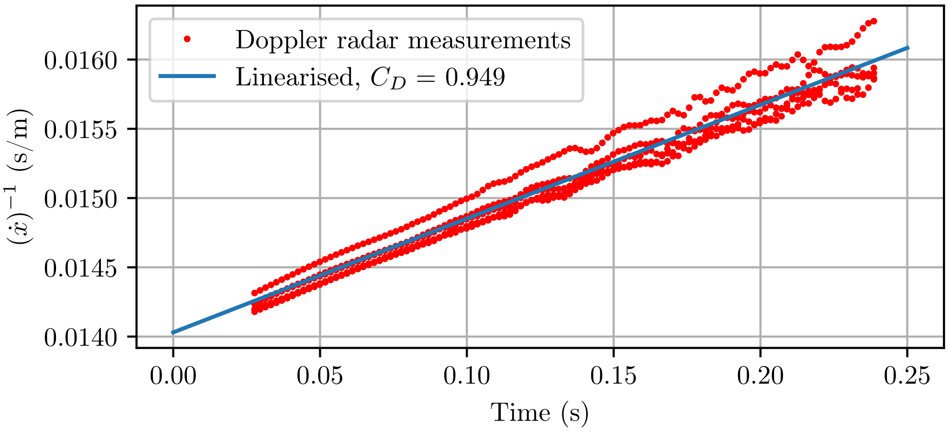

Figure 5.4: Curve fitted to doppler radar measurements: 1.5 cc dart

5.2 Computational fluid dynamics

The objective is to quantify the dart's aero-ballistic properties: diameter, mass, inertia and aerodynamic coefficients. The process entails recreating its geometry in Autodesk® Inventor (Release 2019) and performing CFD analyses using Ansys® Fluent (Release 19.2). Typically the aerodynamic forces and moments are quantified at multiple angles of attack and Mach number to account for their non-linear effects. The doppler radar's results suggest this is not necessary as the drag coefficient is almost constant.

This does not imply they are irrelevant, simply that they do not influence these specific trajectories (short, straight, windless and no spin): complexity is case dependent as illustrated by the sensitivity analysis in section 4.2. Various velocities and angles of attack should thus still be investigated despite not being applicable to the recorded trajectories. Two separate parameterised analyses are performed to determine the coefficient's sensitivity to angle of attack and Mach number. Since this requires several analyses, the parameterised simulations run autonomously: create the mesh and solve the flow without manual intervention.

5.2.1 Geometry refinement

The dart geometry is simple and can be easily captured, however the sharp needle tip causes extreme warpage of adjacent cells. This makes the simulation numerical unstable: residuals diverge. Robustness is improved by applying a small curvature ($radius = 0.2\,\text{mm}$). The resulting mesh at the needle tip is shown in figure 5.5.

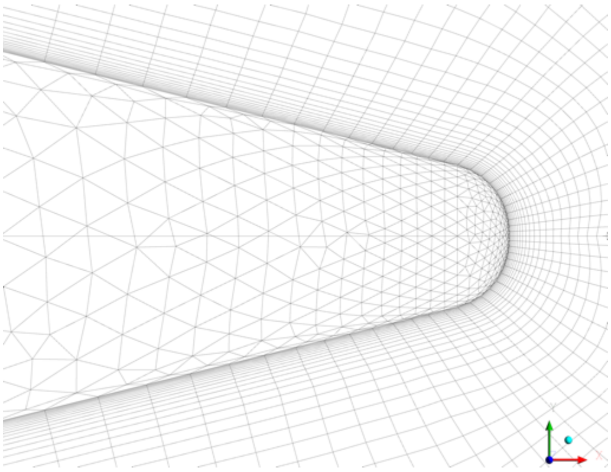

Figure 5.5: Needle mesh after geometry refinement

5.2.2 Flow domain

External ballistic simulations are free stream simulations. The flow field surrounding the dart must be large enough to represent this. For low Mach number ballistic problems like tranquilliser darts, velocity based inlet and pressure based outlet conditions are appropriate, (Ferziger and Perić, 2002). The dart is enveloped in a large cylinder with its volume representing ambient air at sea level. Since no spin is being considered, the needed flow domain is decreased by implementing a symmetry boundary condition.

Figure 5.6: Symmetry plane

Meshing

When investigating various angles of attack, the simulation must periodically re-mesh as the angle is incremented. To facilitate the needed autonomy, a predominantly unstructured topology is used (tetrahedral elements). To accurately capture the wake, a high mesh density region is created with more stringent size constraints (see figure 5.7).

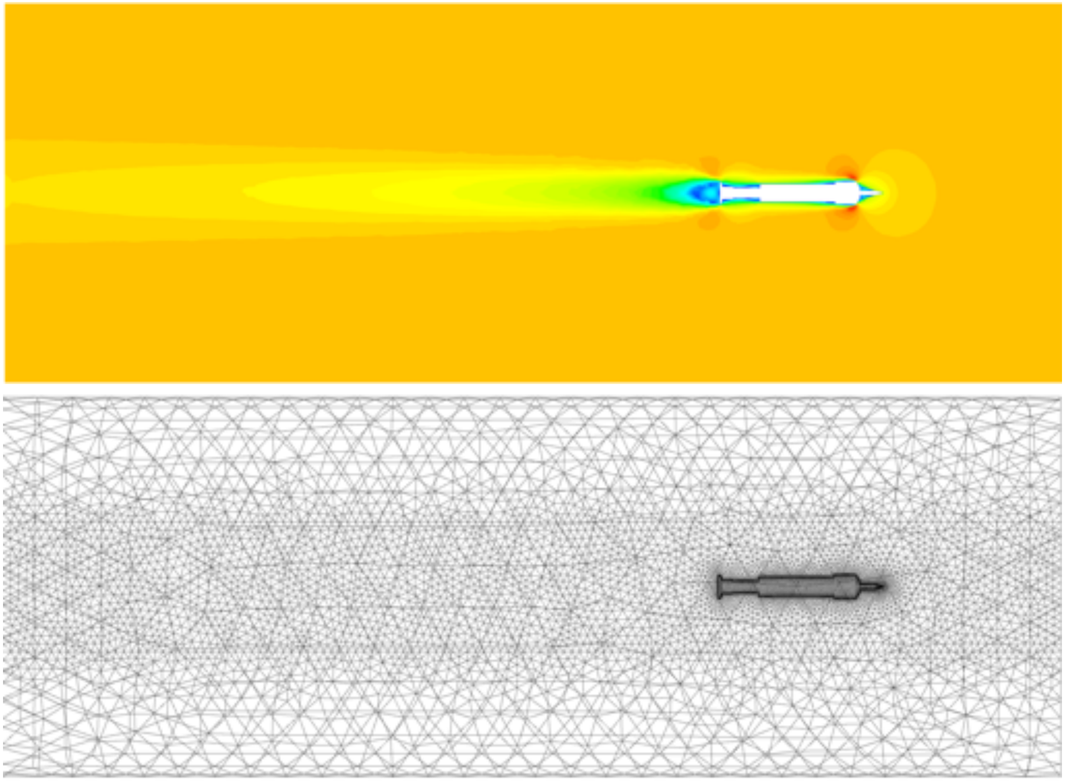

Figure 5.7: Mesh

There are two options to solve near-wall regions in Reynolds-averaged Navier-Stokes based simulations: fully resolve the viscous sublayer or use wall functions to approximate the flow quantities. Wall functions should only be used when near wall effects are not the primary concern as they have deficits in predicting flow separation. This makes them inappropriate for this simulation: near wall effects and flow separation are paramount in determining the aerodynamic coefficients (see figure 5.8). The recirculation at the dart face is clearly visible.

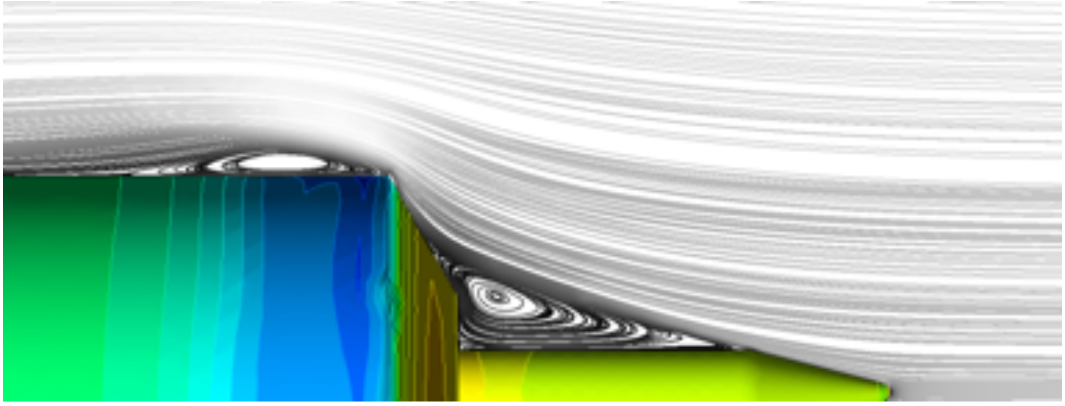

Figure 5.8: Dart pressure contours and fluid streamlines

To ensure the viscous sublayer is resolved the dimensionless wall distance ($y+$) must be sufficiently small during each analysis ($1 < y+$). Some of the key restrictions and modifications made to create the resulting grids (figure 5.7) are listed below:

- Maximum element size for dart surface is 0.4 mm
- A 20 layer inflation on dart surface (first layer 0.02 mm thick)
- Maximum element size in the high density mesh region is 4.5 mm
- Element growth rate in the high density mesh region is 1.1

5.2.3 Fluid properties

Darts operate exclusively at subsonic velocities (<0.3 Ma) where air can be assumed incompressible (Anderson, 2009). Mean sea level conditions are used.

5.2.4 Solvers

Two solver types are commonly integrated into computational fluid dynamics packages: a density-based and pressure-based solver. While density-based solvers are suited for any flow regime, they are inefficient at low Mach numbers ($Ma < 0.3$): flow is almost incompressible. Hence a pressure based solver is appropriate for dart simulations. Additional settings used for the solver:

- Gradient set to “Green-Gauss Node-Based”.
- Discretisation methods all set to “Second Order Upwind “ .
- Pressure-velocity coupling set to “Coupled“.

5.2.5 Turbulence model

Three viable turbulence models are considered, SST $k-\omega$, Transition $k-kl-\omega$ and Transition SST. As shown in table 5.1 both Transition SST and SST $k-\omega$ yield accurate results. SST $k-\omega$ is computationally less expensive and thus used during the parameterised simulations.
The simulated drag will be less than the measured values. Small instabilities/oscillations are always present and increase the average drag coefficient: a zero angle of attack is an unrealistic state.

Table 5.1: Drag coefficients ($\alpha_t = 0°$)

Solver	C_D
Doppler radar	0.898
SST $k-\omega$	0.858
Transition $k-kl-\omega$	1.043
Transition SST	0.863

Mesh independence

Given the prevalence of discretisation errors in CFA, mesh independence must be investigated (Fluent, 2013). Several simulations are performed with sequentially smaller elements in the high mesh density region. Since the doppler radar test had no spin, only drag, lift and overturning moment are investigated. While drag showed little variation with mesh density (varied 5%, see figure 5.9), lift and overturning moment are significantly more sensitive (varying up to 25%). To precisely model all 3 coefficients, a fine mesh is required ($> 10^6$ elements, maximum element size 4.5 mm). The study is performed at 70 m s^{-1} and 2.5° angle of attack.

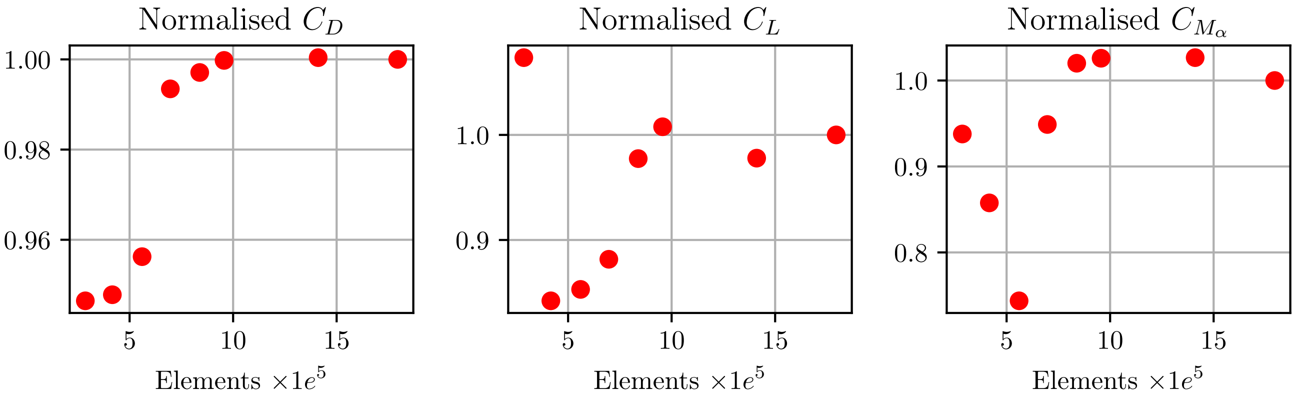

Figure 5.9: Mesh independence

5.3 Results

This dart's high stability and low operating velocities allow the coefficients to be approximated as constant. If excessive pitching or yawing is present the drag, lift and overturning moment coefficients will become highly non-linear.

Dependency on velocity

Tranquilliser darts operate exclusively at subsonic velocities ($40\,\mathrm{m\,s^{-1}} < \dot{x} < 100\,\mathrm{m\,s^{-1}}$). The coefficients are nearly independent of velocity in this range. They can be approximated as constant without significant error: a single analysis at an average velocity ($V = 70\,\mathrm{m\,s^{-1}}$) would suffice. Lift has the largest deviation from the average velocity (varies 5%, see figure 5.10), drag and overturning moment show very little variation ($< 1\%$). This corroborates the sensitivity analysis performed in section 4.2: non-linear effects from angle of attack (such as C_{D_2}, C_{L_2}) could be disregarded for flat trajectories. Therefore, the experimental cases investigated PM or MPM should yield sufficiently accurate results.

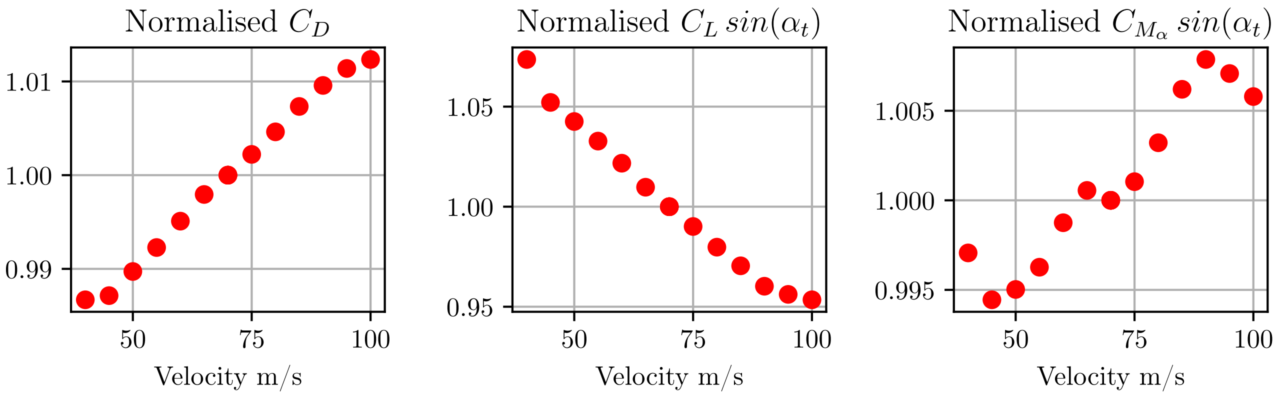

Figure 5.10: Variation with velocity

Dependency on angle of attack

Drag, lift and overturning moment are highly sensitive to angle of attack: after tilting 5°, drag increased 35% (see figure 5.11). The aerodynamic coefficients will be highly non-linear if pitching or yawing (instabilities) is present. The tailpiece however ensures the dart is stable, eliminating possible non-linearities due to the angle of attack (instabilities). If the darts are routinely used in windy conditions, moving vehicles or helicopters, high fidelity simulations are unavoidable: initial angle of attack, pitching/yawing and corresponding lateral jump will be engorged.

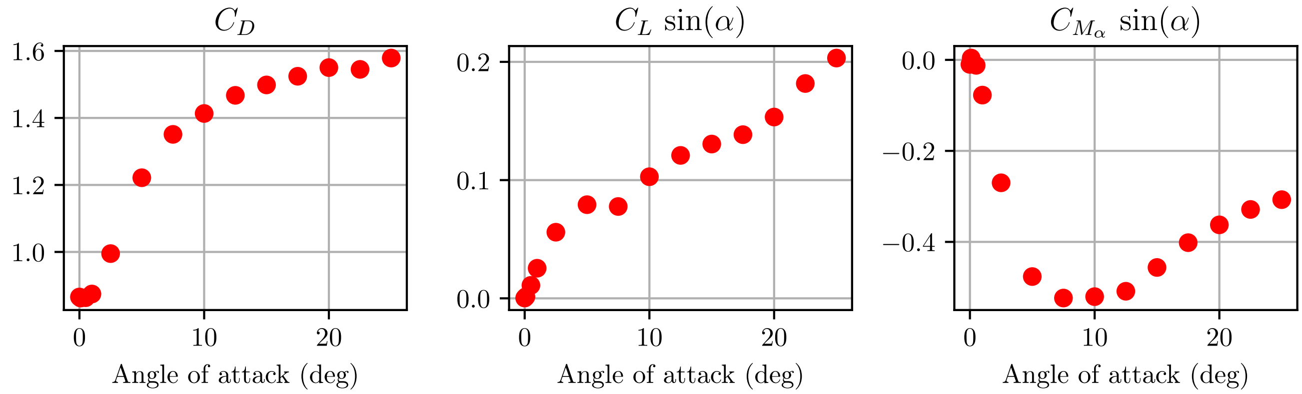

Figure 5.11: Variation with angle of attack

5.3.1 Models compared with measurements

For the trajectories measured, either MPM or PM model yield sufficiently adequate results: relative errors varying between 0.2% and 3%.

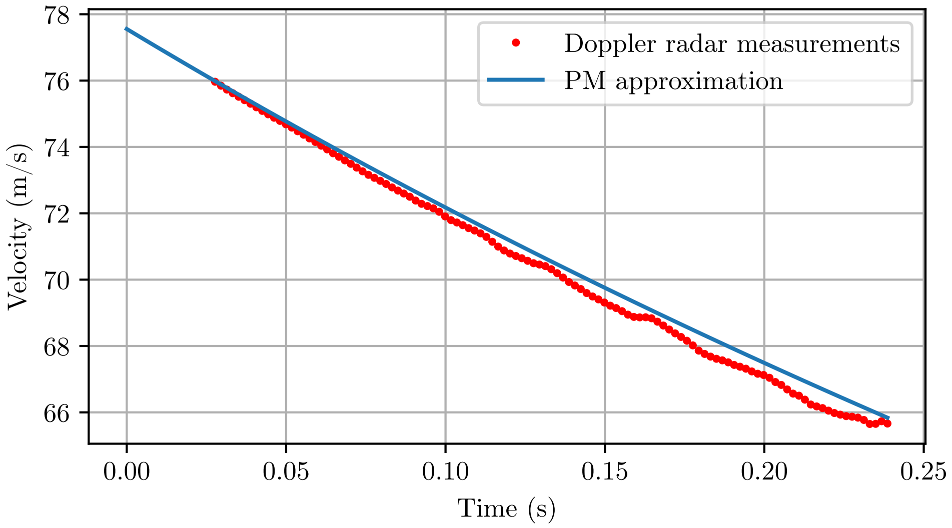

Figure 5.12: PM model predicted velocity and trajectory

Pitching and yawing are always present hence why PM slightly underestimates drag and the resulting velocity: assumes a zero angle of attack. RB can take the pitching and yawing motion into account. By introducing small angular velocity perturbations ($\omega_y = \ 1.5\,\mathrm{rad\cdot s^{-1}}$), the RB model yields highly accurate results (figure 5.13). The improved accuracy is offset by the labour required to sufficiently define a Rigid-body approximation.

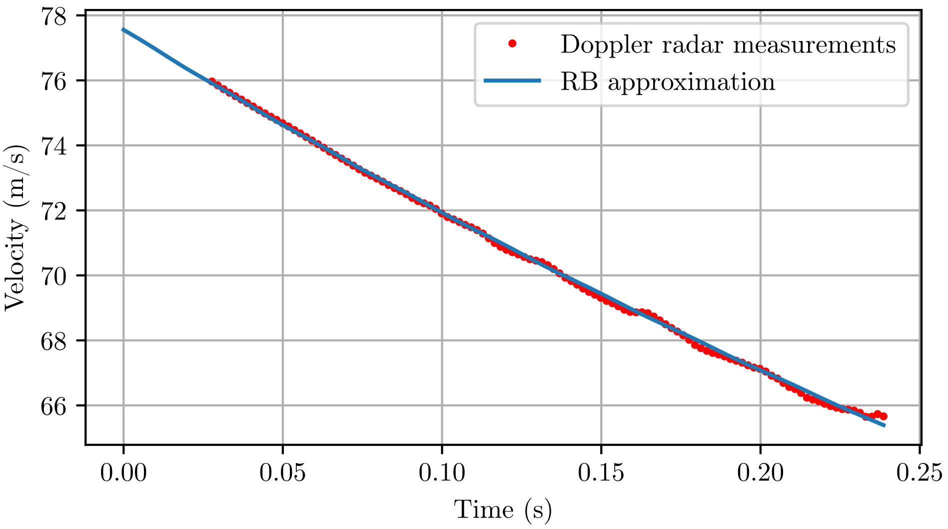

Figure 5.13: RB model predicted velocity and trajectory

These results do not imply that high fidelity models such as RB are irrelevant. They are simply not required to model these particular dart trajectories. As illustrated by the sensitivity analysis (4.2.1), deviation from intended impact point is case dependent. If a spin stabilised dart design were developed, its stability would need to be confirmed initially using RB.

Chapter 6

Conclusion

Several ballistic models are investigated, derived, implemented and verified to facilitate the design of tranquilliser darts. No model is innately superior, each having their respective advantages. Complex models such as Rigid-body can yield accurate results in a wide array of scenarios but are computationally expensive and laborious to define. In contrast, Point-mass and Modified point-mass are inexpensive and simple but only accurate when the projectile is stable with minute pitching/yawing.

Sensitivity analysis (Elementary effects) showed the required model fidelity and parameter accuracies are significantly less stringent for subsonic, flat trajectories. This agrees with doppler radar measurements suggesting drag stabilised darts have a near constant drag coefficient. This is further corroborated by CFA of a 0.5 cc dart. The drag, lift and overturning moment coefficients are nearly independent of velocity but sensitive to angle of attack. The tailpiece however ensures that there is little to no pitching and/or yawing, further eliminating non-linearities due to the angle of attack (instabilities). Consequently, a single CFA at an average velocity will yield a sufficient estimate of the aerodynamic forces and moments. For the same reasons, Point-mass and Modified point-mass will be qualitatively on par with Rigid-body. This does not imply that RB is irrelevant: if flight stability is not known, PM and MPM are not reliable (dart might tumble).

The drag coefficients measured and simulated are high ($C_D >= 0.9$), this can be accredited to drag stabilisation (tailpiece). The aerodynamic efficiency can be improved using spin stabilisation. Point-mass and Modified point-mass will however be unable to predict gyroscopic or dynamic instabilities. If a spin stabilised design is considered, it must (at least initially) be modelled using Rigid-body approximations to confirm stability.

Future studies

The models can be refined to take into account liquid payloads to analyse dart flight performance and stability in greater detail. It is shown that the models can predict dart trajectories. In conjunction with CFD, they can be used to devise a more efficient tranquilliser dart design. The success will reduce ballistic trauma and increase an operators ethical range.

Appendices

Appendix A

Atmospheric model

It is good practice to compare new numerical models with existing literature or commercial codes. For short and flat trajectories (like those encountered with darts), air density and speed of sound (ρ, a) can be assumed constant. Most analyses performed in literature are however for high ordinance artillery projectiles where this assumption is invalid: at 5000 m above sea level, air is 40% less dense (Cavcar, 2000). For benchmarking to be viable, the model must be able to take these changes into account.

Both ρ and a are indirectly only known at the launch site (through ambient pressure and temperature). The atmospheric model propagates these quantities to higher or lower altitudes. An internationally accepted model was introduced in 1952 by the International Civil Aviation Organisation (ICAO).

A.1 ICAO

The ICAO Standard Atmosphere model can approximate air pressure, temperature, density and speed of sound over a wide range of altitudes (< 80 km). Temperature and pressure behave differently in the troposphere and tropopause. At the boundary between the two layers:

$$T_{11} = 216.65°\text{K} \tag{A.1}$$

$$P_{11} = 22632 \text{ Pa} \tag{A.2}$$

Using these constants and the ambient conditions at the launch site, the temperature and pressure at the projectiles location is calculated.

Temperature

$$T = \begin{cases} T_0 - 6.5\dfrac{x_z}{1000} & (AL + x_z) < 11000 \text{ m} \\ \\ T_{11} & (AL + x_z) => 11000 \text{ m} \end{cases} \tag{A.3}$$

Pressure (dry air)

$$P = \begin{cases} P_0\left(1 - 0.0065\frac{x_z}{T_0}\right)^{5.2561} & (AL + x_z) < 11000 \text{ m} \\ \\ P_{11}exp\left(-\frac{g_0}{RT_{11}}\left(x_z + AL - 11000\right)\right) & (AL + x_z) => 11000 \text{ m} \end{cases} \tag{A.4}$$

From the pressure and temperature at the projectile's location, the corresponding air density and speed of sound is calculated.

Density: dry air

Using the ideal gas law:

$$R = 287.04 \text{ J/(kg·K)}$$

$$\rho = \frac{P}{RT} \tag{A.5}$$

Speed of sound: dry air

The speed of sound only varies with temperature.

$$\lambda = 1.4$$

$$a = \sqrt{\lambda \cdot R \cdot T} \tag{A.6}$$

A.1.1 Humidity correction factors

When accuracy requirements are extremely stringent, it is recommended to include the effects of humidity. Humid air is less dense and sound travels faster. While not explicitly significant, for projectiles that consistently travel at transonic speeds, slight changes in Mach number can become crucial. Murphy (1954) provides two correction factors for density and speed of sound. The are simply multiplied by the corresponding property for dry air ($\delta_a \cdot a$).

$$\delta_a\left(R_H\right) = 1 + 0.0014\left(R_H\right)\left(\frac{P_s}{101320.75}\right) \tag{A.7}$$

$$\delta_\rho\left(R_H\right) = 1 - 0.00378\left(R_H\right)\left(\frac{P_s}{101320.75}\right) \tag{A.8}$$

The saturated vapour pressure (P_s) can be accurately estimated using the Arden Buck equations presented in (Buck, 1981). They are a group of empirical correlations that relate saturation vapour pressure to temperature for moist air. They are valid between 193.15 and 323.15 K.

$$P_s(T) = \begin{cases} 611.21\exp\left(\left(18.678 - \dfrac{T-273.15}{234.5}\right)\left(\dfrac{T-273.15}{-16.01+T}\right)\right) & T > 0 \\ \\ 611.15\exp\left(\left(23.036 - \dfrac{T-273.15}{333.7}\right)\left(\dfrac{T-273.15}{6.67+T}\right)\right) & T < 0 \end{cases} \tag{A.9}$$

When no information is available regarding the launch site, it is common practice to use the average conditions at mean sea level (Cavcar, 2000).

Table A.1: International Mean Sea Level Conditions

Pressure	$P_{ave} = 101325$ Pa
Temperature	$T_{ave} = 288.15^\circ$ K (15° C)
Gravitational acceleration	$g_{ave} = 9.80665$ m/s^2
Density	$\rho_{ave} = 1.225$ kg/m^3
Speed of sound	$a_{ave} = 340.294$ m/s

Appendix B

Earth model

Similar to the atmospheric model, this is not necessary for tranquilliser darts, but is required to benchmark the ballistic model against commercial codes.

For most ballistic problems, the earth can be approximated as a stationary flat plane. For long distance trajectories (> 2000 m), variation in gravity, the earth's rotation and curvature become increasingly significant. The earth model quantifies these effect based on the geodetic location relative to the world frame. Figure B.1 shows the reference angles and values used to describe the geodetic location. The approaches used are well documented in Chaves *et al.* (2019) and McCoy (1999).

$$r = 6356766 \text{ m} \tag{B.1}$$

$$\Omega_E = 7.292115 \times 1e^{-5} \text{ rad/s} \tag{B.2}$$

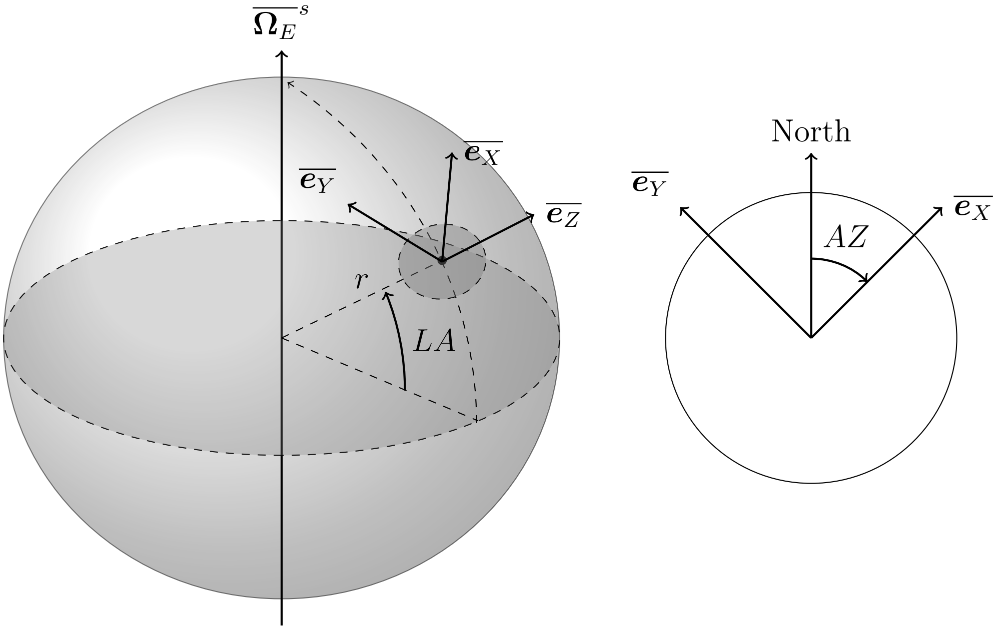

Figure B.1: Geodetic location

B.1 Gravity

Approximating the earth as flat plane assumes gravitational acceleration is independent of latitude and altitude. This is sufficient for applications such as tranquilliser darts where the relevant distances are simply too short. For this simple approximations the gravity vector can be defined as outlined in (Cavcar, 2000).

$$\overline{\boldsymbol{g}}^s = \begin{bmatrix} 0 & 0 & -9.80665 \end{bmatrix}^T \text{ m s}^{-2} \tag{B.3}$$

This is however inadequate for high ordinance trajectories. Equation B.4 takes into account gravity's variation with both latitude and altitude (Chaves *et al.* (2019), McCoy (1999)).

$$g = 9.80665[1 - 0.0026\cos(2LA)] \tag{B.4}$$

$$\overline{\boldsymbol{g}}^s = -g\begin{bmatrix} \frac{x_x}{r} & 0 & \left(1 - 2\frac{x_z + AL}{r}\right) \end{bmatrix}^T \tag{B.5}$$

B.2 Coriolis effect

The world frame is in motion due to the earth's rotation. This rotating frame causes a fictitious force that acts on the projectile known as the Coriolis effect.

$$\overline{\boldsymbol{\Omega}_E}^s = \begin{bmatrix} \Omega_E\cos(LA)\cos(AZ) & \Omega_E\cos(LA)\sin(AZ) & \Omega_E\sin(LA) \end{bmatrix}^T \tag{B.6}$$

$$\overline{\boldsymbol{\Lambda}}^s = -2\overline{\boldsymbol{\Omega}_E}^s \times \dot{\boldsymbol{x}}^s \tag{B.7}$$

B.3 Curvature correction

The earth's inherent curvature means a flat approximation will under estimate the horizontal displacement. These coordinates must thus be adjusted over greater distances. Equation B.8 gives the corrected coordinates for the projectile. It is however more convenient to use its derivative.

$$\overline{\boldsymbol{x}}^E = \begin{bmatrix} x_x & x_y & \left(x_z + \dfrac{x_x^2}{2r} \right) \end{bmatrix}^T \tag{B.8}$$

In the derivative (equation B.9), the effect is expressed as a vertical velocity. This can be seamlessly incorporated into any equation of motion.

$$\begin{aligned}
\dot{\overline{\boldsymbol{x}}}^E &= \begin{bmatrix} \dot{x}_x & \dot{x}_y & \left(\dot{x}_z + \dot{x}_x \dfrac{x_x}{r} \right) \end{bmatrix}^T \\
\dot{\overline{\boldsymbol{x}}}^E &= \dot{\overline{\boldsymbol{x}}}^s + \begin{bmatrix} 0 & 0 & \dot{x}_x \dfrac{x_x}{r} \end{bmatrix}^T \\
\dot{\overline{\boldsymbol{x}}}^E &= \dot{\overline{\boldsymbol{x}}}^s + \dot{\overline{\boldsymbol{x}}}_c^s
\end{aligned}$$

$$\dot{\overline{\boldsymbol{x}}}_c^s = \begin{bmatrix} 0 & 0 & \dot{x}_x \dfrac{x_x}{r} \end{bmatrix}^T \tag{B.9}$$

This increase in velocity only alters the resulting vertical displacement and is thus incorporated into the state vector derivative $\dot{\mathbf{Y}}$. Illustrating this with the Point-mass equations of motion:

$$\mathbf{Y}_{PM} = \begin{bmatrix} \overline{\boldsymbol{x}}^E \\ \dot{\overline{\boldsymbol{x}}}^s \end{bmatrix} \tag{B.10}$$

$$\dot{\mathbf{Y}}_{PM} = \begin{bmatrix} \dot{\overline{\boldsymbol{x}}}^E \\ \ddot{\overline{\boldsymbol{x}}}^s \end{bmatrix} = \begin{bmatrix} \dot{\overline{\boldsymbol{x}}}^s \\ m^{-1}\overline{\boldsymbol{F}}^s \end{bmatrix} + \begin{bmatrix} \dot{\overline{\boldsymbol{x}}}_c^s \\ \mathbf{0} \end{bmatrix} \tag{B.11}$$

Appendix C

Projectile properties

In chapter 4 the model is benchmarked against trajectories encountered in literature. This appendix gives the properties of the projectiles used: diameter, mass, inertia and aeroballistic coefficients. Linear interpolation is used to describe the coefficients as functions of Mach number and/or angle of attack.

C.1 M107 artillery projectile

Figure C.1: M107 artillery projectile

$$m = 43.0962 \text{ kg} \quad d = 155 \text{ mm} \quad I_x = 0.14248 \text{ kg m}^2 \quad I_t = 1.225615 \text{ kg m}^2$$

Table C.1: M107 artillery projectile aeroballistic coefficients

Mach	C_{D_0}	Mach	C_{D_2}	C_{L_P}	Mach	C_L	Mach
.4	.1419	1.78	1.890	-.71	3.336	-8.7	-.02800
.6	.1431	1.79	1.901	-.71	3.365	-8.5	-.02788
.7	.1439	1.96	1.909	-.72	3.388	-8.4	-.02776
.8	.1487	2.18	1.933	-.74	3.493	-8.4	-.02754
.9	.1756	2.57	2.033	-.79	3.737	-9.3	-.02712
1.0	.3239	3.27	2.328	-.83	3.618	-11.4	-.02643
1.2	.3816	4.69	2.476	-.65	3.403	-12.6	-.02511
1.5	.3416	3.72	2.621	-.56	3.268	-13.0	-.02370
2.0	.2976	2.74	2.812	-.51	3.058	-12.4	-.02213
2.5	.2607	2.18	2.865	-.50	2.928	-11.7	-.02028
3.0	.2329	1.73	2.821	-.50	2.874	-10.5	-.01905

C.2 Mortar

Figure C.2: Mortar

$m = 13.585$ kg $\quad d = 119.56$ mm $\quad I_x = 0.02335\ \mathrm{kg\,m^2} \quad I_t = 0.23187\ \mathrm{kg\,m^2}$

Table C.2: Mortar aeroballistic coefficients

Mach	C_{D_0}	Mach	C_{D_2}	Mach	C_{L_P}	Mach	C_L	Mach	$C_{M_{a0}}$
0	.119	0	2.32	0	1.75	0	14.8	0	-.02
.8	.119	.4	2.44	.6	1.95	.5	14.8	.4	-1.02
.85	.120	.6	2.66	.8	2.02	.6	4.5	.6	-1.62
.87	.122	.7	2.87	.9	2.06	.63	1.4	.8	-2.41
.90	.126	.75	3.01	.95	2.08	.7	0.4	.9	-2.72
.93	.148	.85	3.55			.8	8.8	.92	-2.75
.95	.182	.90	4.03			.9	28.3	.95	-2.71
		.95	5.20			.95	40		

Mach	$C_{M_{\alpha_2}}$	Mach	$(C_{M_{q+\alpha}})_0$	Mach	$(C_{M_{q+\alpha}})_2$
0	-15.1	0	-22	0	48
.45	-15.1	.8	-21.1	.5	-46
.6	-12.7	.85	-21.9	.6	-86
.7	-8.5	.9	-24,2	.7	-144
.75	-4.5	.92	-26.8	.8	-259
.8	1.5	.95	-31.5	.85	-357
.85	13.9			.9	-468
.90	30.2			.95	-745
.95	59.9				

C.3 Sierra international bullet

Figure C.3: Sierra international bullet

$$m = 10.8898\ \mathrm{g} \quad d = 7.82\ \mathrm{mm} \quad I_x = 7.2282e^{-8}\ \mathrm{kg\,m^2} \quad I_t = 5.3787^{-7}\ \mathrm{kg\,m^2}$$

Table C.3: Sierra international bullet aeroballistic coefficients

Mach	C_{D_0}	Mach	C_{D_2}	Mach	C_{L_P}	Mach	C_L	Mach	$C_{M_{a0}}$
0	.140	0	2.9	0	-.0150	0	1.75	0	3.05
.8	.140	.95	2.9	.5	-.0125	.5	1.63	.5	3.26
.85	.142	1.0	3.0	.8	-.0108	.8	1.45	.8	3.38
.90	.160	1.05	3.1	.85	-.0107	.85	1.40	.85	3.40
.95	.240	1.1	3.6	.90	-.0105	.90	1.35	.90	3.43
1.00	.430	1.2	6.5	.95	-.0103	.95	1.30	.95	3.45
1.05	.449	1.4	7.6	1.00	-.0100	1.0	1.35	1.0	3.24
1.1	.447	1.6	7.3	1.05	-.0099	1.05	1.55	1.05	3.17
1.2	.434	1.8	6.8	1.1	-.0098	1.1	1.70	1.1	3.15
1.4	.410	2.0	6.1	1.2	-.0095	1.2	1.90	1.2	3.12
1.6	.385	2.2	5.4	1.4	-.0088	1.4	2.15	1.4	3.06
1.8	.365	2.5	4.4	1.6	-.0083	1.6	2.32	1.6	2.98
2.0	.350			1.8	-.0080	1.8	2.45	1.8	2.88
2.2	.339			2.0	-.0075	2.0	2.58	2.0	2.79
2.5	.320			2.2	-.0073	2.2	2.68	2.2	2.69
				2.5	-.0068	2.5	2.85	2.5	2.56

Mach	$C_{M_{\alpha_2}}$	Mach	C_{M_q}	Mach No.	α_t^2	C_{M_P}
0	-4.3	0	1.2	0	0	-2.6
.95	-4.3	1.05	1.2	0	29.2	.06
1.0	-4.35	1.1	0.5	0	400	.06
1.05	-4.4	1.2	-3.6	.90	0	-2.6
2.5	-4.4	1.4	-7.3	1.1	0	-1.35
		1.6	-8.2	1.1	18.4	.05
		2.5	-8.2	1.1	400	.05
				1.4	0	-.51
				1.4	9.9	.24
				1.4	400	.24
				1.7	0	-33
				1.7	5.6	.10
				1.7	400	.10
				2.5	0	-.33
				2.5	400	.10

C.4 M1 artillery projectile

Figure C.4: M1 artillery projectile

$$m = 14.97 \text{ kg} \quad d = 104.8 \text{ mm} \quad I_x = 0.02326 \text{ kg m}^2 \quad I_t = 0.23118 \text{ kg m}^2$$

Table C.4: M1 artillery projectile aeroballistic coefficients

Mach	C_{D_0}	Mach	C_{D_2}	Mach	C_{L_P}	Mach	C_{L_0}	Mach	C_{L_2}
0	.124	0	3.2	0	-0178	0	1.63	0	0.1
.875	.124	.88	3.2	.43	-0149	.4	1.63	.2	0.16
.925	.150	.97	6.3	.70	-0135	.7	1.41	.6	3.5
.965	.200	.99	4.0	.91	-0126	.89	1.22	.8	6.6
990	.350	1.15	5.0	1.4	-0110	.99	1.73	.985	9.2
1.025	.375	1.25	5.4	1.75	-.0101	1.09	1.57	1.09	8.8
1.085	.415	1.3	5.5	2.1	-.0094	1.5	1.97	1.3	12.0
1.19	.415	2.5	5.5	2.5	-.0087	2.0	2.25	1.5	13.7
1.35	.385					2.5	2.50	2.0	16.0
1.80	.335								
2.0	.318								
2.5	.276								

Mach	$C_{M_{\alpha_0}}$
0	3.55
.46	3.55
.61	3.76
.78	3.92
.87	3.96
.925	4.85
.97	4.0
1.09	3.83
1.5	3.75
2.5	3.75

Mach	$C_{M_{\alpha_2}}$
0	-2.9
.4	-2.9
.45	-3.1
.65	-4.4
.78	-3.45
.885	-1.78
.98	-3.0
1.075	-2.1
1.25	-3.325
1.5	-4.45
2.0	-4.6
2.5	-4.6

Mach	$C_{M_{q+\alpha}}$
0	-3.15
.79	-3.15
1.15	-9.1
1.55	-9.5

Mach	α_t^2	C_{N_P}
0	0	-.34
0	632	-.91
0	908	-1.42
0	1316	-2.63
.22	0	-.34
.22	632	-.91
.22	908	-1.42
.22	1316	-2.63
.31	0	-.125
.31	21.4	-.465
.31	364.5	-.503
.31	638	-1.015
.31	1316	-2.92
.48	0	-.34
.48	348.5	-.591
.48	1316	-2.45
.99	0	-.34
.99	348.5	-.591
.99	1316	-2.45
1.001	0	-.36
1.001	706	-1.68
1.55	0	-.36
1.55	706	-1.68

Mach	α_t^2	C_{M_P}
0	0	.10
0	403.6	.173
0	630	.345
0	1316	2.35
.22	0	.10
.22	403.6	.173
.22	630	.345
.22	1316	2.35
.31	0	.10
.31	410.8	.133
.31	637.7	.471
.31	915.9	1.276
.31	1316	2.35
.48	0	-.46
.48	27.5	.08
.48	375.2	.022
.48	1316	.94
.81	0	-.46
.81	27.5	.08
.81	375.2	.022
.81	1316	.94
.87	0	.4175
.87	315.3	.053
.87	743.9	.285
.92	0	.4175
.92	315.3	.053
.92	743.9	.285
.96	0	.3747
.96	322.2	.05
.96	1316	.665
.995	0	.3747
.995	322.2	.05
.995	1316	.665
1.02	0	.20
1.02	322.2	.301
1.1	1316	.20
1.1	0	.301
1.21	375.7	.193
1.21	0	.50
1.21	375.7	.301
1.28	0	.193
1.28	403.6	.50
1.28	705.7	.445
1.46	0	.215
1.46	410.8	.495
1.55	0	.215
1.55	410.8	.495

Appendix D

Algorithm sample outputs

BallisticsAJC is equipped with an "Illustrate" routine. It natively produces several common figures, such as height vs range, drift vs range, pitch vs yaw and angle of attack vs time, (if the model allows it). It can be either executed within "Trajectory" as outlined in section 3.6 or at a later stage by providing "Illustrate"with the same struct used to save a prior simulation. In this case it simply processes the already existing data. This appendix gives the figures resulting from the sample struct provided in (table 3.1). The corresponding python script to process existing data:

```
from Ballistics_AJC import Illustrate

Illustrate(**Settings)
```

The code produces these figures:

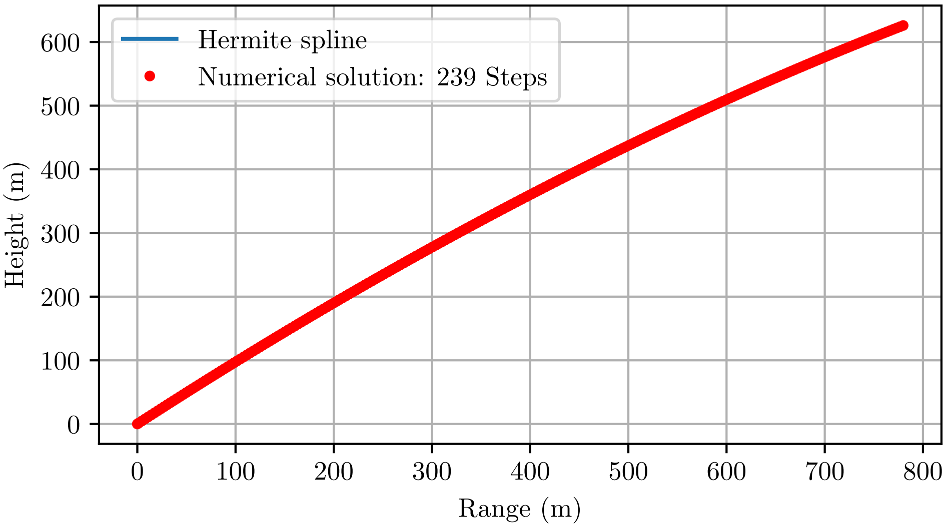

Figure D.1: Sample output: Height vs range

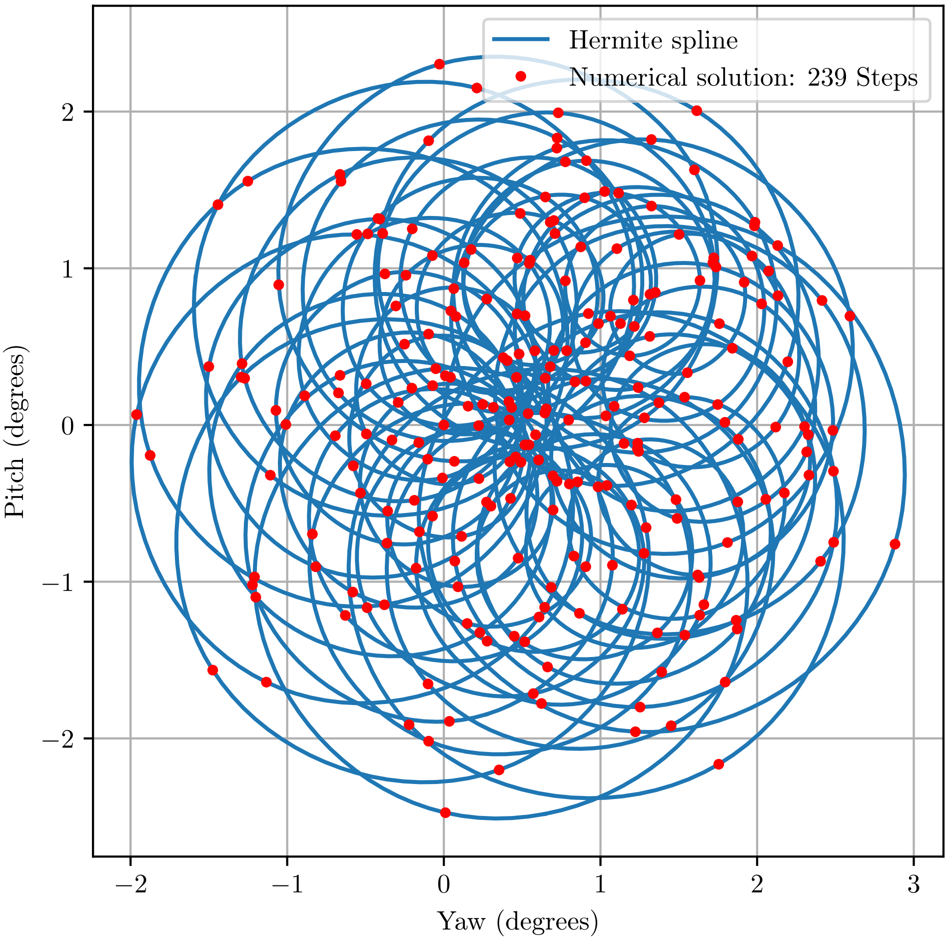

Figure D.2: Sample output: Pitch vs Yaw

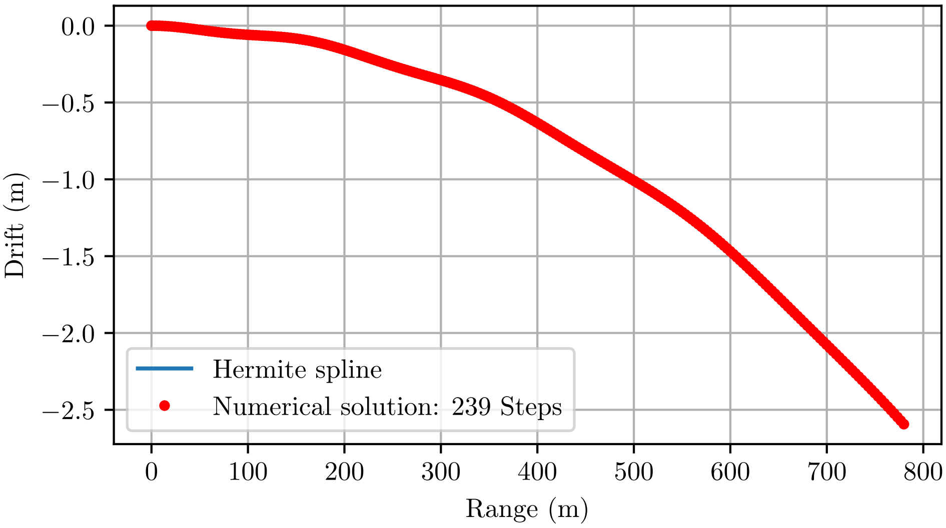

Figure D.3: Sample output: Drift vs range

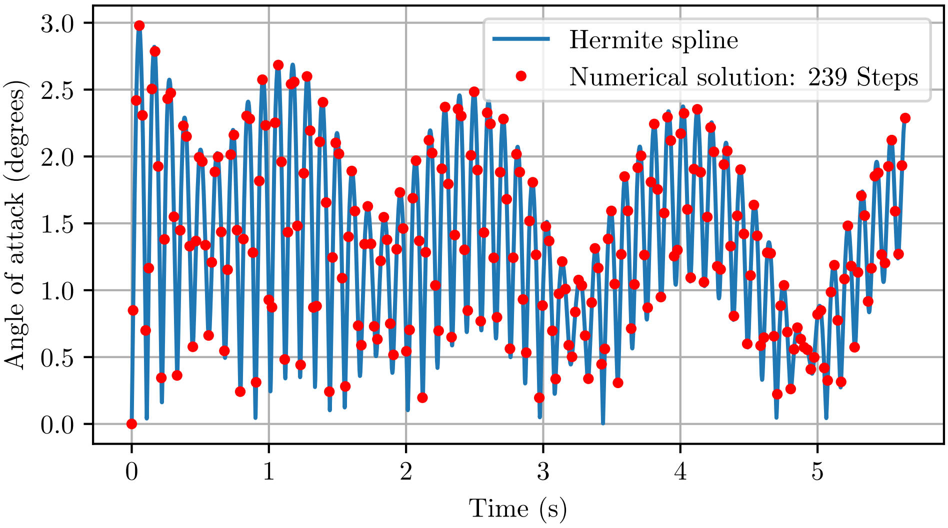

Figure D.4: Sample output: Angle of attack vs time

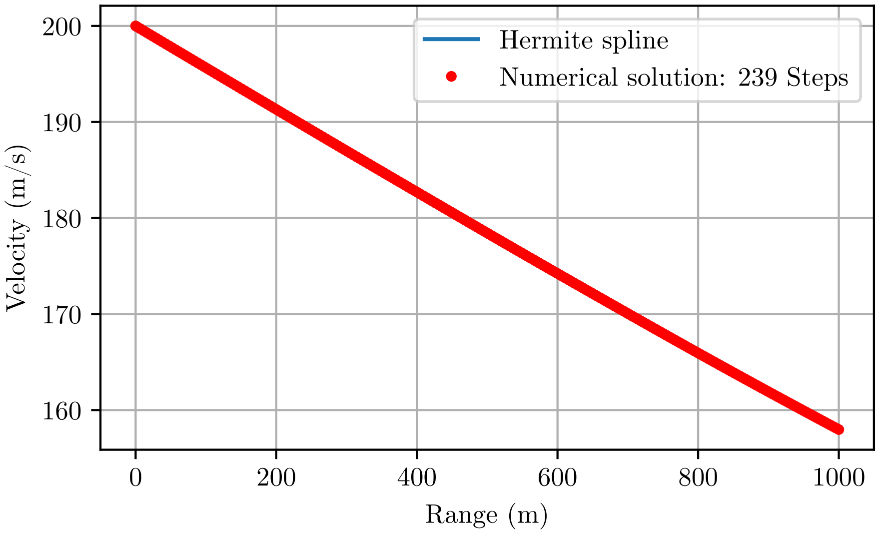

Figure D.5: Sample output: Velocity vs time

Appendix E

Sensitivity/uncertainty analysis results

Sensitivity analysis (Elementary effects) is performed on a M1 artillery simulation (Rigid-body). Unlike traditional analyses that simply investigate a predetermined point of impact, the entire trajectory is analysed. A time dependent presentation of sensitivity yields a robust guide for understanding the propagation of errors, prioritisation of parameters and model selection.

Four unique trajectories are analysed with distinct defining characteristics: supersonic, subsonic and high or low ordinance (outlined in table E.1). This appendix gives the results of the sensitivity analysis for all the parameters investigated: location, velocity and angular velocity.

Table E.1: M1 artillery projectile cases

Run Number	Twist (Cal/turn)	V_m (m/s)	QE (deg)
1	18	205	45
2	18	205	70
3	18	493	45
4	18	493	70

E.1 Subsonic, QE = 45 study

E.1.1 Position sensitivity

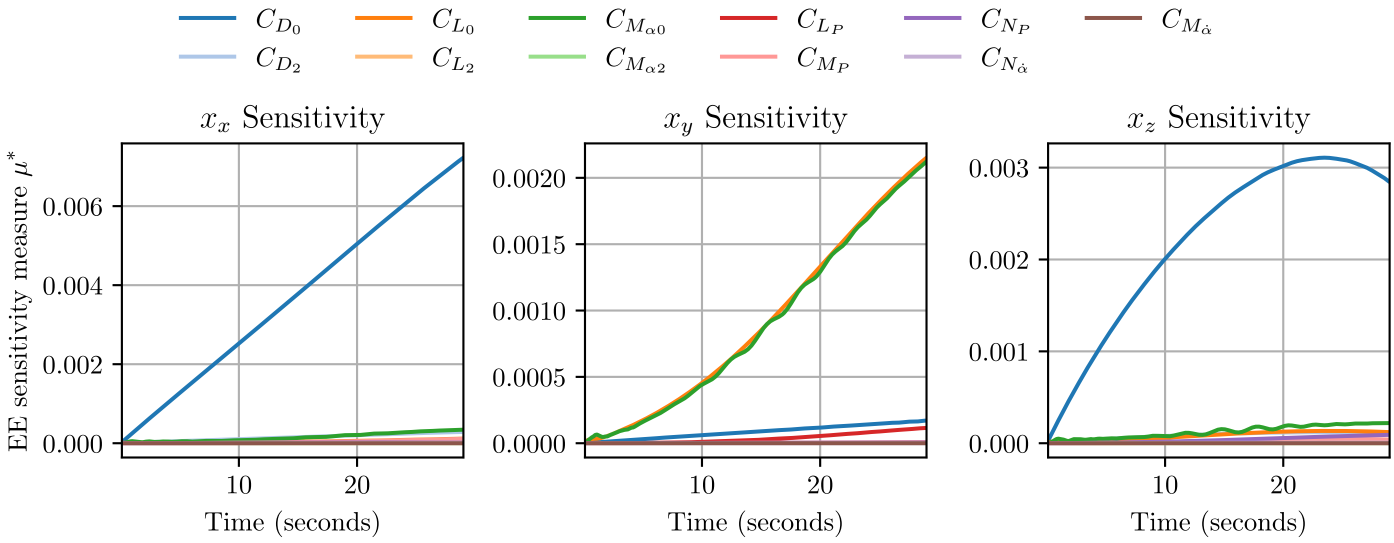

Figure E.1: Sensitivity to aerodynamic coefficients

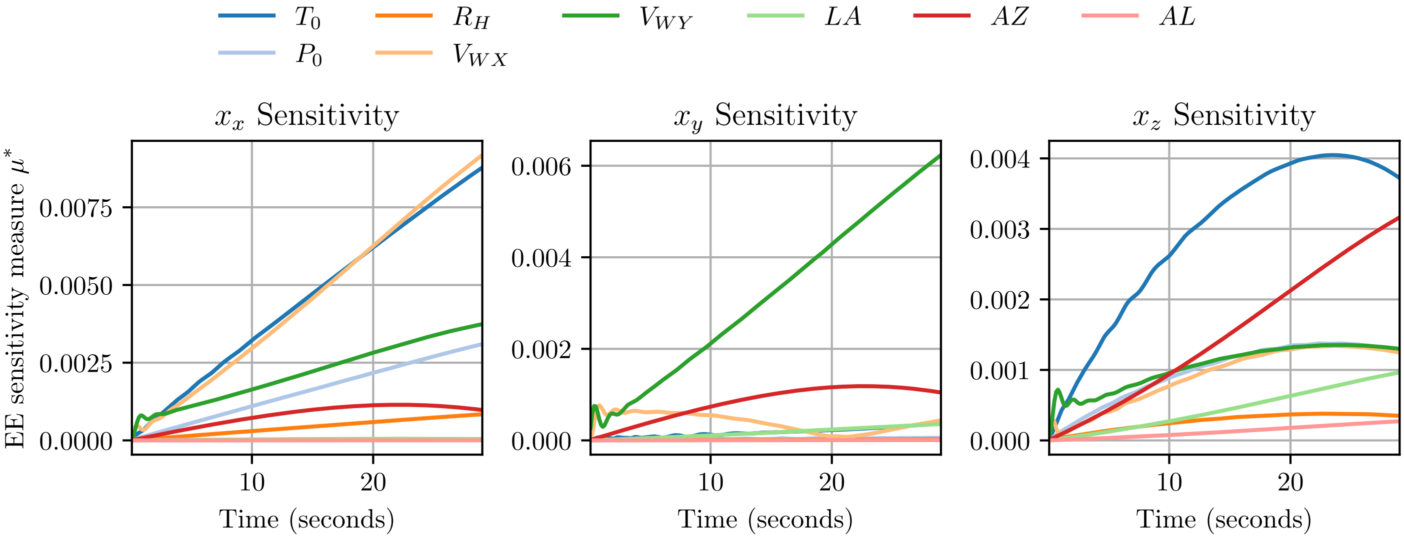

Figure E.2: Sensitivity to location and ambient conditions

.

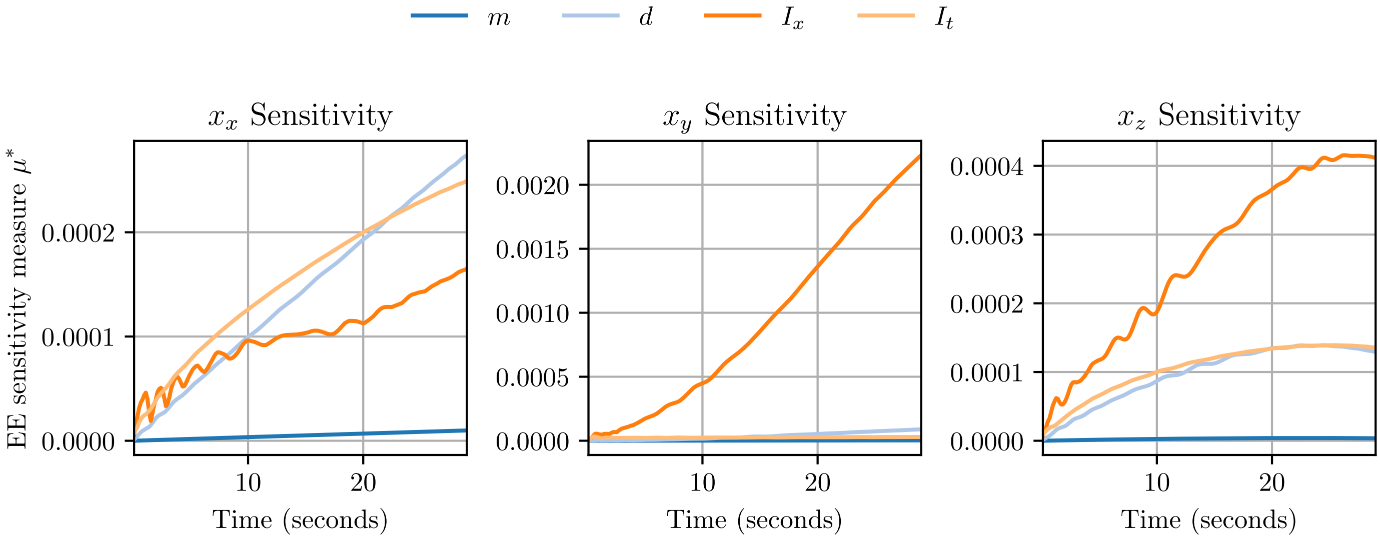

Figure E.3: Sensitivity to projectile properties

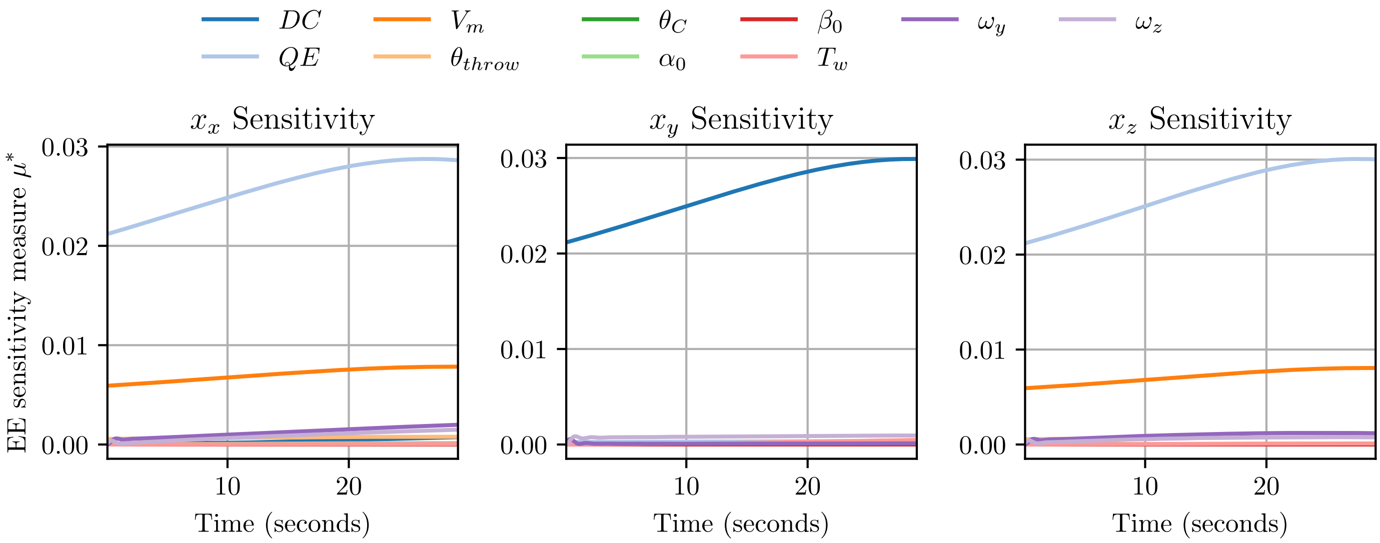

Figure E.4: Sensitivity to location and initial conditions

E.1.2 Velocity sensitivity

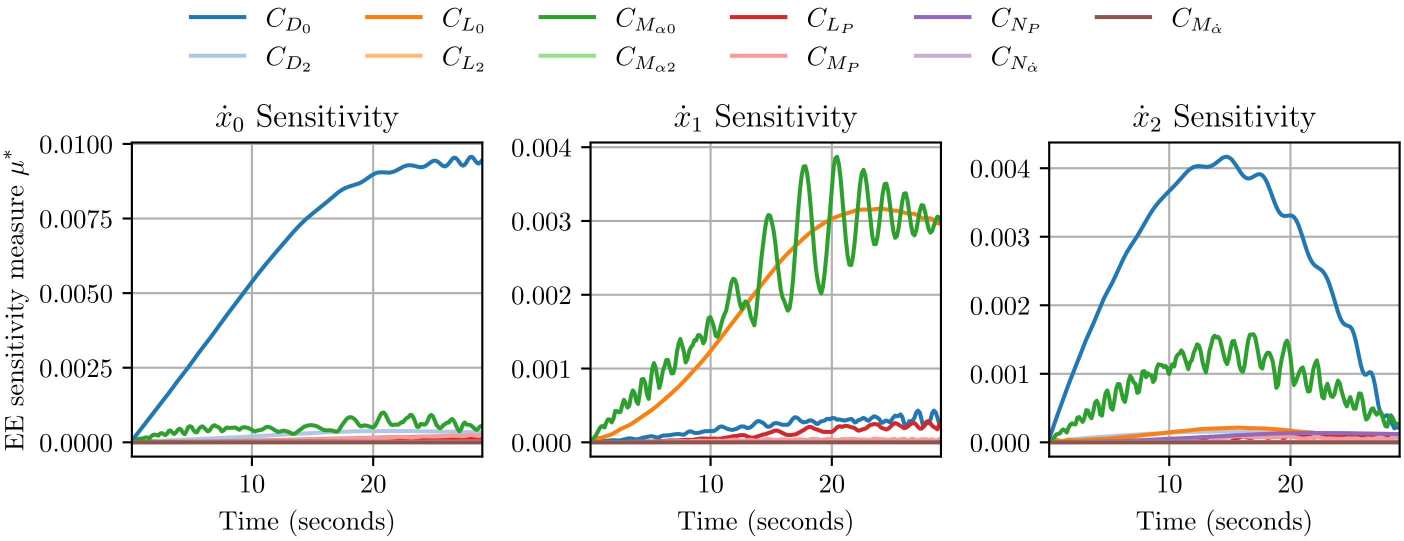

Figure E.5: Sensitivity to aerodynamic coefficients

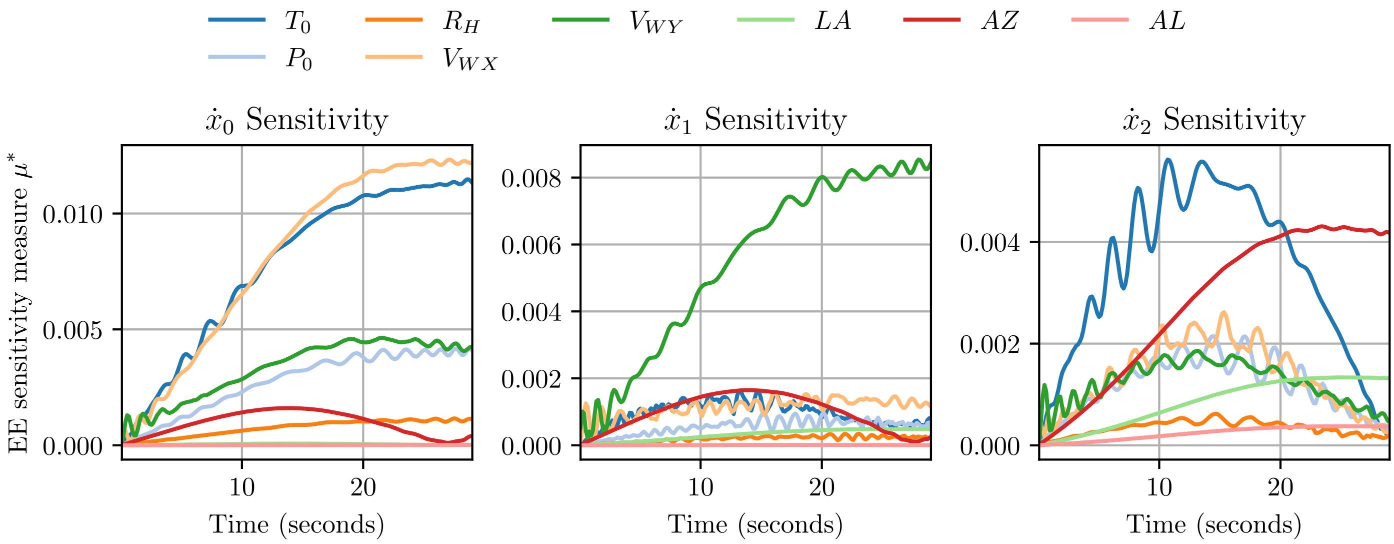

Figure E.6: Sensitivity to location and ambient conditions

.

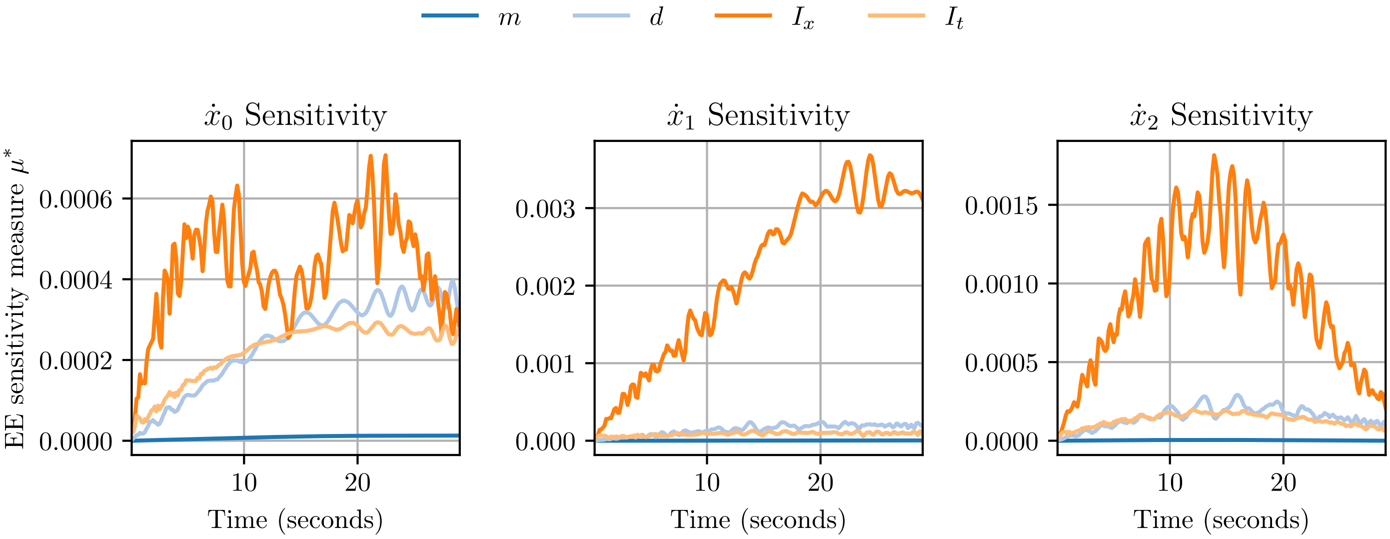

Figure E.7: Sensitivity to projectile properties

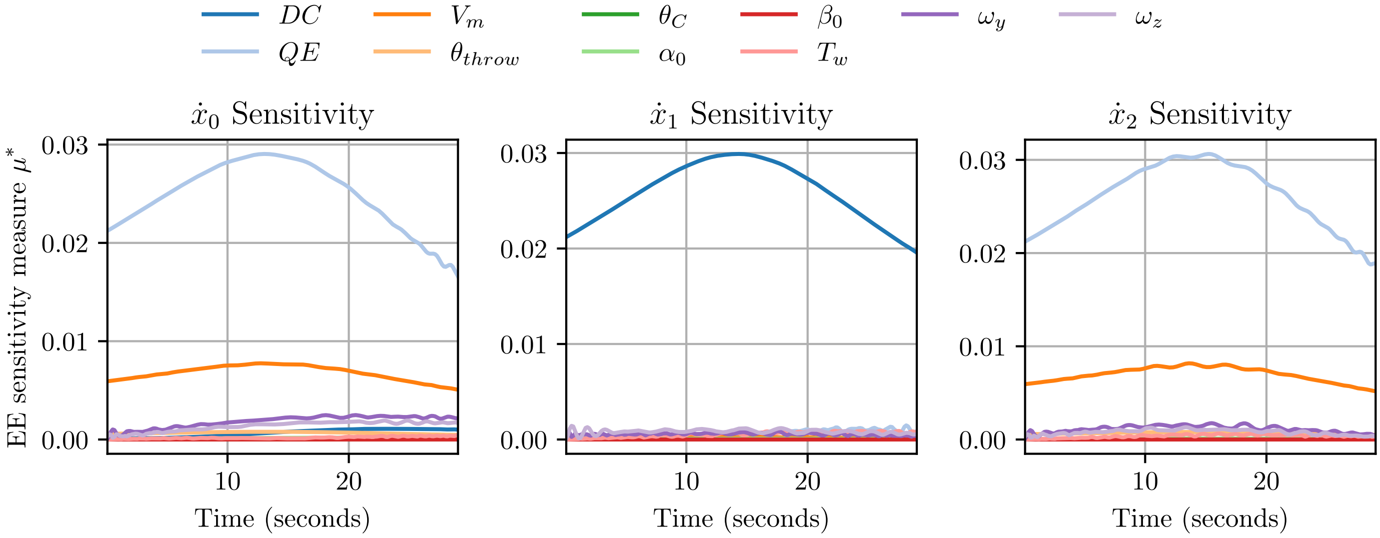

Figure E.8: Sensitivity to location and initial conditions

E.1.3 Angular velocity

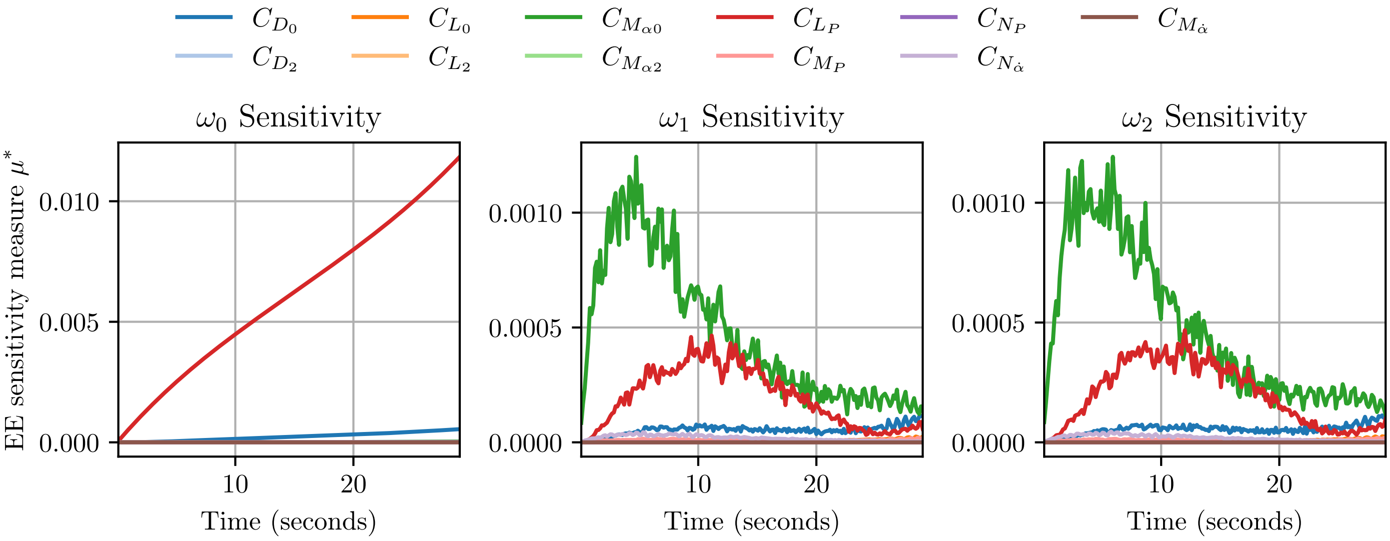

Figure E.9: Sensitivity to aerodynamic coefficients

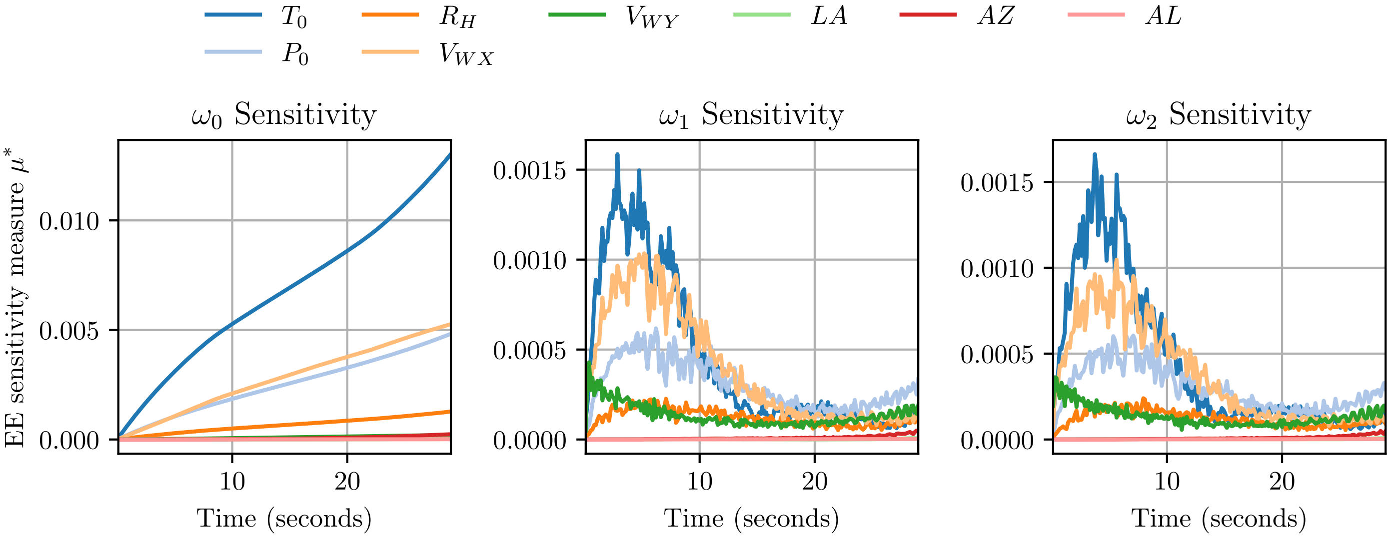

Figure E.10: Sensitivity to location and ambient conditions

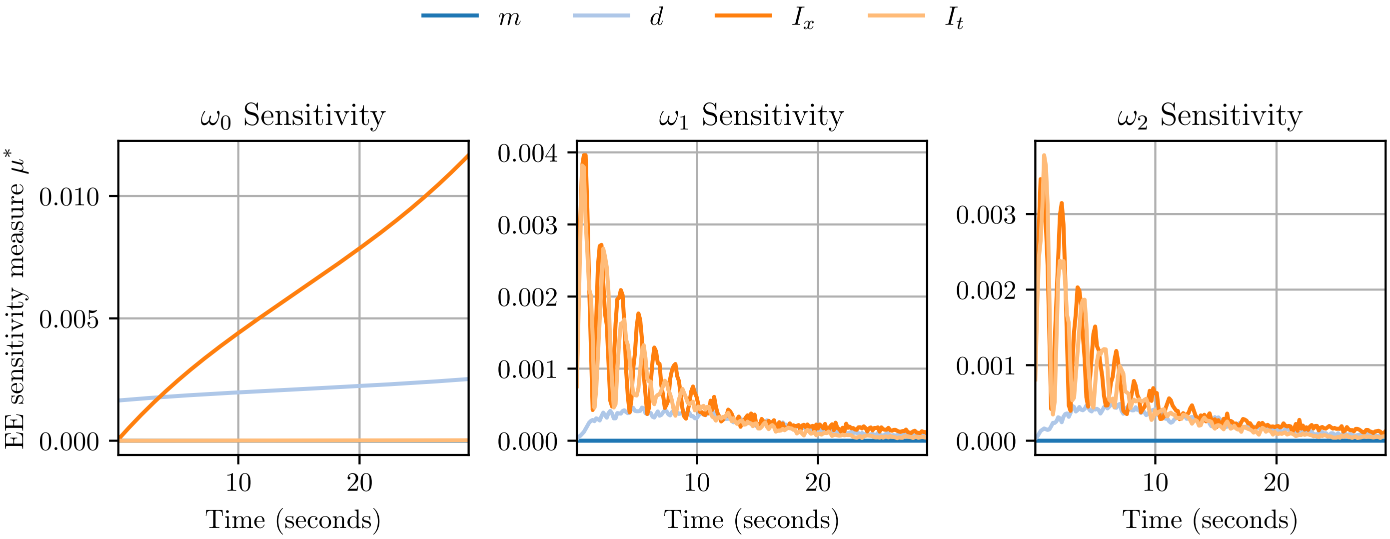

Figure E.11: Sensitivity to projectile properties

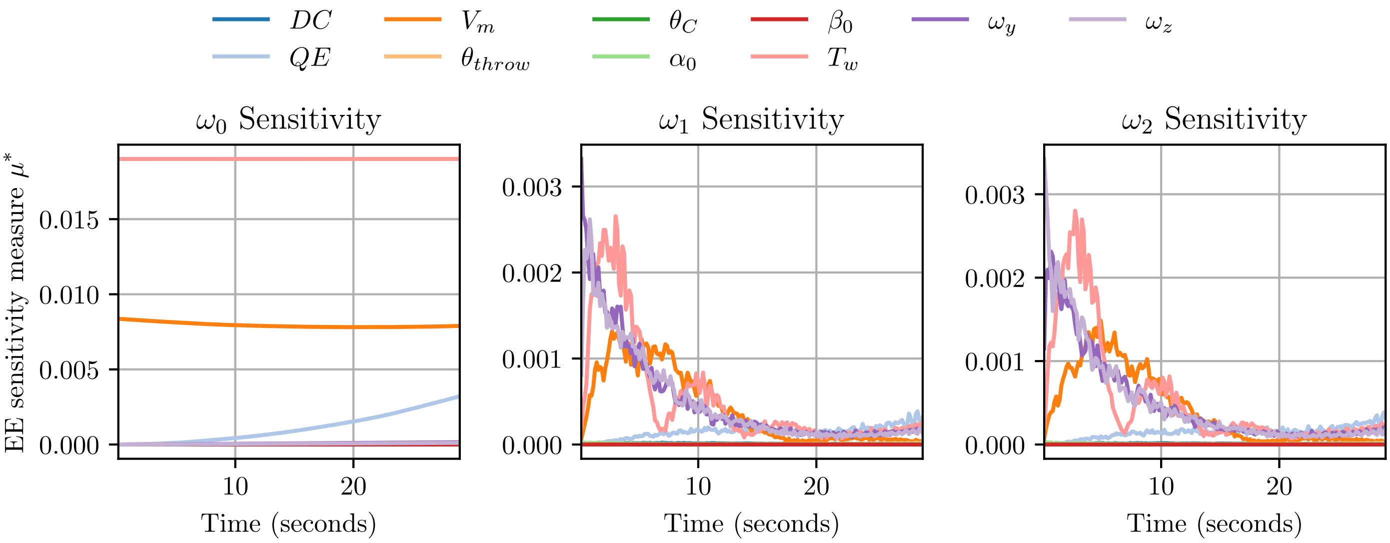

Figure E.12: Sensitivity to location and initial conditions

E.2 Subsonic, QE = 70 study

E.2.1 Position sensitivity

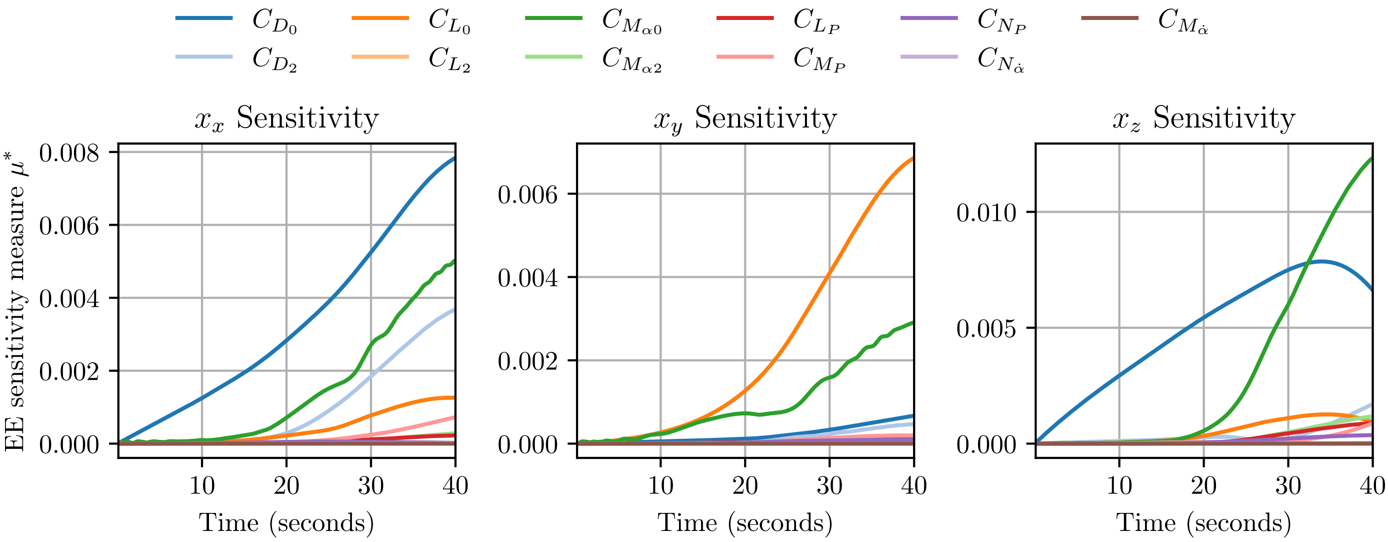

Figure E.13: Sensitivity to aerodynamic coefficients

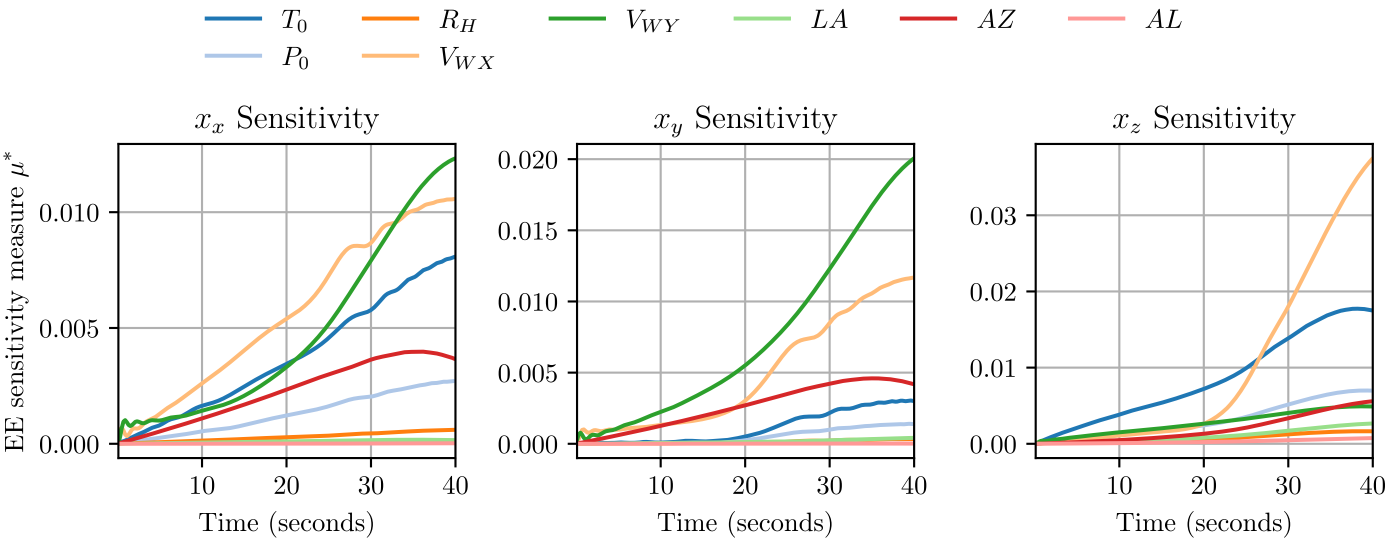

Figure E.14: Sensitivity to location and ambient conditions

.

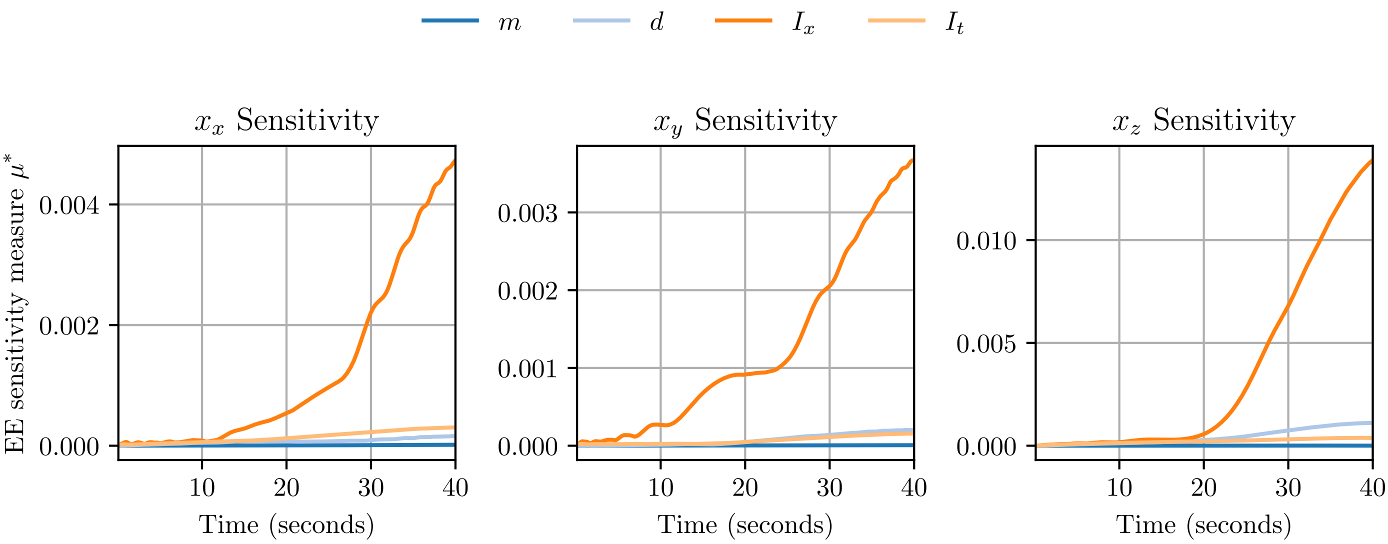

Figure E.15: Sensitivity to projectile properties

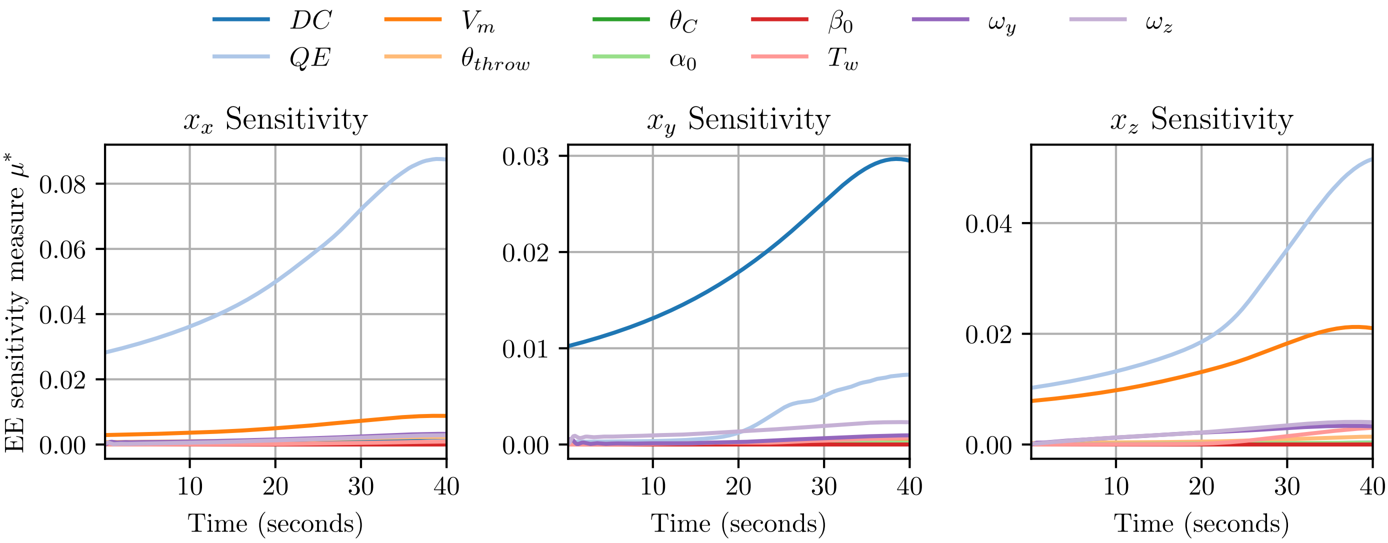

Figure E.16: Sensitivity to location and initial conditions

E.2.2 Velocity sensitivity

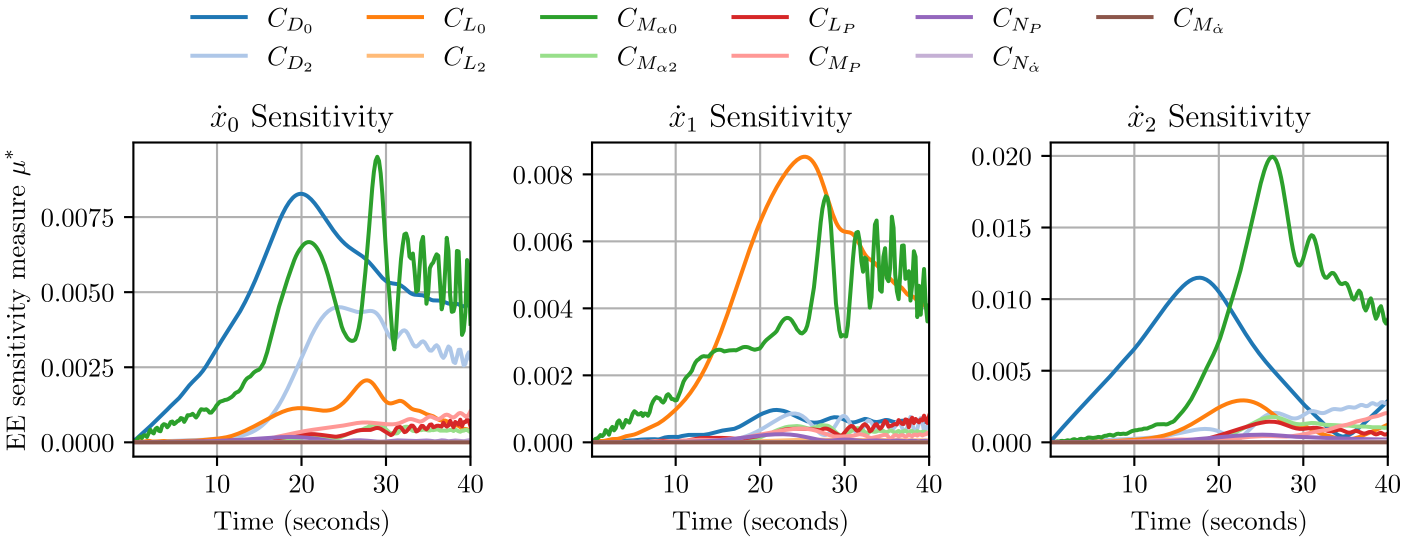

Figure E.17: Sensitivity to aerodynamic coefficients

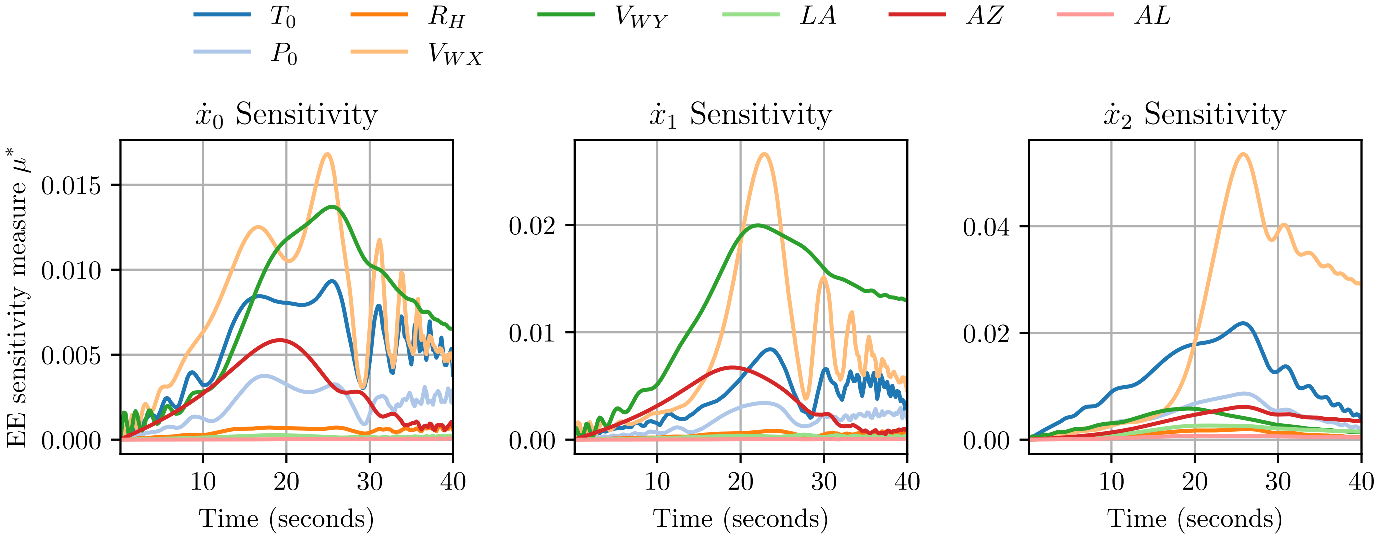

Figure E.18: Sensitivity to location and ambient conditions

.

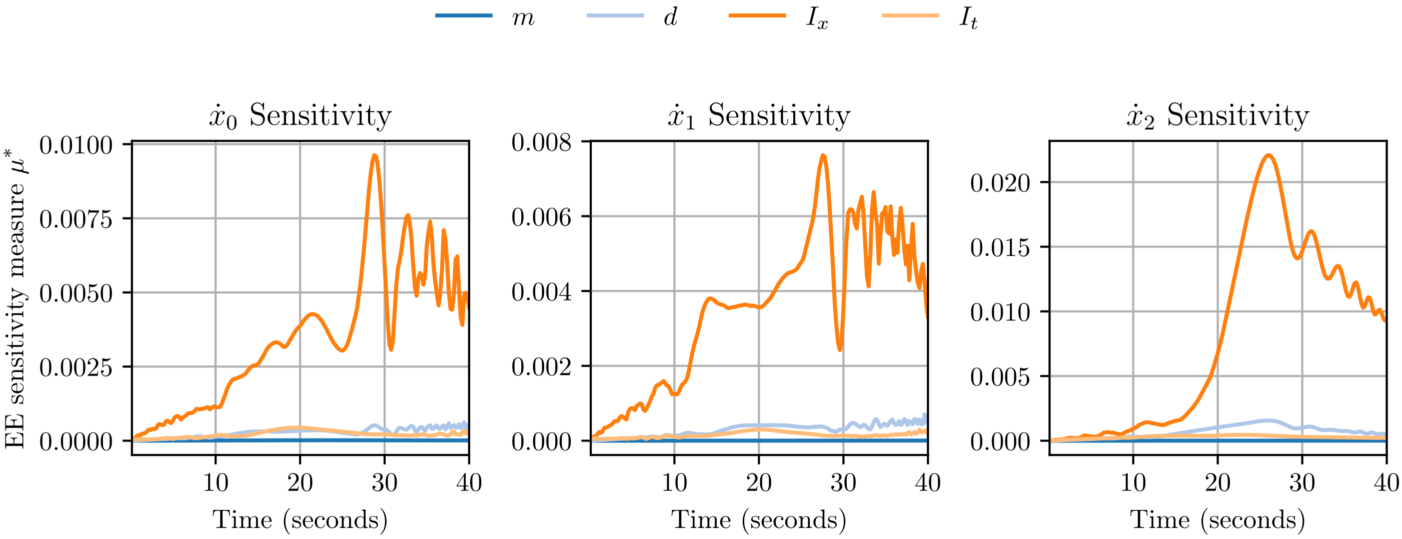

Figure E.19: Sensitivity to projectile properties

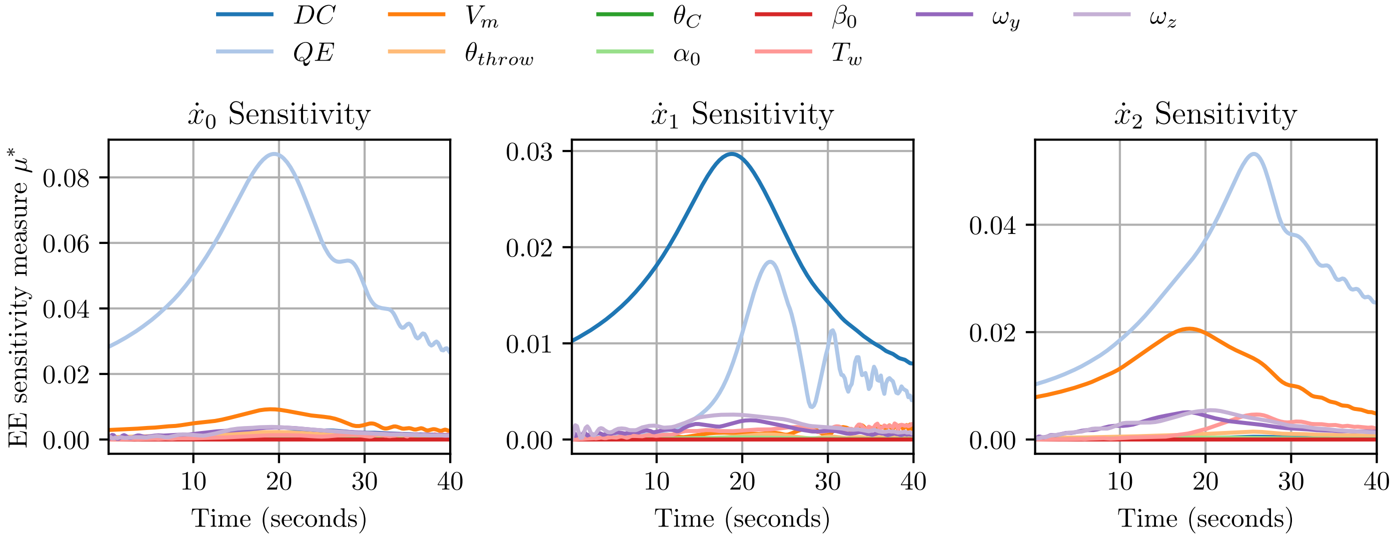

Figure E.20: Sensitivity to location and initial conditions

E.2.3 Angular velocity sensitivity

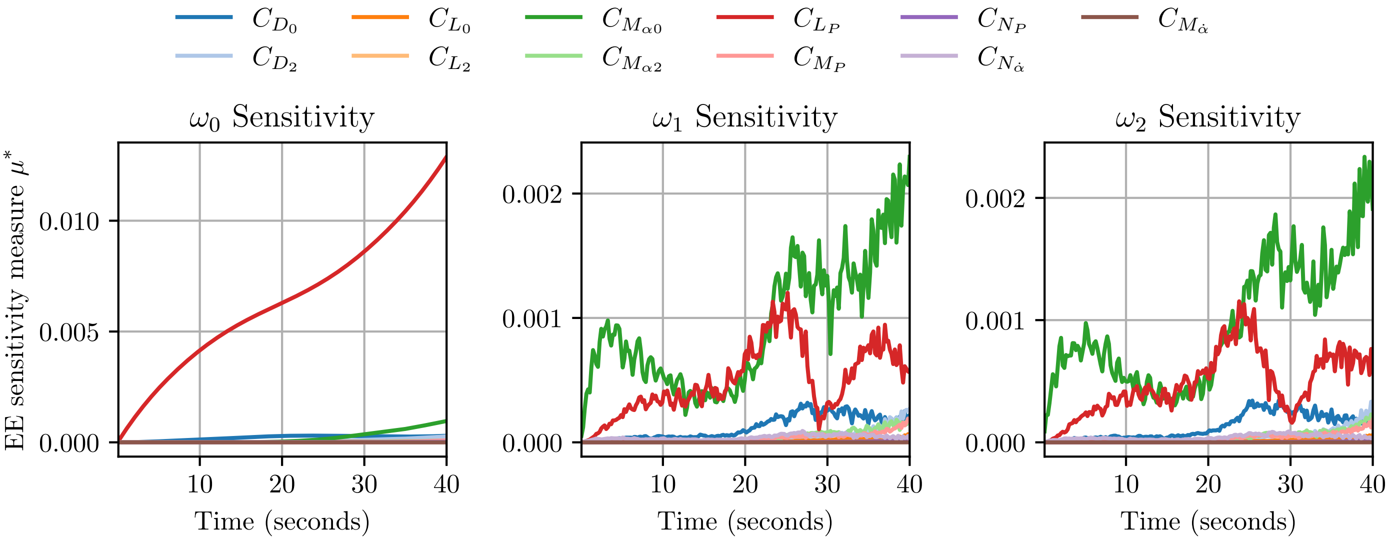

Figure E.21: Sensitivity to aerodynamic coefficients

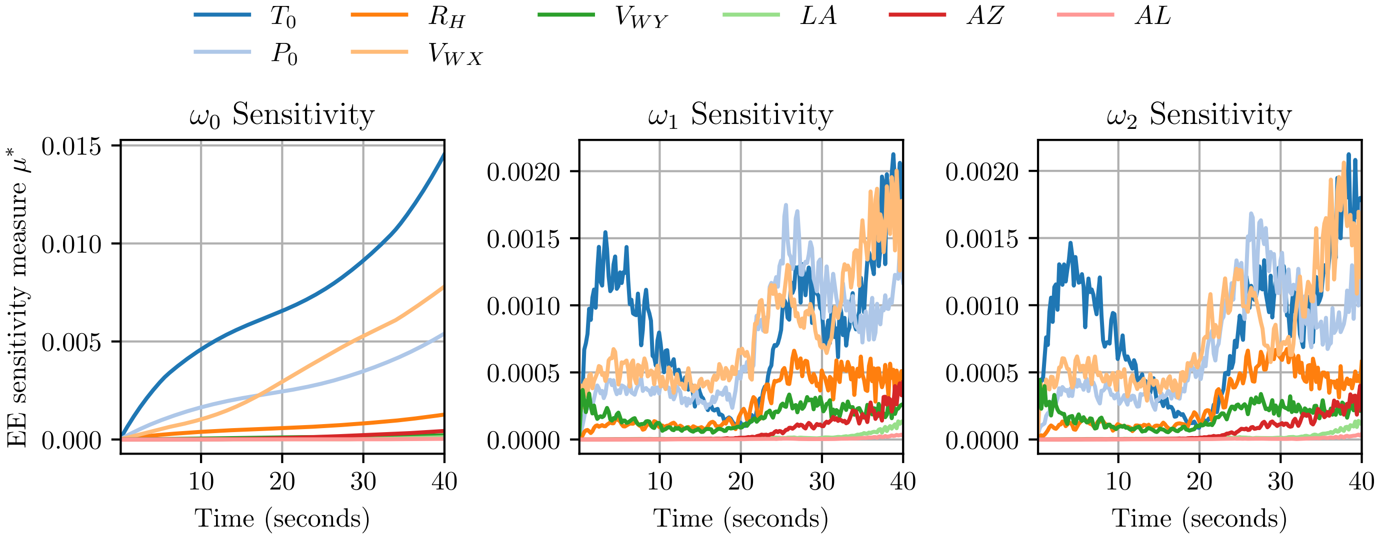

Figure E.22: Sensitivity to location and ambient conditions

.

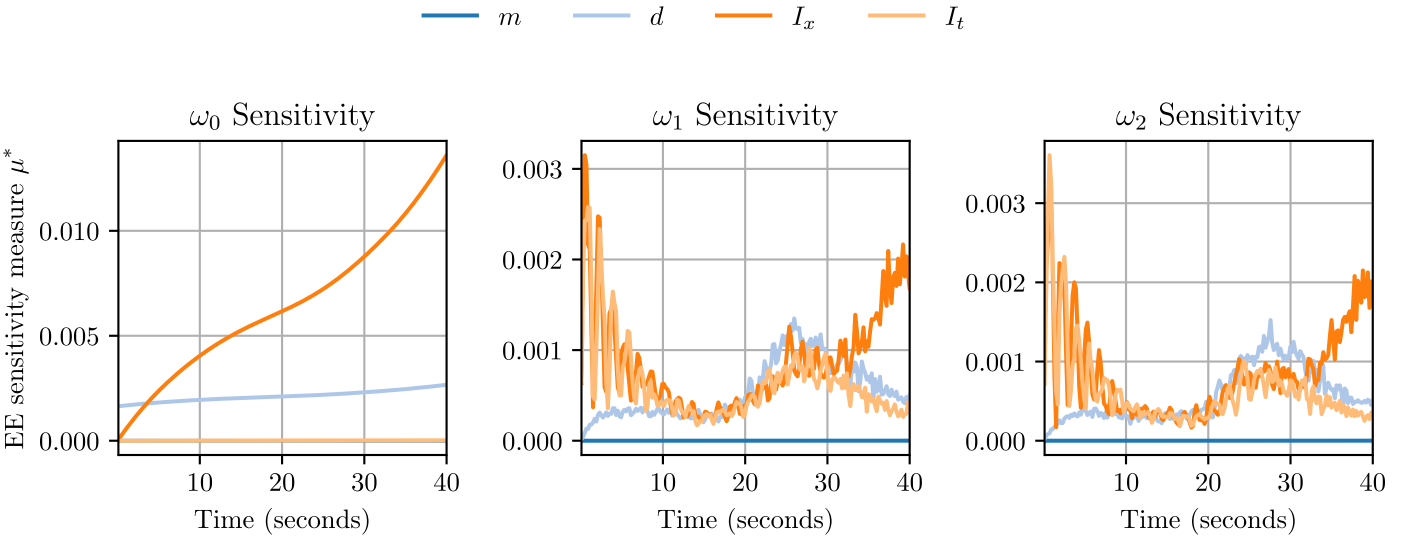

Figure E.23: Sensitivity to projectile properties

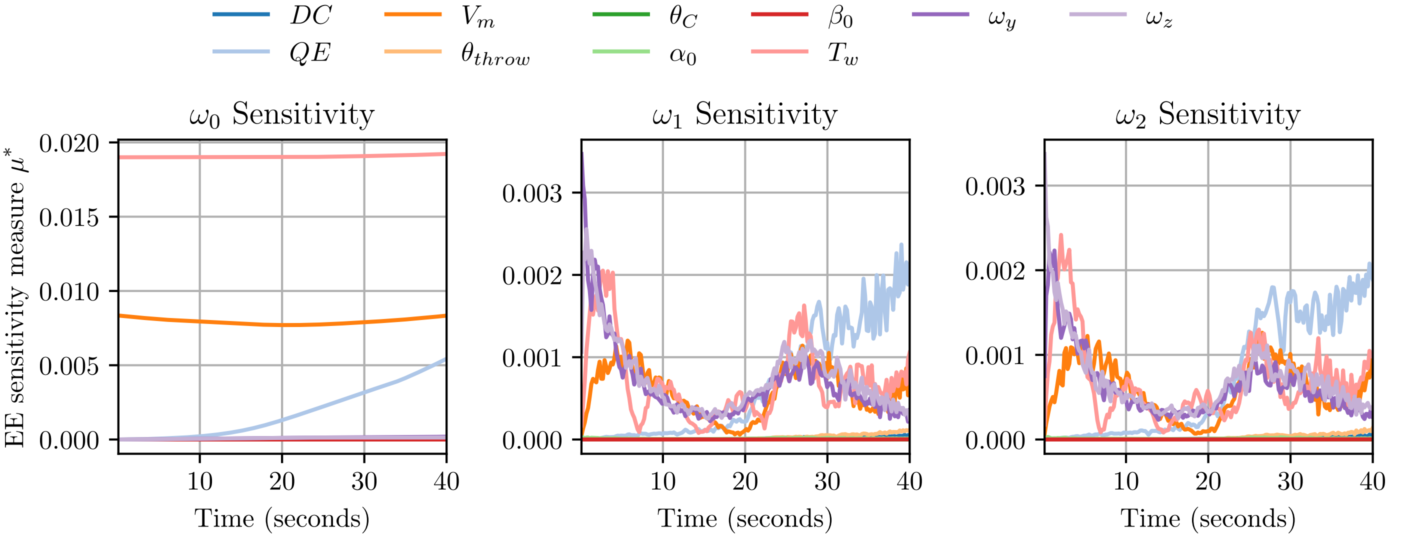

Figure E.24: Sensitivity to location and initial conditions

E.3 Supersonic, QE = 45 study

E.3.1 Position sensitivity

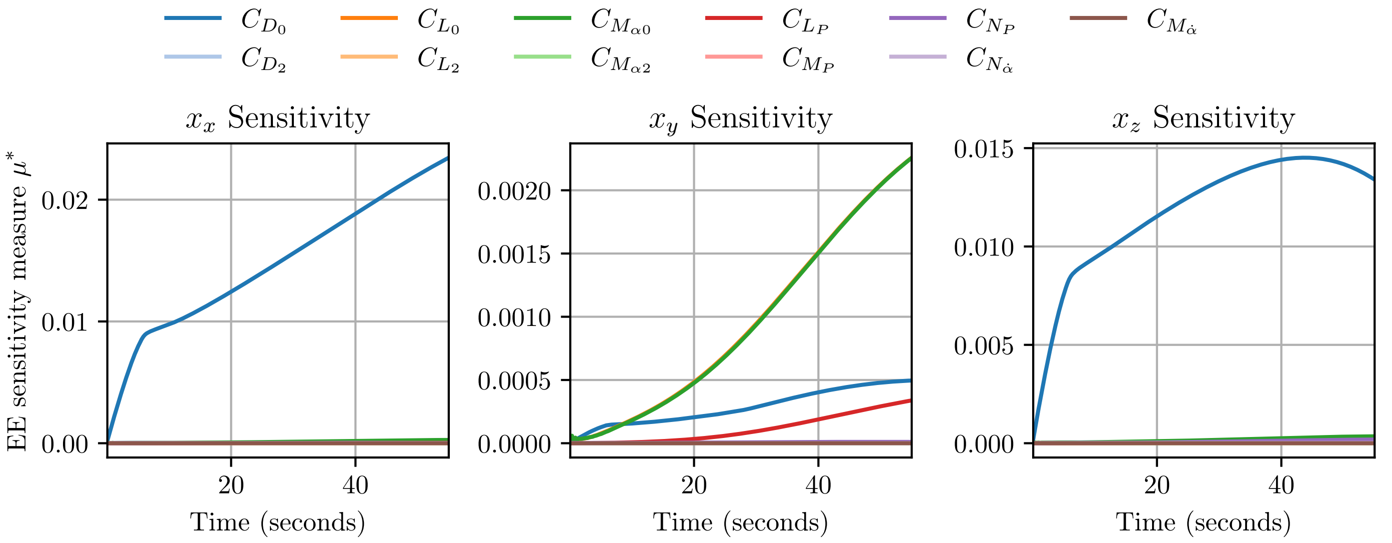

Figure E.25: Sensitivity to aerodynamic coefficients

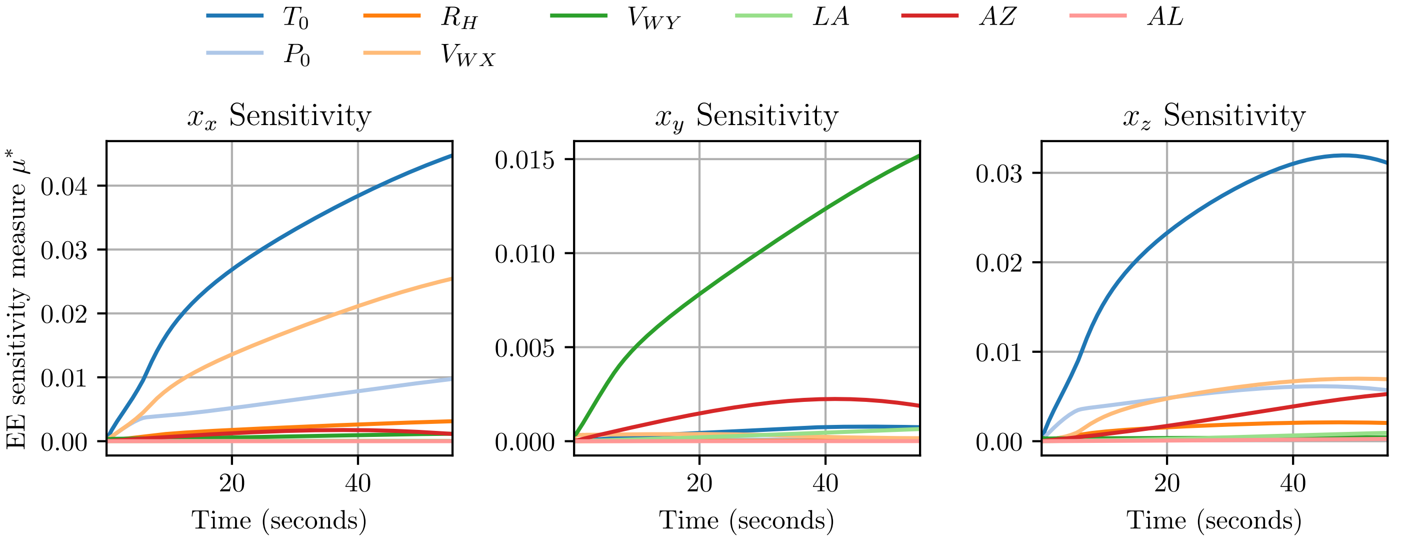

Figure E.26: Sensitivity to location and ambient conditions

.

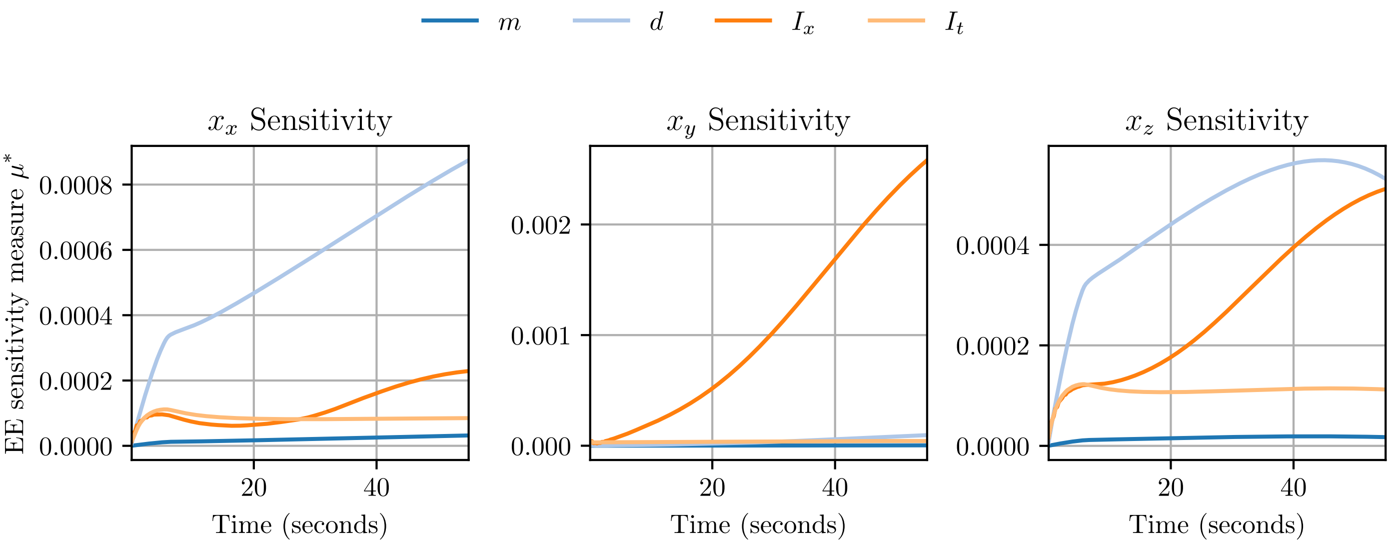

Figure E.27: Sensitivity to projectile properties

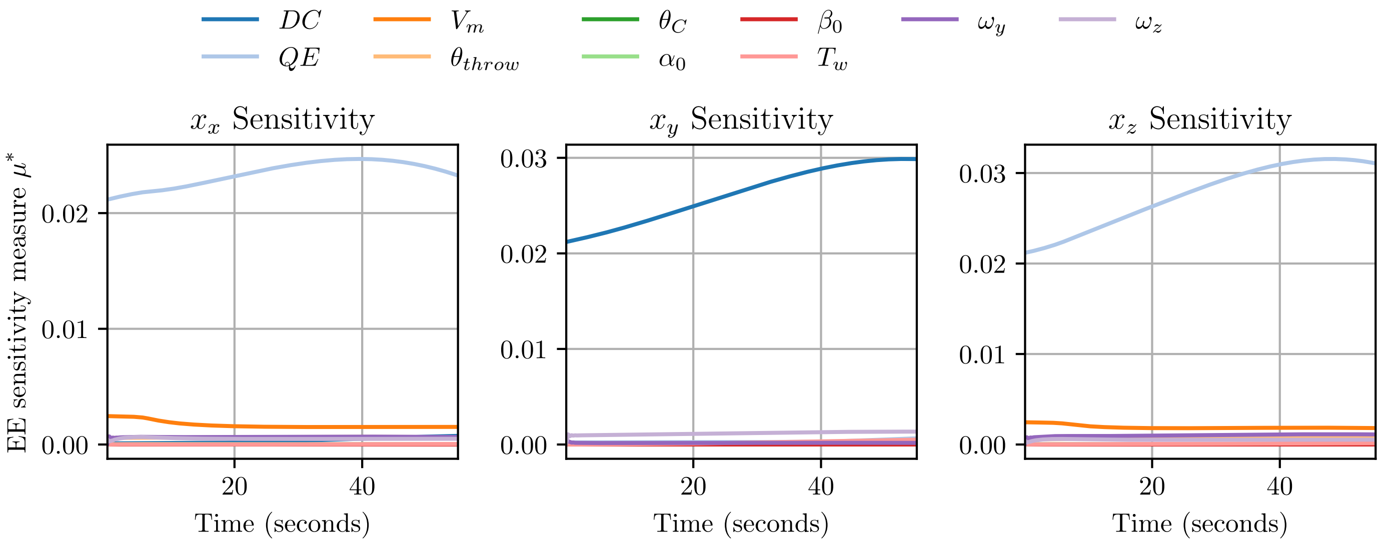

Figure E.28: Sensitivity to location and initial conditions

E.3.2 Velocity sensitivity

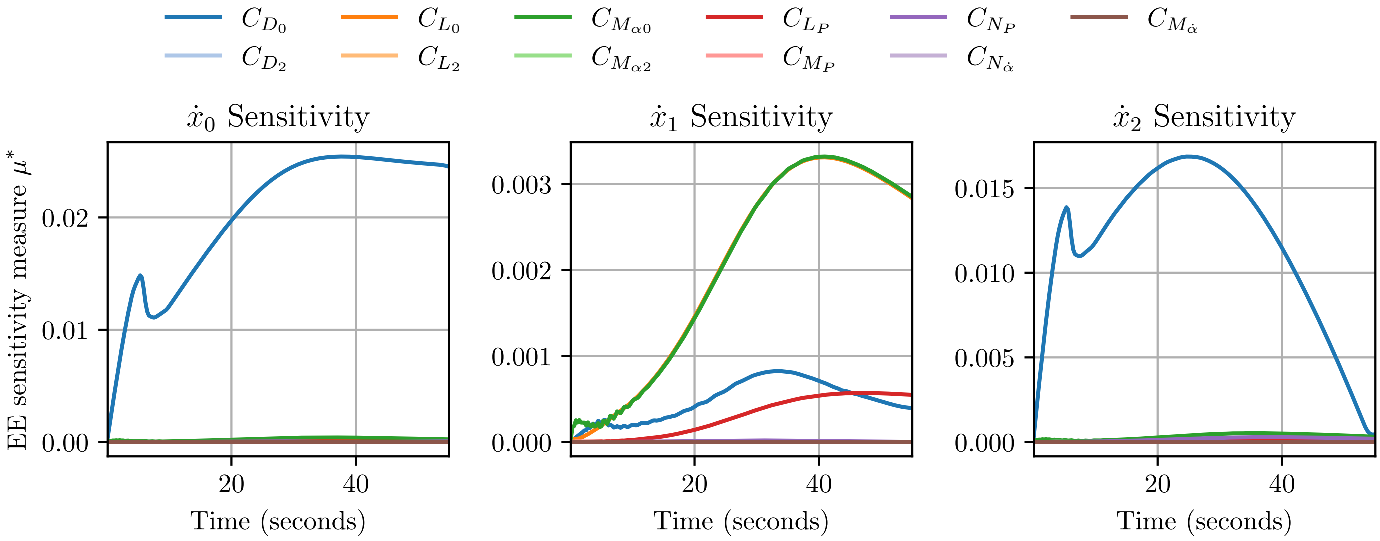

Figure E.29: Sensitivity to aerodynamic coefficients

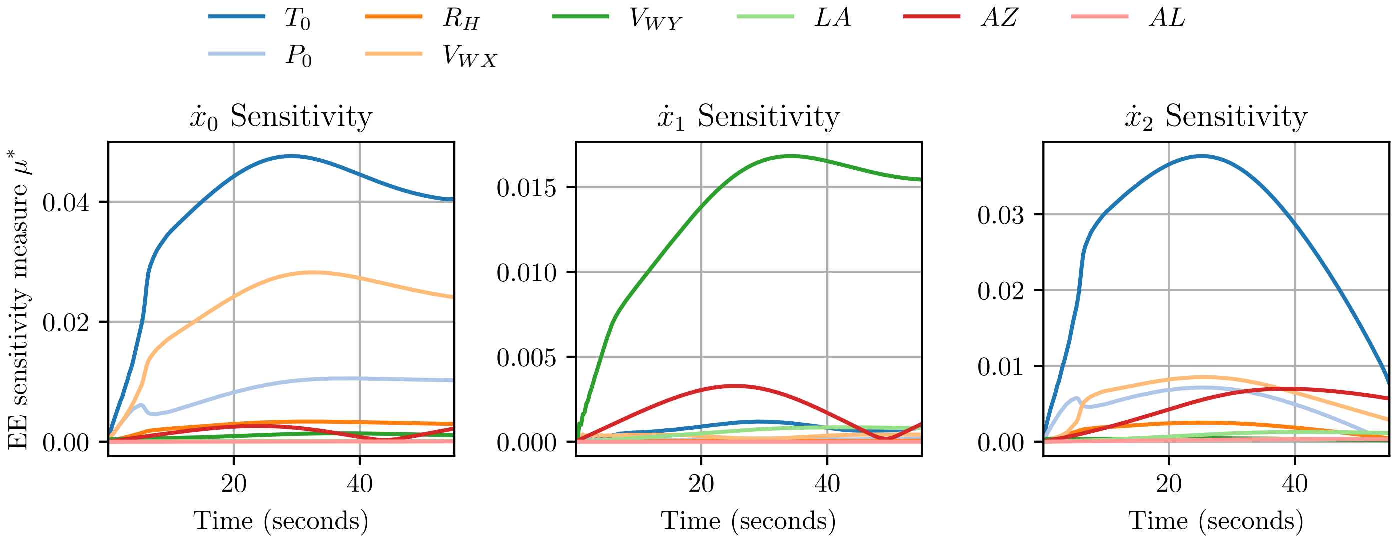

Figure E.30: Sensitivity to location and ambient conditions

.

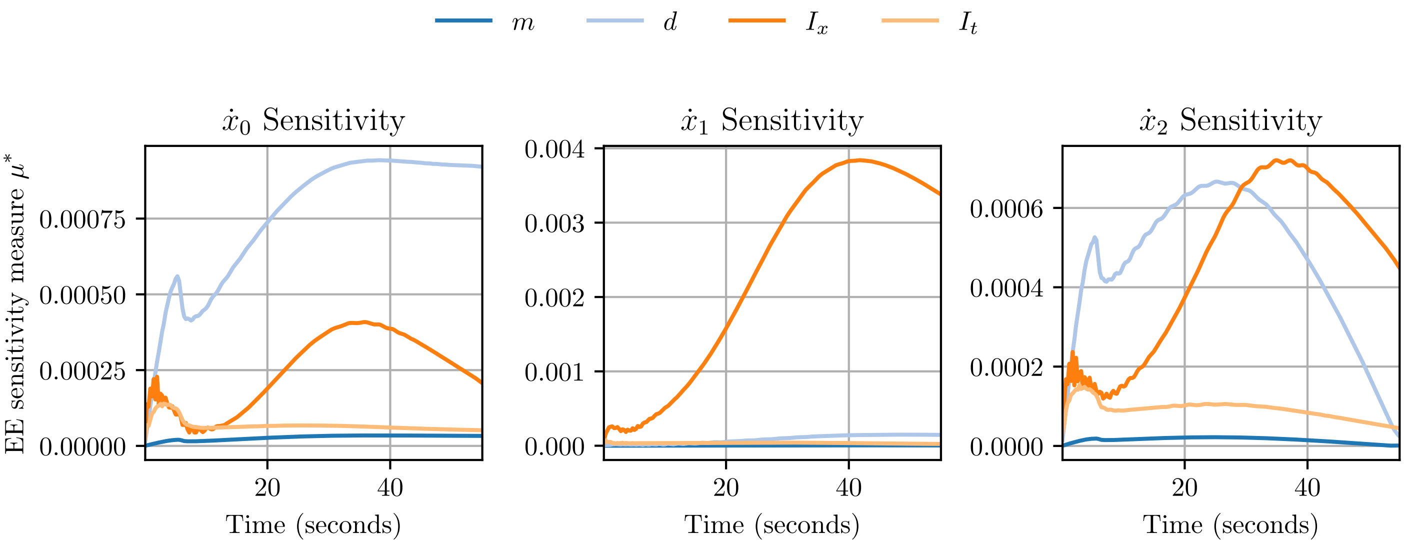

Figure E.31: Sensitivity to projectile properties

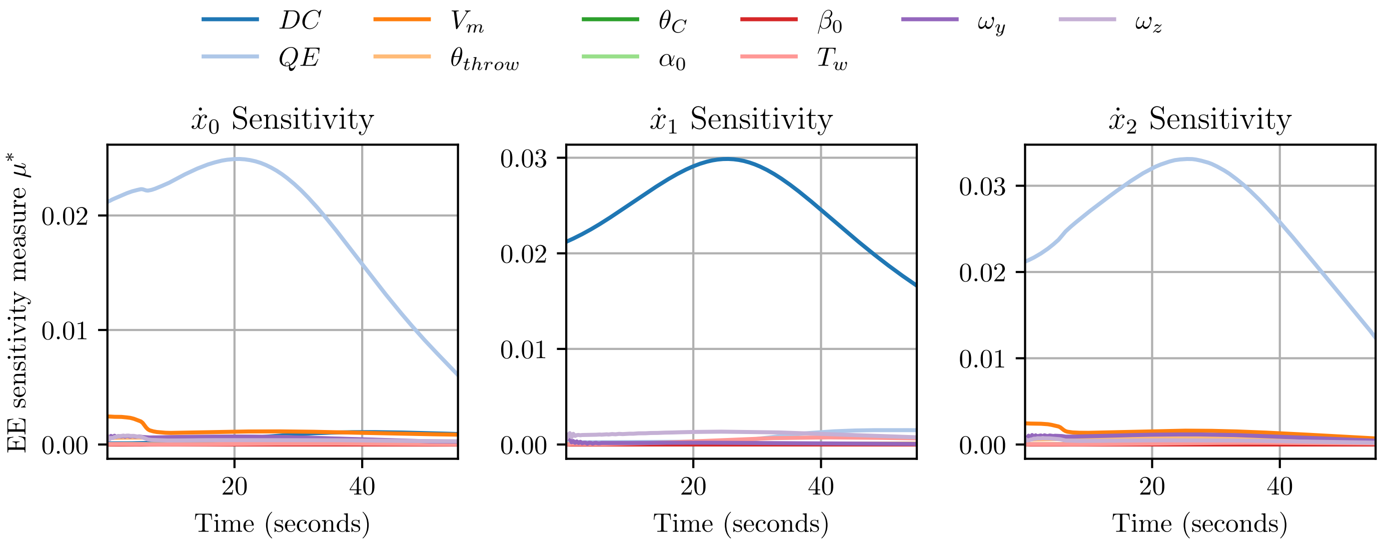

Figure E.32: Sensitivity to location and initial conditions

E.3.3 Angular velocity sensitivity

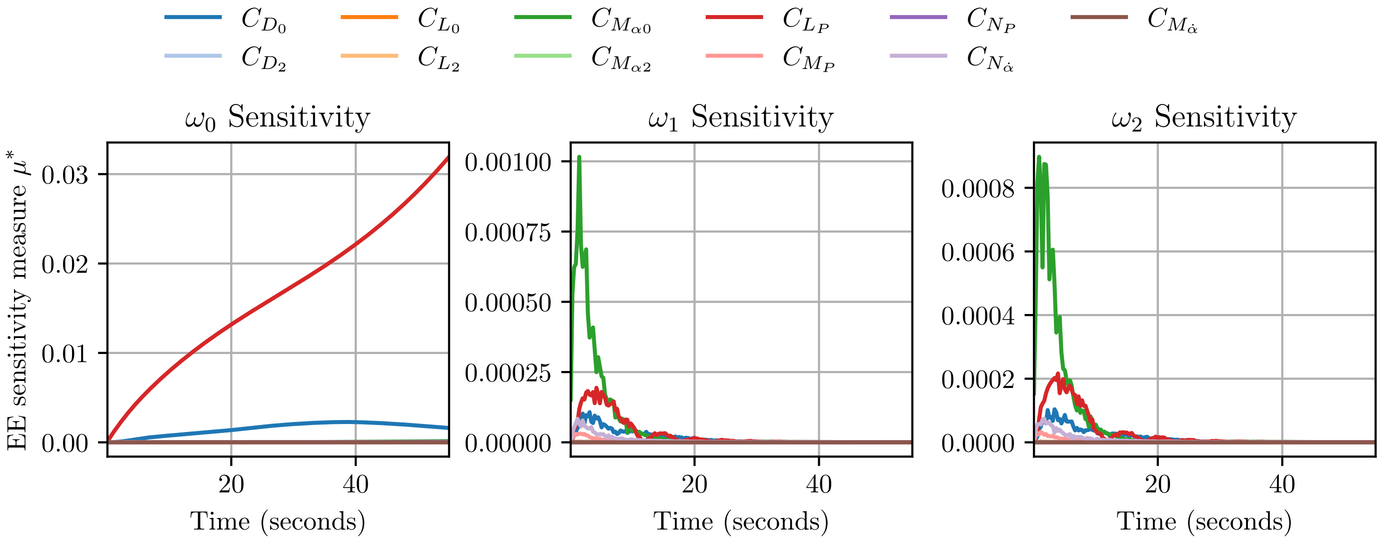

Figure E.33: Sensitivity to aerodynamic coefficients

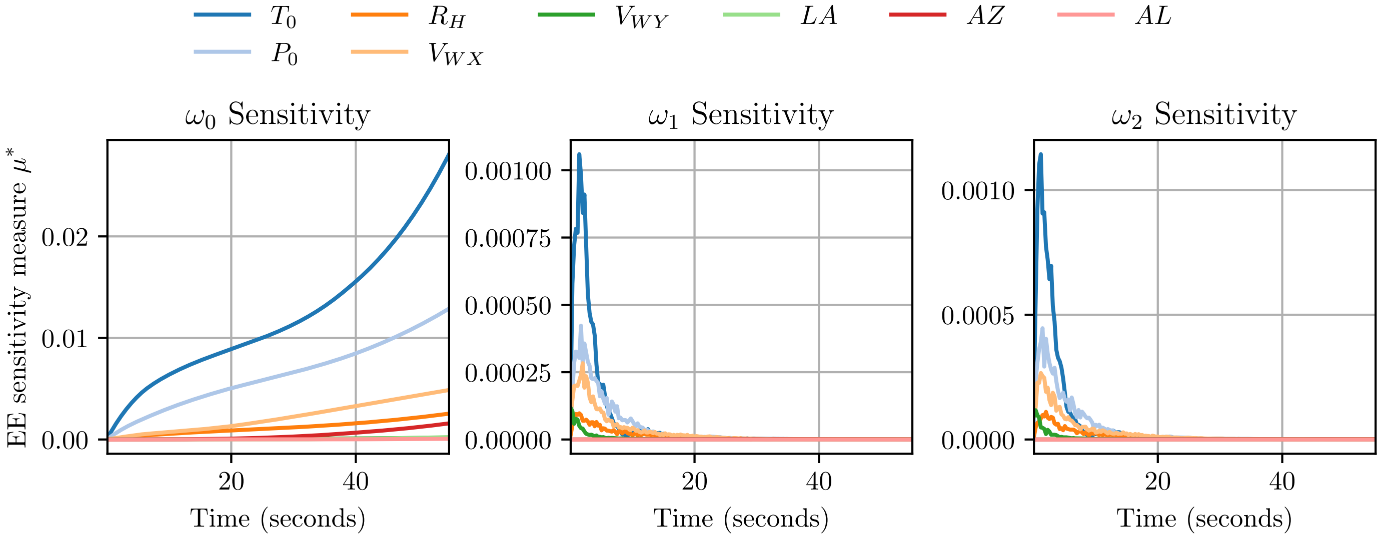

Figure E.34: Sensitivity to location and ambient conditions

.

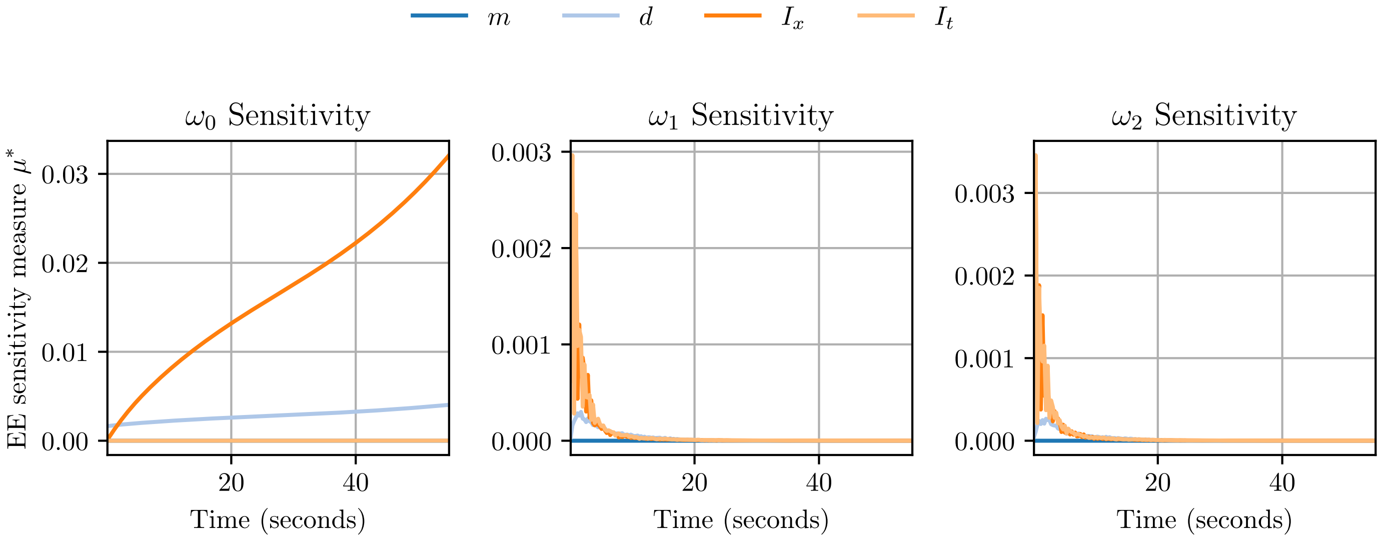

Figure E.35: Sensitivity to projectile properties

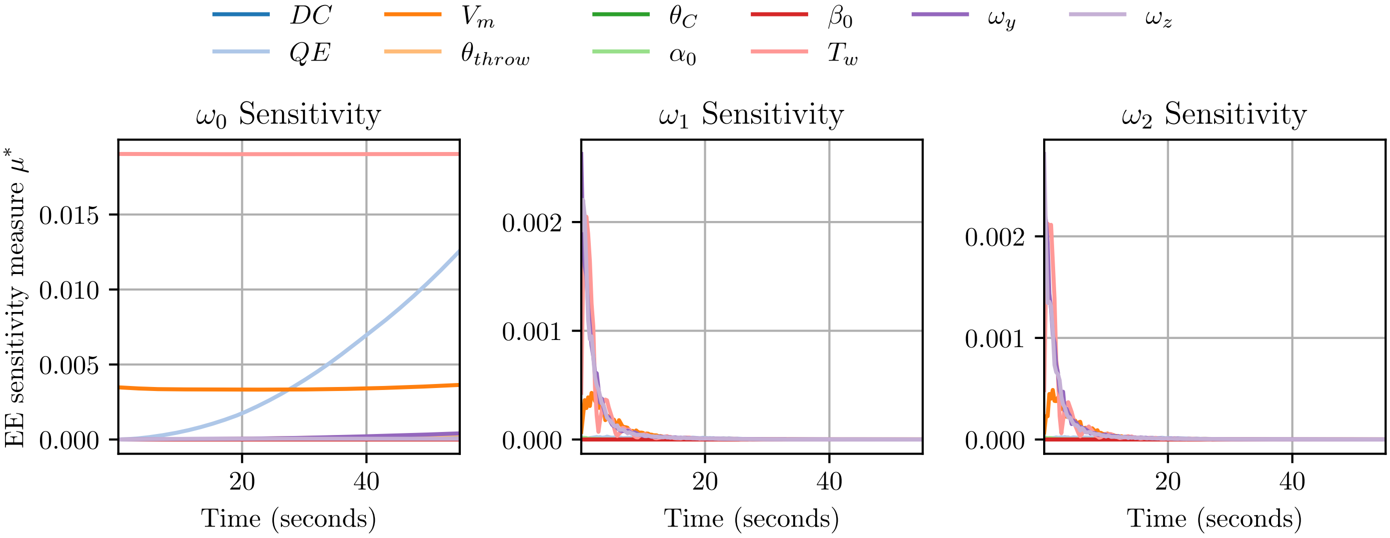

Figure E.36: Sensitivity to location and initial conditions

E.4 Supersonic, QE = 70 study

E.4.1 Position sensitivity

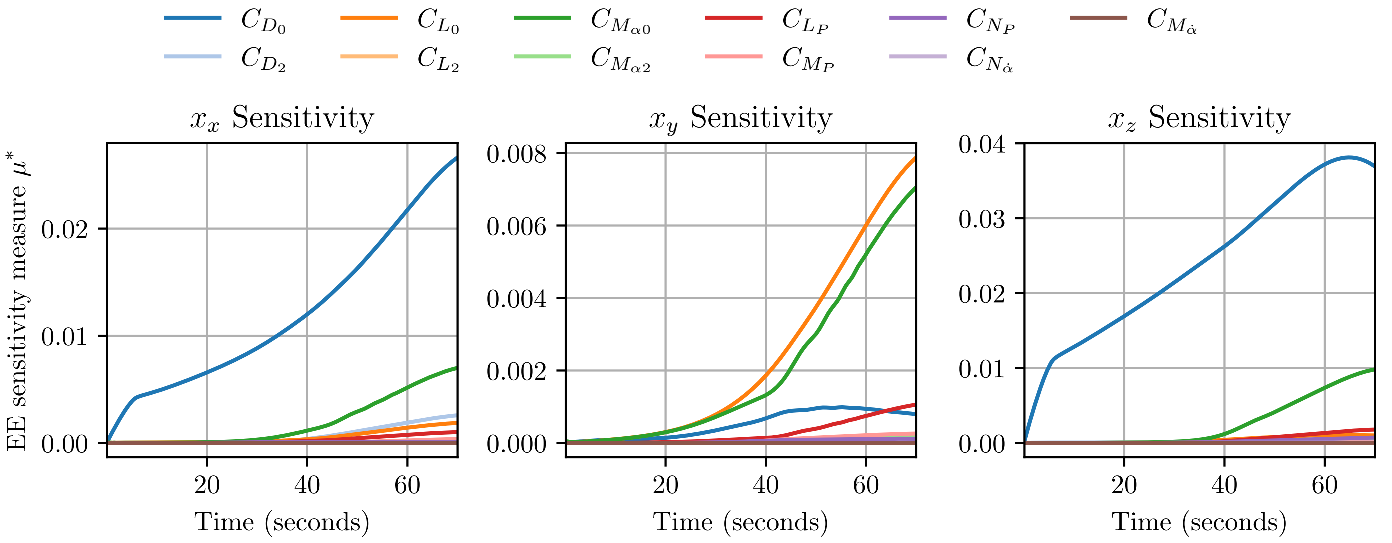

Figure E.37: Sensitivity to aerodynamic coefficients

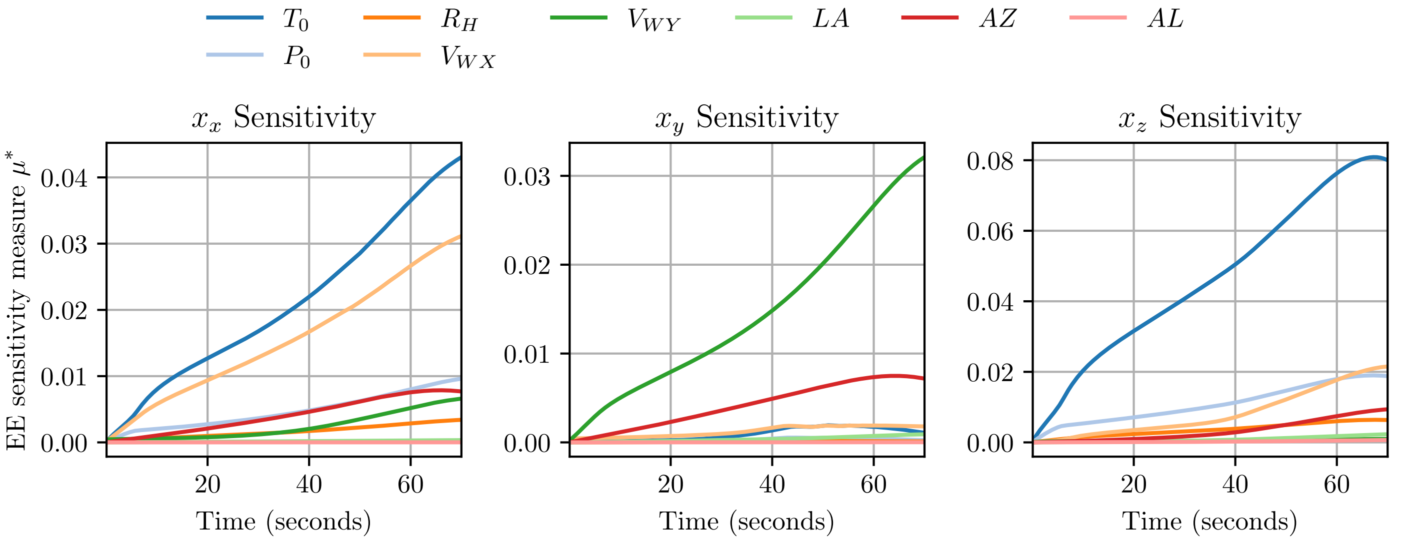

Figure E.38: Sensitivity to location and ambient conditions

.

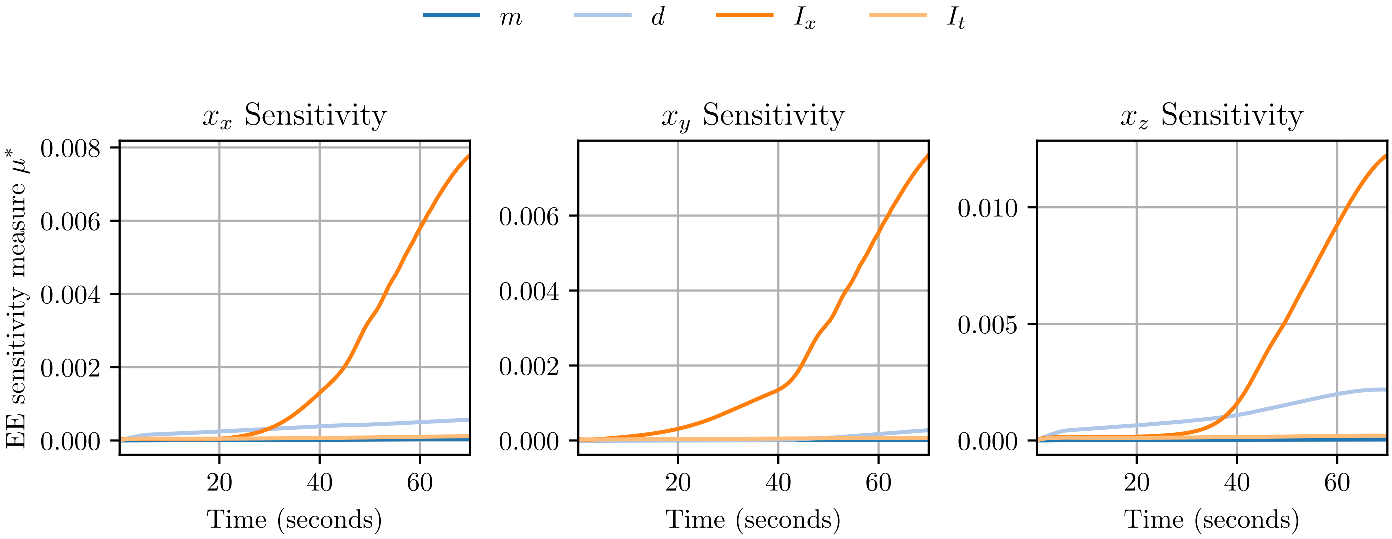

Figure E.39: Sensitivity to projectile properties

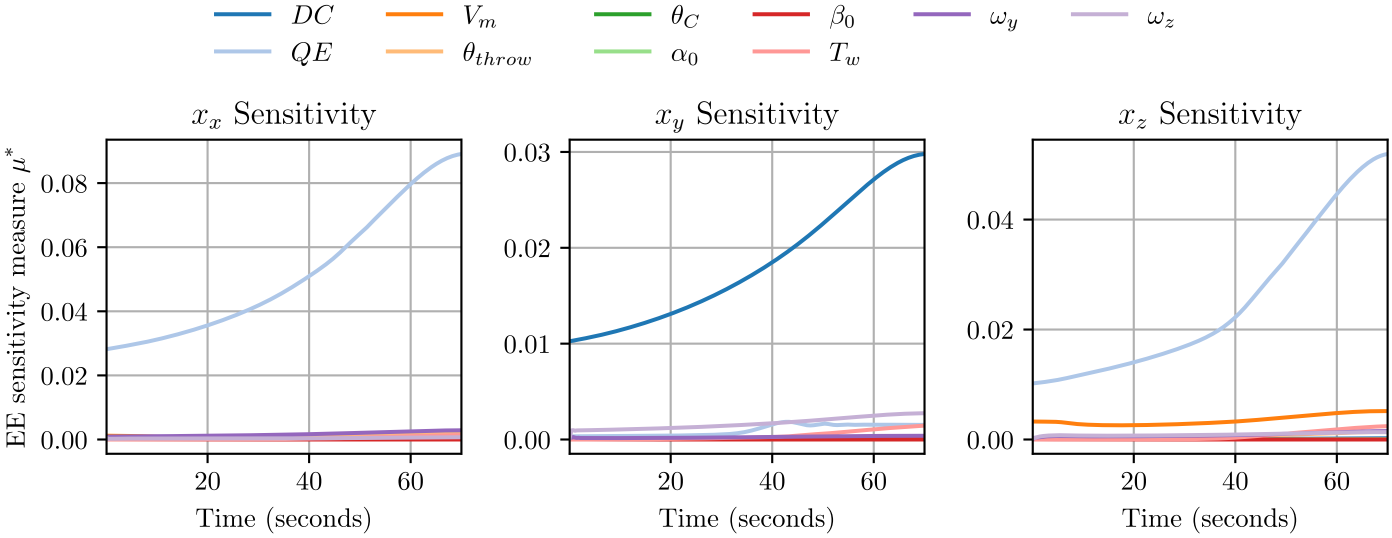

Figure E.40: Sensitivity to location and initial conditions

E.4.2 Velocity sensitivity

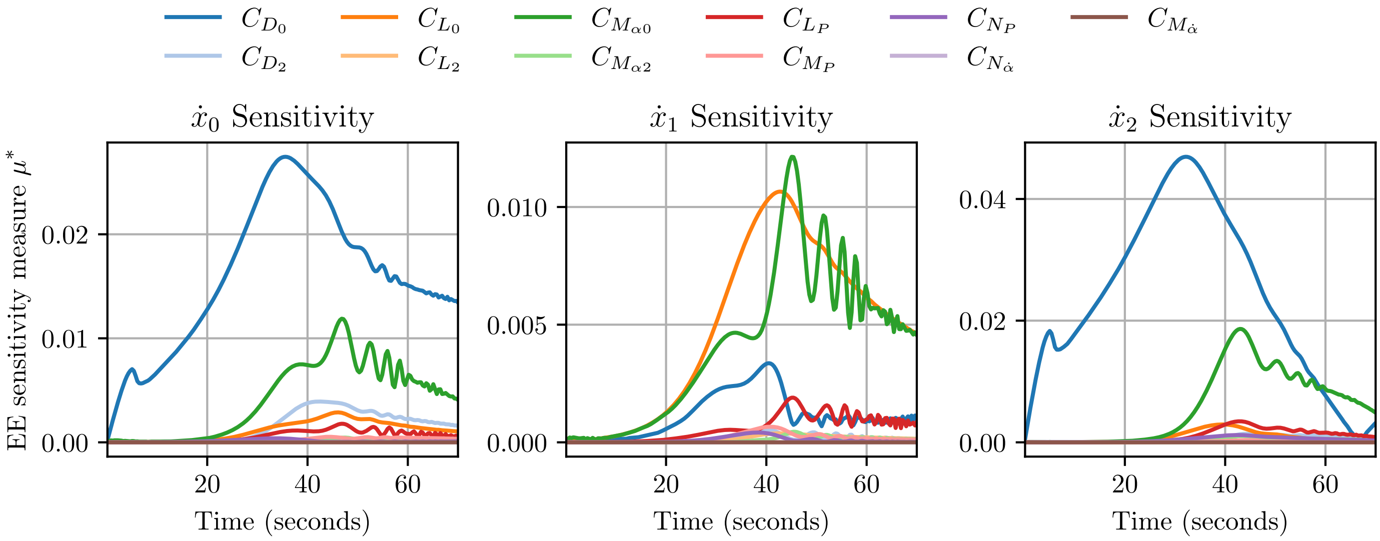

Figure E.41: Sensitivity to aerodynamic coefficients

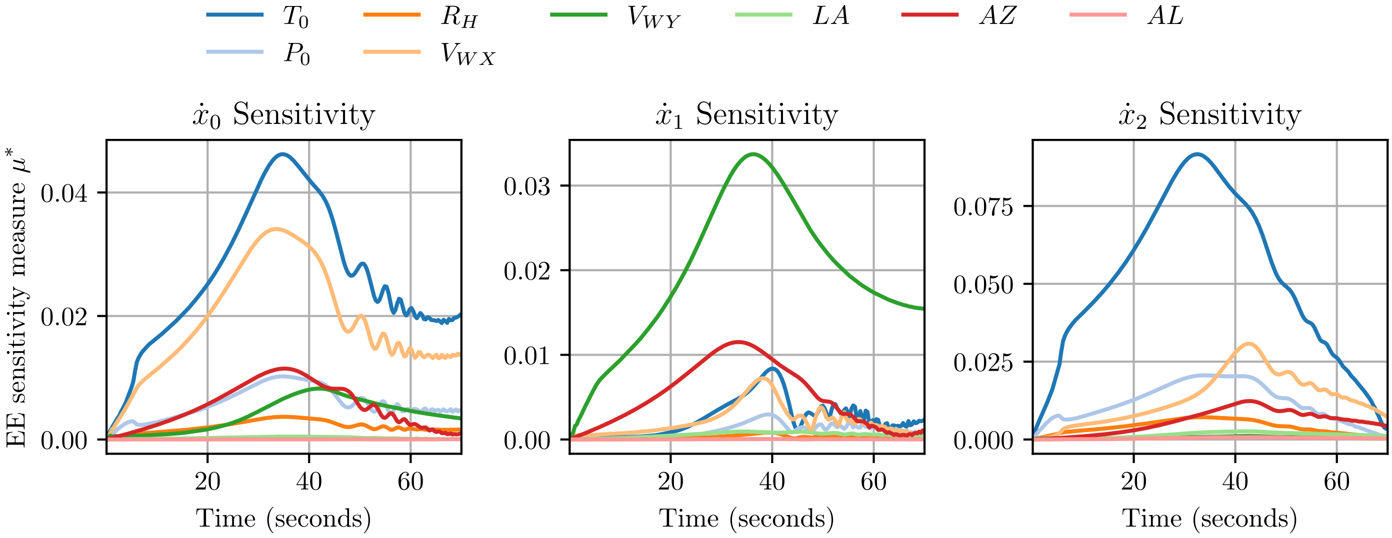

Figure E.42: Sensitivity to location and ambient conditions

.

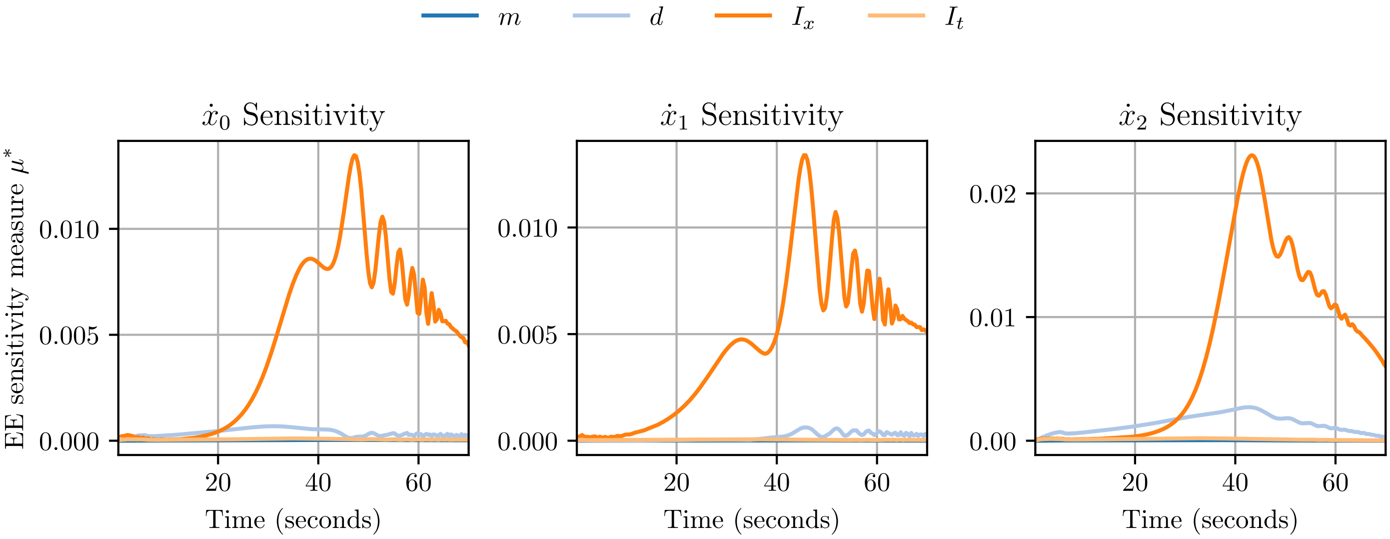

Figure E.43: Sensitivity to projectile properties

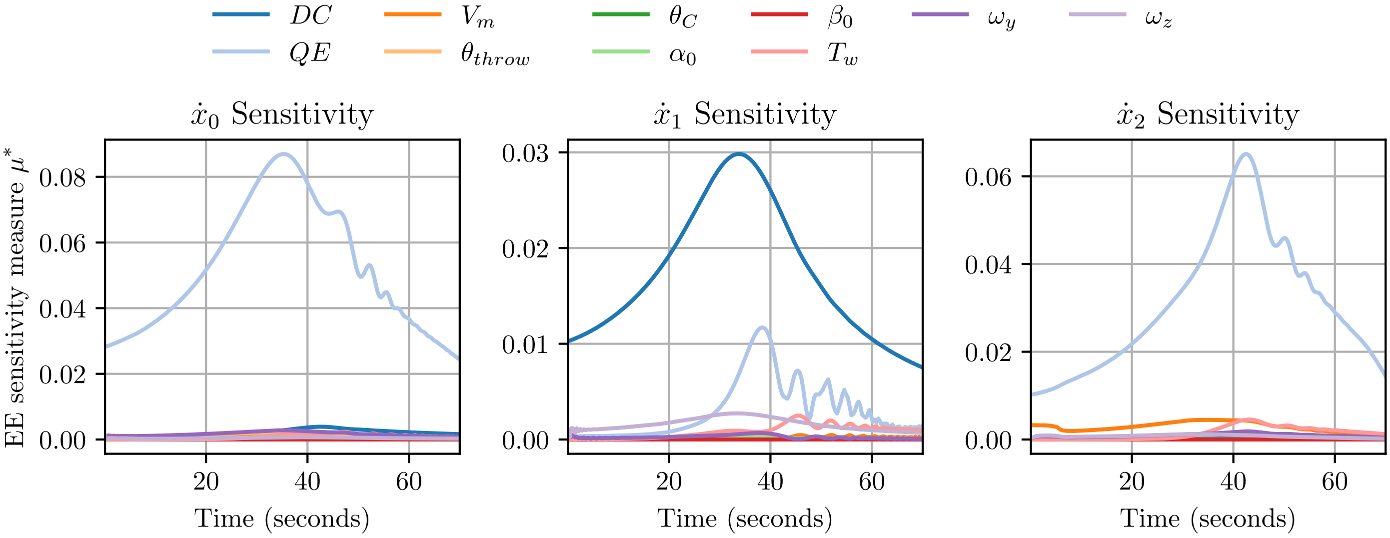

Figure E.44: Sensitivity to location and initial conditions

E.4.3 Angular velocity sensitivity

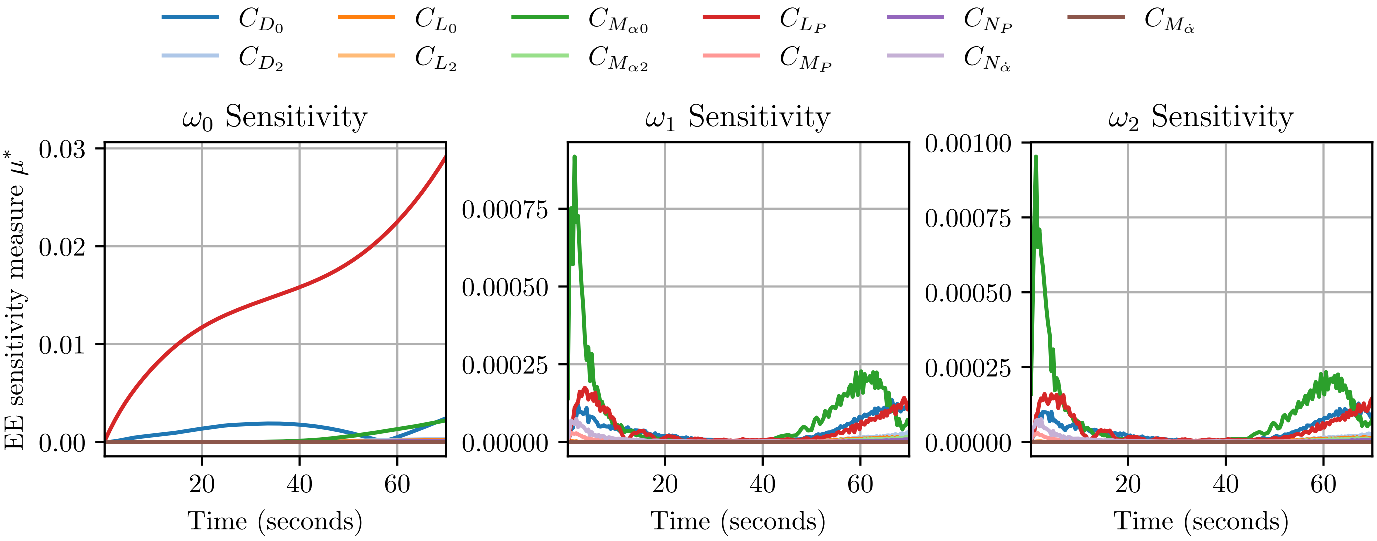

Figure E.45: Sensitivity to aerodynamic coefficients

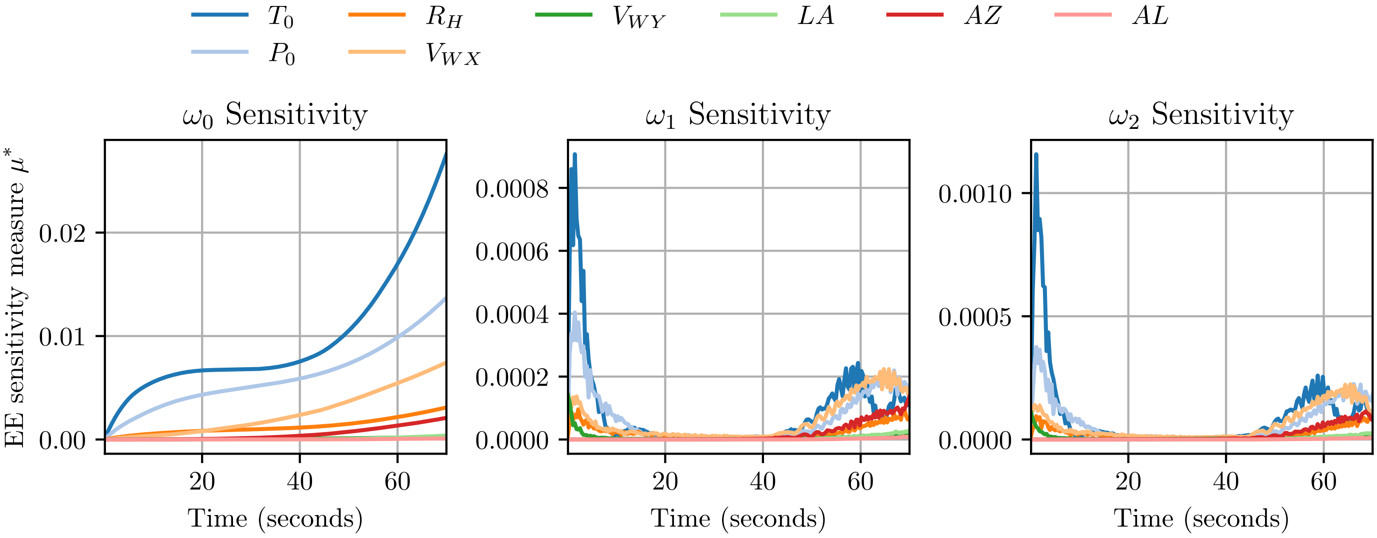

Figure E.46: Sensitivity to location and ambient conditions

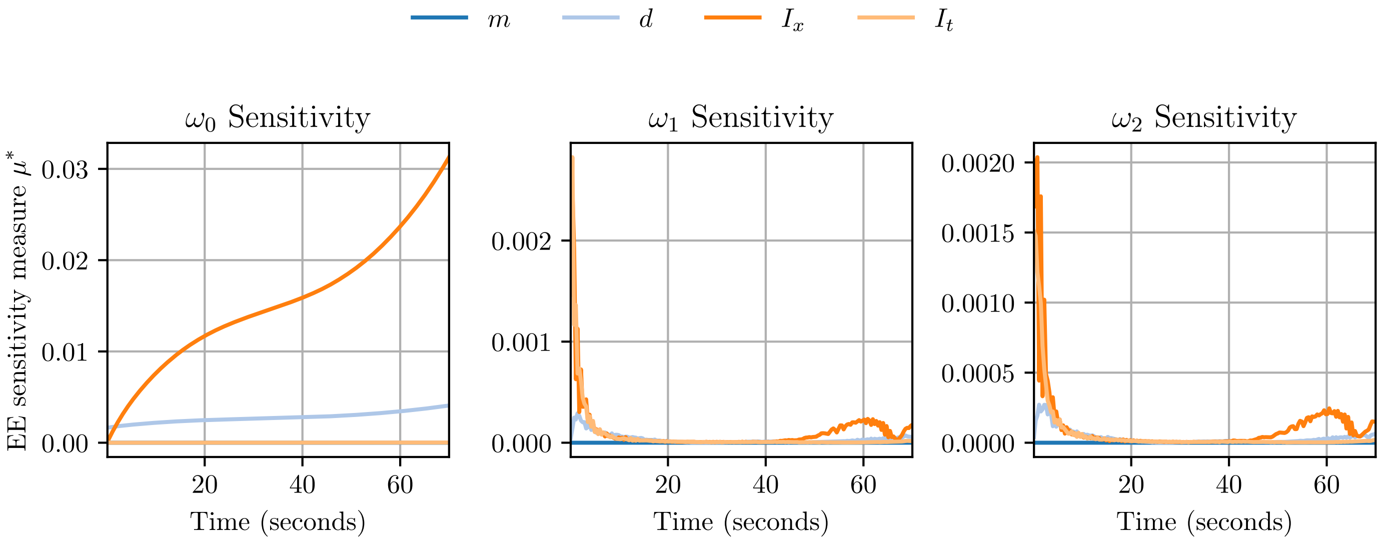

Figure E.47: Sensitivity to projectile properties

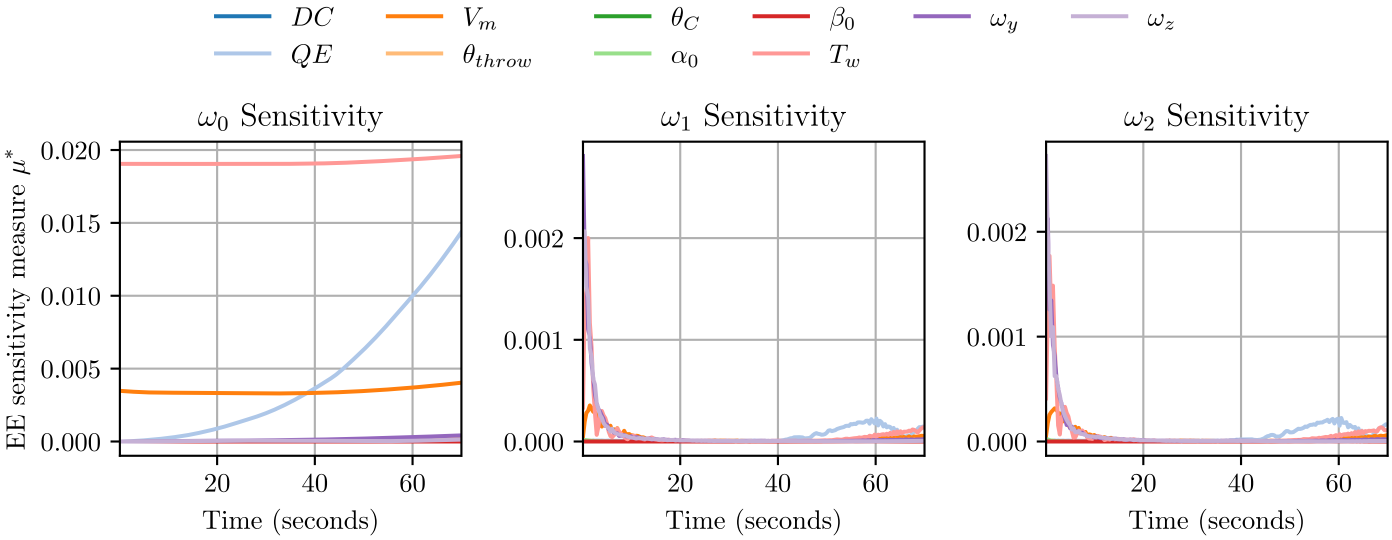

Figure E.48: Sensitivity to location and initial conditions

Table E.2: Sample inputs and Sensitivity analysis

Input	Distribution	Range	Units (SI)	μ	μ^*	σ
Ambient conditions						
T_0	Uniform	[5. 40.]	°C	0.007	0.007	0.001
P_0	Uniform	[99698. 103991.]	Pa	-0.002	0.002	0
R_H	Uniform	[8. 90.]	%	0.001	0.001	0
V_{WX}	Uniform	[-5.3 5.3]	m s^{-1}	0.002	0.002	0.002
V_{WY}	Uniform	[-5.3 5.3]	m s^{-1}	0.001	0.003	0.003
Earth properties						
LA	Uniform	[-38. -24.]	deg	0.001	0.001	0
AZ	Uniform	[-180. 180.]	deg	0.003	0.003	0.002
AL	Uniform	[0. 1000.]	m	0	0	0
Projectile properties						
m	Normal	[14.969 14.971]	kg	0	0	0
d	Normal	[0.104 0.105]	m	-0	0	0
I_x	Normal	[0.022 0.024]	kg m^2	0.001	0.001	0
I_t	Normal	[0.22 0.243]	kg m^2	-0	0	0
C_{D_0}	Normal	[95. 105.]	%	-0.006	0.006	0
C_{D_2}	Normal	[95. 105.]	%	-0	0	0
C_{L_0}	Normal	[95. 105.]	%	0	0	0
C_{L_2}	Normal	[95. 105.]	%	0	0	0
$C_{M_{\alpha 0}}$	Normal	[95. 105.]	%	-0	0	0
$C_{M_{\alpha 2}}$	Normal	[95. 105.]	%	0	0	0
C_{L_P}	Normal	[95. 105.]	%	-0	0	0
C_{M_P}	Normal	[95. 105.]	%	-0	0	0
C_{N_P}	Normal	[95. 105.]	%	0	0	0
$C_{N_{\dot{\alpha}}}$	Normal	[95. 105.]	%	0	0	0
$C_{M_{\dot{\alpha}}}$	Normal	[95. 105.]	%	0	0	0
Initial conditions						
DC	Normal	[-1. 1.]	deg	0	0	0
QE	Normal	[44. 46.]	m s^{-1}	0.058	0.058	0
V_m	Normal	[204. 206.]	deg	0.016	0.016	0
θ_{throw}	Normal	[0. 0.054]	deg	0.002	0.002	0
θ_C	Normal	[0. 360.]	deg	0	0	0
α_0	Normal	[-0.1 0.1]	deg	0	0	0
β_0	Normal	[-0.1 0.1]	cal/turn	-0	0	0
T_w	Normal	[17.8 18.2]	rad s^{-1}	-0	0	0
ω_y	Normal	[-1.44 1.44]	rad s^{-1}	0.001	0.002	0.002
ω_z	Normal	[-1.44 1.44]		0.001	0.001	0.002

List of References

Altufayl, A. (2019). *Development of a 6-DOF Trajectory Simulation Model for Asymmetric Projectiles*. Ph.D. thesis, North-West University.

Anderson, J. (2009). *Fundementals of aerodynamics*. 5th edn. McGraw-Hill Higher Education.

Baranowski, L., Gadomski, B., Majewski, P. and Szymonik, J. (2016). Explicit "ballistic M-model": A refinement of the implicit "modified point mass trajectory model". *Bulletin of the Polish Academy of Sciences: Technical Sciences*. ISSN 02397528.

Bradly, J. (1990). An alternative form of the Modified Point-Mass Equation of Motion. *Ballistic research laboratory*.

Buck, A.L. (1981). New Equation for computing vapor pressure. *Journal of Applied Meteorology*.

Bush, M. (1992). Remote Drug Delivery Systems Published by : American Association of Zoo Veterinarians Stable URL : http://www.jstor.org/stable/20095205 REVIEW ARTICLE REMOTE DRUG DELIVERY SYSTEMS. *Journal of Zoo and Wildlife Medicine*, vol. 23, no. 2, pp. 159–180.

Caudell, J.N., West, B.C., Griffin, B. and Davis, K. (2009). Fostering greater professionalism with firearms in the wildlife arena. In: *Human Dimensions of Wildlife Damage Management Fostering*, pp. 95–99.

Cavcar, M. (2000). The International Standard Atmosphere (ISA). *Anadolu University, Turkey*.

Chaves, E., Manezes, M.T. and Sobreiro, T. (2019). *Mini-curso "Corpo conciencinete na intervenção urbana"*, vol. 1. 3rd edn. CRC Press. ISBN 9781138055315.

Cooper, G.R. and Costello, M. (2011). Trajectory prediction of spin-stabilized projectiles with a liquid payload. *Journal of Spacecraft and Rockets*. ISSN 15336794.

Crassidis, J.L. and Markley, F.L. (2003). Quaternion Identities. *Fundamentals of Spacecraft Attitude Determination and Control*, vol. 3, no. 4, pp. 345–359.

Elsaadany, A. and Wen-Jun, Y. (2014). Accurate trajectory prediction for typical artillery projectile. In: *Proceedings of the 33rd Chinese Control Conference, CCC 2014*. ISBN 9789881563842. ISSN 21612927.

Ferziger, J.H. and Perić, M. (2002). *Computational Methods for Fluid Dynamics.*

Fluent, A. (2013). Ansys Fluent Theory Guide. *ANSYS Inc., USA.*

Fresconi, F., Cooper, G. and Costello, M. (2011). Practical Assessment of Real-Time Impact Point Estimators for Smart Weapons. *Journal of Aerospace Engineering*, vol. 11, no. January, pp. 1–11.

Gkritzapis, D.N. and Kaimakamis, G. (2008). A Review of Flight Dynamic Simulation Model of Missiles Hellenic Army Academy. pp. 257–261.

Gkritzapis, D.N., Panagiotopoulos, E.E., Margaris, D.P. and Papanikas, D.G. (2007). Computational atmospheric trajectory simulation analysis of spin-stabilized projectiles and small bullets. In: *Collection of Technical Papers - 2007 AIAA Atmospheric Flight Mechanics Conference.* ISBN 1563479052. ISSN 1752-5055.

Greenwood, D.T. (2003). *Advanced Dynamics.*

Hainz, L.C. and Costello, M. (2005). Modified projectile linear theory for rapid trajectory prediction. *Journal of Guidance, Control, and Dynamics*, vol. 28, no. 5, pp. 1006–1014. ISSN 07315090.

Hampton, J.O., Adams, P.J., Forsyth, D.M., Cowled, B.D., Stuart, I.G., Hyndman, T.H. and Collins, T. (2016). Improving animal welfare in wildlife shooting. *Wildlife Society Bulletin*, vol. 40, no. 4, pp. 1–27.

Henderson, D. (1977). Euler Angles, Quaternions, and Transformation Matrices. *NASA JSC Report.*

Hibbeler, R. (2010). *Engineering mechanics: Dynamics.* 12th edn. Upper Saddle River: Pearson.

Khalil, M., Rui, X. and Hendy, H. (2015). Discrete Time Transfer Matrix Method for Projectile Trajectory Prediction. *Journal of Aerospace Engineering*, vol. 28, no. 2. ISSN 0893-1321.

Koene, B., ID-Boufker, F. and Papy, A. (2008). Kinetic Non-lethal Weapons. *Netherlands Annual Review of Military Studies 2008: Sensors, Weapons, C4I and Operations Research.*

Lieske, R.F. and Reiter, M.L. (1966). Equations of Motion for a Modified Point Mass Trajectory. *Ballistic research laboratory.*

McCoy, R. (1999). *Modern Exterior Ballistics.* Schiffer Publishing. ISBN 0764338250,9780764338250.

Murphy, C. (1954). Data reduction for the free flight spark ranges.

Pneu-Dart (2020). Pneu dart Inc.
Available at: `http://www.pneudart.com/products/projectors/#gauged`

Press, W.H. and Teukolsky, S.A. (1992). Adaptive Stepsize Runge-Kutta Integration. *Computers in Physics*. ISSN 08941866.

Press, W.H., Teukolsky, S.A., Vetterling, T.W. and Flannery, B.P. (2007). *Numerical Recipies, The Art of Scientific Computing*. ISBN 978-0-521-88068-8.

Rogers, J., Costello, M. and Cooper, G. (2013). Design considerations for stability of liquid payload projectiles. *Journal of Spacecraft and Rockets*. ISSN 15336794.

Rosenfield, D. (2017). Introduction to Technical Aspects of Remote Drug Delivery Systems (* RDDS) with Telemetric Support in Free-Ranging Wildlife * RDDS = Remote Drug Delivery System. *Abravas*, vol. 2, no. September.

Saltelli, A., Ratto, M., Andres, T., Campolongo, F., Cariboni, J., Gatelli, D., Saisana, M. and Tarantola, S. (2008). *Global Sensitivity Analysis. The Primer*. ISBN 9780470059975.

Sandvik, A.W. (2018). Numerical Solutions of Classical Equations of Motion.

Schobeiri, M.T. (2010). *Fluid mechanics for engineers: A graduate textbook*. Springer. ISBN 9783642115936.

Tsien, H.S. (2012). *Collected Works of H.S. Tsien (1938–1956)*. Academic Press.

White, F.M. (2010). Fluid Mechanics (4th Edition). *Refrigeration And Air Conditioning*. ISSN 1364-0321. `1003.3921v1`.

Wie, B. (2008). *Space Vehicle Dynamics and Control, Second Edition*. American Institute of Aeronautics and Astronautics.